

AD-A259 771



2

WL-TR-92-2046

**TRANSVERSE INJECTION OF LIQUID
AND GASEOUS FUELS INTO
SUBSONIC/SUPERSONIC FLOW**

D. Papamoschou, W.A. Sirignano, and G.S. Samuelsen
UCI Combustion Laboratory
University of California
Irvine, CA 92717-3550

May 1992



DTIC
ELECTE
S **FEB 2 1993** **D**
C

Final Report for Period September 1988 to December 1991

Approved for public release; distribution is limited.

AERO PROPULSION AND POWER DIRECTORATE
WRIGHT LABORATORY
AIR FORCE SYSTEMS COMMAND
WRIGHT-PATTERSON AIR FORCE BASE, OHIO 45433-6563

98 2 1 045

93-01836



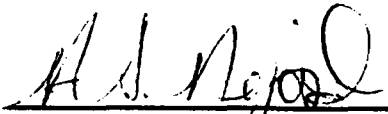
21/98

NOTICE


When Government drawings, specifications, or other data are used for any purpose other than in connection with a definitely Government-related procurement, the United States Government incurs no responsibility or any obligation whatsoever. The fact that the government may have formulated or in any way supplied the said drawings, specifications, or other data, is not to be regarded by implication, or otherwise in any manner construed, as licensing the holder, or any other person or corporation; or as conveying any rights or permission to manufacture, use, or sell any patented invention that may in any way be related thereto.

This report is releasable to the National Technical Information Service (NTIS). At NTIS, it will be available to the general public, including foreign nations.

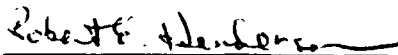
This technical report has been reviewed and is approved for publication.



ABDOLLAH S. NEJAD
Aerospace Engineer
Experimental Research Branch
Advanced Propulsion Division
Aero Propulsion & Power Directorate



JOHN T. HOJNACKI, Chief
Experimental Research Branch
Advanced Propulsion Division
Aero Propulsion & Power Directorate



ROBERT E. HENDERSON
Chief
Advanced Propulsion Division
Aero Propulsion & Power Directorate

If your address has changed, if you wish to be removed from our mailing list, or if the addressee is no longer employed by your organization please notify WL/POPT, WPAFB, OH 4533-6563 to help us maintain a current mailing list.

Copies of this report should not be returned unless return is required by security considerations, contractual obligations, or notice on a specific document.

REPORT DOCUMENTATION PAGE				Form Approved OMB No. 0704-0188	
1a. REPORT SECURITY CLASSIFICATION Unclassified			1b. RESTRICTIVE MARKINGS		
2a. SECURITY CLASSIFICATION AUTHORITY			3. DISTRIBUTION / AVAILABILITY OF REPORT Approved for public release; Distribution is unlimited		
2b. DECLASSIFICATION / DOWNGRADING SCHEDULE					
4. PERFORMING ORGANIZATION REPORT NUMBER(S) UCI-ARTR-92-2			5. MONITORING ORGANIZATION REPORT NUMBER(S) WL-TR-92-2046		
6a. NAME OF PERFORMING ORGANIZATION University of California		6b. OFFICE SYMBOL (if applicable)	7a. NAME OF MONITORING ORGANIZATION Aero Propulsion and Power Directorate Wright Laboratory.		
6c. ADDRESS (City, State, and ZIP Code) UCI Combustion Laboratory University of California Irvine, CA 92717			7b. ADDRESS (City, State, and ZIP Code) WL/POPT WPAFB, OH 45433-6563		
8a. NAME OF FUNDING / SPONSORING ORGANIZATION		8b. OFFICE SYMBOL (if applicable)	9. PROCUREMENT INSTRUMENT IDENTIFICATION NUMBER F33615-88-C-2889		
8c. ADDRESS (City, State, and ZIP Code)		10. SOURCE OF FUNDING NUMBERS			
		PROGRAM ELEMENT NO. 61102F	PROJECT NO. 2308	TASK NO. 51	WORK UNIT ACCESSION NO. 23
11. TITLE (Include Security Classification) Transverse Injection of Liquid and Gaseous Fuels into Subsonic/Supersonic Flow					
12. PERSONAL AUTHOR(S) Dr. G.S. Samuelsen					
13a. TYPE OF REPORT Final		13b. TIME COVERED FROM 0988 TO 1291		14. DATE OF REPORT (Year, Month, Day) May 1992	
15. PAGE COUNT 79					
16. SUPPLEMENTARY NOTATION					
17. COSATI CODES			18. SUBJECT TERMS (Continue on reverse if necessary and identify by block number) Supersonic flow, jets, jet injection		
FIELD	GROUP	SUB-GROUP			
19. ABSTRACT (Continue on reverse if necessary and identify by block number) The goal of the program was to provide needed insight into the mixing behavior of liquid and gaseous jets injected transversely into a high velocity crossflow.					
20. DISTRIBUTION / AVAILABILITY OF ABSTRACT <input checked="" type="checkbox"/> UNCLASSIFIED/UNLIMITED <input type="checkbox"/> SAME AS RPT. <input type="checkbox"/> DTIC USERS			21. ABSTRACT SECURITY CLASSIFICATION Unclassified		
22a. NAME OF RESPONSIBLE INDIVIDUAL Dr. A.S. Nejad or S.A. Ahmed			22b. TELEPHONE (Include Area Code) (513) 255-9991		22c. OFFICE SYMBOL WL/POPT

TABLE OF CONTENTS

SECTION	TITLE	PAGE
1.0	OVERVIEW	1
2.0	TASK 1: EXPERIMENTAL STUDY	2
2.1	SUMMARY	2
2.2	INTRODUCTION	2
2.3	APPROACH	4
2.4	EXPERIMENTAL FACILITY	7
2.5	EXPERIMENTAL CONDITIONS	9
2.6	RESULTS AND DISCUSSION	9
	2.6.1 Flow Visualization	9
	2.6.2 Jet Penetration	12
2.7	CONCLUSIONS	20
2.8	RECOMMENDATIONS FOR FOLLOW-ON WORK	20
	2.8.1 Turbulent Structure	20
	2.8.2 Shock Structure and Unsteadiness	21
	2.8.3 Total-Pressure Loss	21
	2.8.4 Inclination Angle	22
3.0	TASK 2: THEORETICAL STUDY	23
3.1	SUMMARY	23
3.2	INTRODUCTION	23
3.3	THEORY AND COMPUTATIONS	24
	3.3.1 Phase I	24
	3.3.2 Phase II	25
	3.3.3 Phase III	25

	3.3.4 Phase IV	29
	3.3.5 Phase V	38
4.0	REFERENCES	49
APPENDIX A	ESTIMATION OF AVERAGE PRESSURE AROUND JET	51
APPENDIX B	PHASE I: SIMPLE CHANNEL FLOWS	52
APPENDIX C	PHASE II: GASEOUS JET INJECTION	55
APPENDIX D	PHASE III: LIQUID JET INJECTION	71

LIST OF FIGURES

SECTION	TITLE	PAGE
2.1	Side view of idealized jet flow.	3
2.2	Idealized cross section of jet near orifice.	5
2.3	Schematic of supersonic tunnel and jet module.	8
2.4	Schlieren photographs of gaseous jets at $J = 8.35$ into air cross flow at $M_1 = 2.0$.	10
2.5	Effect of density ratio on jet trajectory.	13
2.6	Effect of M_j on trajectory for $J = 5.28$.	15
2.7	Effect of M_j on jet trajectory for $J = 8.35$.	16
2.8	Penetration distance h/d versus momentum ratio J for variable M_1 .	17
2.9	Penetration distance h/d versus momentum ratio J for variable pressure ratio.	18
2.10	Parameter C for incompressible and present compressible transverse jets.	19
3.1	Geometry concerned and the coordinate system used.	26
3.2	A representative 2-D computational cell.	26
3.3	(a) Velocity vector and jet cross section at $x=0.15 d$; Max. Vector= 1.71m/s . (b) Enlargement of the Recirculation Region; Max. Vector= 1.15 m/s .	33
3.4	(a) Velocity vector and jet cross section at $x=0.32 d$; Max. vector= 1.35 m/s . (b) Enlargement of the recirculation region; Max. vector= 1.17 m/s .	34
3.5	(a) Velocity vector and jet cross section at $z=5.28 d$; Max. vector= 1.61 m/s . (b) Velocity vector and jet cross section at $z=9.0 d$; Max. vector= 0.23 m/s . (c) Velocity vector and jet cross section at $z=23.75 d$; Max. vector= 0.03 m/s .	36
3.6	(a) Velocity vector at $y=0.1 d$; Max. vector= 1.02 m/s . (b) Enlargement of the wake region; Max. vector= 0.78 m/s .	37
3.7	The coordinate systems.	43
3.8	(a) Full interface conditions. (b) Approximate interface conditions at 0.00015 second .	45

3.9	(a) Full interface conditions. (b) Approximate interface conditions at 0.0066 second.	46
3.10	(a) Full interface conditions. (b) Approximate interface conditions at 0.008 second.	47
3.11	(a) Full interface conditions. (b) Approximate interface conditions at 0.011 second.	48
B.1	Centerline velocity development.	54
C.1	Velocity vectors (x-y) at $Z=0.00934$ m.	57
C.2	Mass fraction contours of injectant (x-y) at $z=0.00934$ m.	58
C.3	Velocity vectors (x-y) at $z=0.01362$ m.	59
C.4	Mass fraction contours of injectant (x-y) at $Z=0.01362$ m.	60
C.5	Velocity vectors (x-y) at $z=0.05055$ m.	61
C.6	Mass fraction contours of injectant (x-y) at $z=0.05055$ m.	62
C.7	Velocity vectors (z-y) at $x=0.00035$ m.	63
C.8	Mass fraction contours of injectant (z-y) at $x=0.00035$ m.	64
C.9	Velocity vectors (z-y) at $x=0.00362$ m.	65
C.10	Mass fraction contours of injectant (z-y) at $x=0.00362$ m.	66
C.11	Velocity vectors (z-x) at $y=0.00029$ m.	67
C.12	Mass fraction contours of injectant (z-x) at $x=0.00029$ m.	68
C.13	Velocity vectors (z-x) at $y=0.02066$ m.	69
C.14	Mass fraction contours of injectant (z-x) at $x=0.02066$ m.	70
D.1	Volume fraction contours at $z=0.016$ m.	72
D.2	Velocity vector plot at $z=0.016$ m.	73
D.3	Volume fraction contours at $x=0.0012$ m.	74
D.4	Velocity vector plot at $x=0.0012$ m.	74

LIST OF TABLES

SECTION	TITLE	PAGE
2.1	Transverse Jet Parameters	9

1.0 OVERVIEW

The program and present report is organized by the following two tasks:

<u>Task</u>	
1	Experimental Study
2	Theoretical Study

Dr. Papamoschou provided the leadership for Task 1, while Dr. Sirignano assumed the responsibility for Task 2. Dr. Sirignano was assisted by another member of the Department of Mechanical and Aerospace Engineering faculty, Dr. Said Elghobashi, and a post-doctoral researcher, Dr. Fanghei Tsau.

The goal of the program was to provide needed insight into the mixing behavior of liquid and gaseous jets injected transversely into a high velocity cross flow.

DTIC QUALITY INSPECTED 3

Accession For	
NTIS CHAI	<input checked="" type="checkbox"/>
DTIC TAB	<input type="checkbox"/>
Unannounced	<input type="checkbox"/>
Justification	
By	
Distribution/	
Availability Codes	
Avail and/or	
Dist	Special
A-1	

2.0 TASK 1: EXPERIMENTAL STUDY

2.1 SUMMARY

The penetration of round supersonic jets normal to a supersonic cross flow has been studied experimentally in a specially-configured supersonic wind tunnel. The cross-flow stream consisted of air at Mach numbers of 2 and 3. The jet Mach number ranged from 1 to 3.53 and the jet gases employed were helium and argon. Schlieren photography was the primary diagnostic. The study examined the effects of jet-to-freestream momentum ratio, jet and freestream Mach numbers, and pressure and density ratios at the jet exit. It is found that penetration is strongly dependent on momentum ratio, weakly dependent on Mach numbers and pressure ratio, and independent of density ratio. For fixed momentum ratio, increasing freestream Mach number produced a small increase in penetration, while changing the jet Mach number produced no apparent effect. Values of pressure ratio that appear to maximize penetration are suggested in the report. Flow visualization reveals large-scale turbulent structures in the jet and significant unsteadiness of the bow shock in front of the jet.

2.2 INTRODUCTION

The problem of supersonic injection into a supersonic cross flow is very interesting both from the point of view of fundamental knowledge and from the point of view of practical applications. Such applications include thrust vectoring of spacecraft and fuel injection in the combustor of supersonic-combustion ramjet (SCRAMJET) engines. While there has been considerable experimental and theoretical work in the past, a host of questions remain to be addressed. Central among those is how the relevant parameters in the flow independently affect penetration, and how the behavior of so-called "pressure matched" jets differs from that of underexpanded jets. Figure 2.1 depicts a simplified side view of the flow of interest, highlighting the essential features. The injection into a supersonic cross flow generates a bow shock wave, which is of crucial importance in the jet behavior. The sketch of Figure 2.1 represents a "pressure-matched" jet devoid of shock/expansion waves downstream of its orifice. Although the definition of "pressure matching" is far more complex than in the case of a jet issuing into a quiescent medium, the study of "pressure-matched" jets is desirable because (a) the flow field is relatively simpler and (b) such jets are likely to provide better penetration for reasons explained later.

The majority of experiments in the literature encompass underexpanded jets, with the jet static pressure substantially higher than the static pressure of the cross flow in the vicinity of the jet orifice. In the experiments of Zukoski and Spaid [1], gas was injected through a sonic orifice into a supersonic cross flow. It was shown that the penetration distance scaled with the ratio of jet to free-stream total pressures. A simple model, based on the rough approximation of the jet injection pattern as a blunt axisymmetric body, predicted reasonably well the jet penetration distance. Schetz et al. [2] studied experimentally supersonic underexpanded transverse jets and noted that penetration increases slightly with jet Mach number. The works by Schetz and Billig [3] and by Billig et al. [4] incorporate experimental data into more advanced models of the flow field and generate the important concept of "effective back pressure" felt by the jet. McDaniel and Graves [5] used laser-induced fluorescence to study penetration and spreading of sonic underexpanded jets with low momentum ratio, and inferred a linear dependence of penetration on momentum ratio. Recently, Heister and Karagozian [6] modeled the pressure-matched jet by means of a compressible vortex pair and obtained theoretical predictions of jet trajectory.

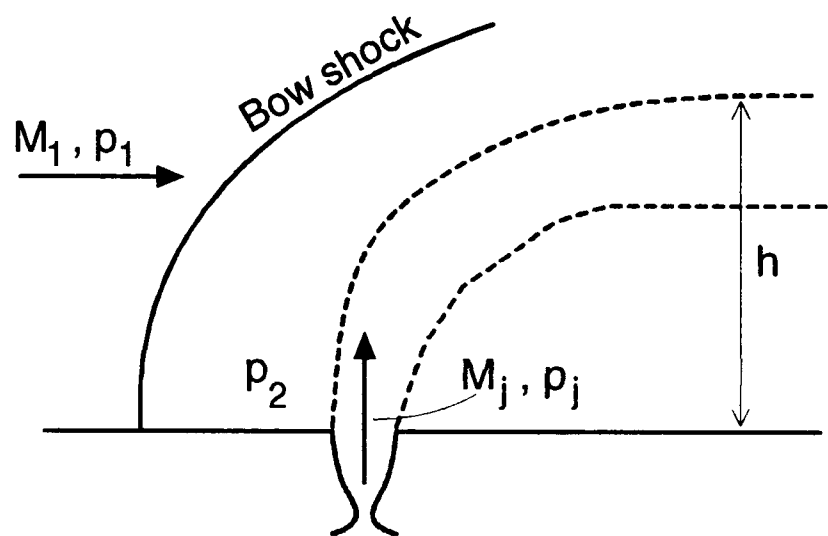


Figure 2.1: Side view of idealized jet flow.

In the studies of Schetz and Billig and of Heister and Karagozian, it is pointed out that the pressure-matched jet is likely to achieve better penetration than the underexpanded jet. The reason is that underexpansion (as well as overexpansion) generates shock waves in the jet flow leading to creation of a Mach disk, which renders the jet flow subsonic. Hence, the jet loses most of its momentum and is unable to penetrate further into the free stream.

A typical complication in the previous studies is that, when studying the dependence of trajectory on flow parameters, more than one of the relevant parameters were varied at a given time. For example, it was very common to increase momentum ratio by increasing jet Mach number or jet pressure, thus clouding the effects of individual variables. It should be noted, on the other hand, that some variables cannot be readily uncoupled from each other. In that case, certain assumptions are needed in order to infer the isolated effect of each variable, as will be shown later.

The goal of the present study was to conduct a parametric study of jet penetration versus relevant flow parameters in a fashion that attempts to uncouple the effect of a given variable from those of the others. Since very little is presently known about "pressure-matched" jets, the study concentrates on establishing "pressure matching" conditions for which the shock structure of the issuing jet appears to be weakest.

2.3 APPROACH

The flow that results from the interaction of a transverse jet with a supersonic cross flow is extremely complex. This study explores the global features of the flow, primarily the penetration distance and its scaling versus the flow parameters. It is desired to selectively vary those parameters in order to describe their individual influence on penetration.

The sketch of Figure 2.2 helps in the discussion that follows. Freestream conditions are denoted by subscript (1), conditions behind the shock by subscript (2), and jet-exit conditions by subscript (j). The shock interacts with the boundary layer and creates a separation region ahead of the jet. There is also a separation region behind the jet. The conditions in the front separation region could dominate the behavior of the jet if the jet penetration is of similar scale as the separated boundary-layer thickness (Schetz and Billig [3]). Highly-underexpanded jets, with a Mach disk close to the jet exit, are likely to fall under that category. However, the intent of this study is to create jets that will penetrate far into the cross stream, so it will be assumed that the separation region is of secondary importance.

It is known that the penetration of the subsonic jet injected perpendicularly to a subsonic freestream scales with the jet-to-cross flow momentum ratio, $J = \rho_j U_j^2 / \rho_1 U_1^2$ (Broadwell and Breidenthal [7]). In the supersonic case, the following additional variables are likely to play a significant role on jet penetration: freestream Mach number M_1 ; jet Mach number M_j ; pressure ratio at the jet exit, p_j/p_2 ; and density ratio at the exit, ρ_j/ρ_2 . A parametric statement including all the above parameters could be of the form:

$$\frac{h}{d} = \frac{h}{d}(J, M_1, M_j, \frac{p_j}{p_2}, \frac{\rho_j}{\rho_2}) \quad (2.1)$$

where h/d is penetration normalized by jet-exit diameter. Equation 2.1 illustrates two basic views of the flow field: (a) the integral, control-volume view, in which the variables J and

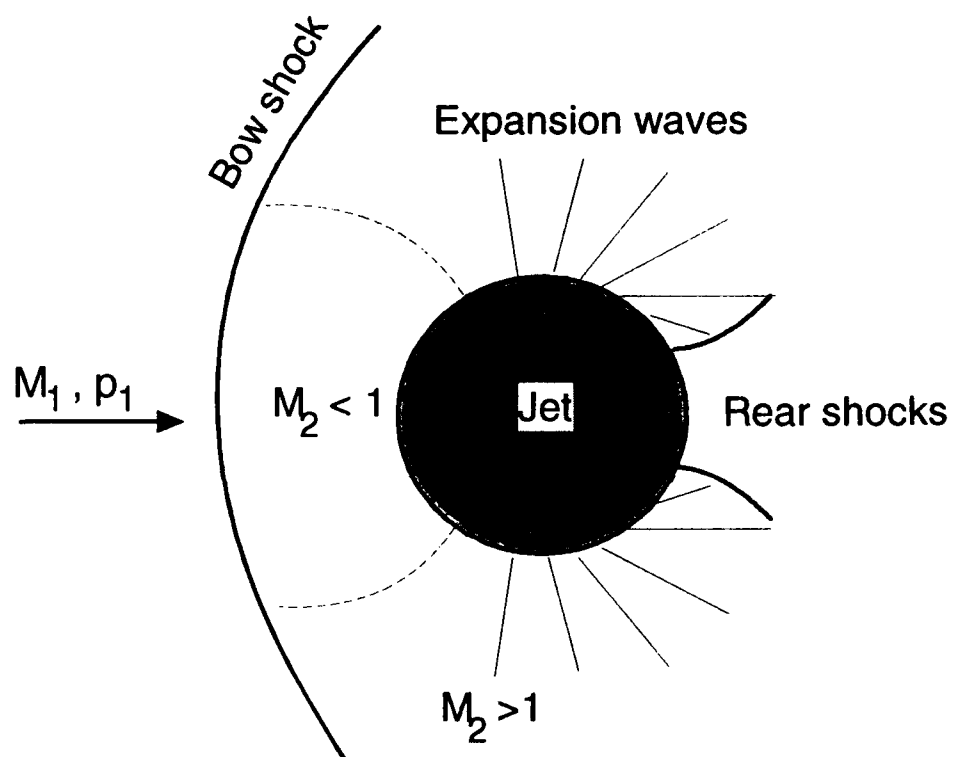


Figure 2.2: Idealized cross section of jet near orifice.

M_1 are salient; (b) the localized view of critical areas - in this case the vicinity of the jet exit - in which the variables M_j , p_j/p_2 , and ρ_j/ρ_2 are important. Still, it is impossible for a simple statement like the above to capture all the relevant fluid-mechanical processes. Rather, it represents a guide for a systematic study of the jet and an educated guess as to which parameters are important. It is desired to selectively vary each parameter to see its effect on jet penetration. However, as noted previously, there is interdependence of some parameters that needs to first be established.

For compressible flow, the momentum ratio J can be written in the form:

$$J = \frac{\gamma_j p_j M_j}{\gamma_1 p_1 M_1}$$

which shows its dependence on Mach numbers and static pressures in the jet and cross flow. The normal-shock relation between p_2 and p_1 is:

$$p_2 = p_1 \frac{2\gamma_1 M_1^2 - (\gamma_1 - 1)}{\gamma_1 + 1}$$

which for $M_1 > 2$ is well approximated by $p_2 \approx p_1 \frac{2\gamma_1 M_1^2}{\gamma_1 + 1}$. This enables us to relate J to p_2 and write Equation 2.1 in the form:

$$\frac{h}{d} = \frac{h}{d} (J = \frac{2\gamma_j}{\gamma_1 + 1} \frac{p_j}{p_2} M_j^2, M_1, M_j, \frac{p_j}{p_2}, \frac{\rho_j}{\rho_2}) \quad (2.2)$$

which shows that, for given p_j/p_2 , the momentum ratio J is a very strong function of M_j . Consequently, for fixed J , it is very hard to independently vary M_j and p_j/p_2 . Switching between gases of very different γ 's allows only marginal room for independent variation of these parameters, which is not enough to obtain meaningful trends. However, if one makes the assumption that above a certain level of underexpansion the numerical value of p_j/p_2 makes little difference on jet penetration, then the effects of J and M_j can be examined at independently. Conversely, Equation 2.2 shows that M_1 has a very weak influence on J ; therefore, it can be varied by a large extent while keeping all other variables virtually fixed.

As noted earlier, it was desired to focus our study on "pressure-matched" jets. There is major difficulty, however, in defining pressure matching for the supersonic case; due to compressibility in the cross flow, the static pressure around the jet varies greatly along its circumference as well as along its trajectory. Figure 2.2 shows the major waves around the jet perimeter, with the jet idealized as an inviscid circular cylinder. Clearly, it is impossible to create an ideally pressure-matched, supersonic transverse jet. The objective here is to avoid, or at least delay, the occurrence of the Mach disk by minimizing the strength of shock/expansion waves at the jet exit.

As a first try, one may set $p_j = p_2$, p_2 being the static pressure immediately aft of the normal shock. A further refinement comes by setting p_j equal to the static pressure averaged around the jet circumference, denoted here by \bar{p} . A simple calculation, presented in Appendix A, that takes into account the shock/expansion waves on the jet perimeter produces the result $\bar{p} \approx 0.5p_2$, for $M_1 \geq 1.5$. It appears reasonable, therefore, to initially take $p_j = 0.5p_2$ as the "pressure-matched" case, subject to further refinement as more details about the flow field become known. That pressure is lower than the "effective back pressure" of $0.8p_2$ suggested by Schetz et al. [2] or the value of $2/3 p_{t2}$, with p_{t2} the total

pressure after the bow shock, suggested by Billig et al. [4]. However, it is in good agreement with the "equivalent pressure" (the static pressure averaged around the jet perimeter) computed numerically by Heister and Karagozian [6].

2.4 EXPERIMENTAL FACILITY

Funds from AFWAL were instrumental for developing and enhancing the UCI Supersonic Turbulence Laboratory to accommodate the transverse-jet experiments reported here. The facility is depicted schematically in Fig. 2.3. The main flow consisted of air, supplied by compressors with capacity up to 2400 SCFM (specific cubic feet per minute). Two additional gas-supply systems, each connected to a row of 10 gas cylinders, can be connected to the main flow or to the transverse-jet line. In this study, the main flow was always air and the additional gas lines were used to supply the jet. The test-section Mach number is variable by means of removable nozzle blocks, designed by the method of characteristics. In this investigation, the test-section Mach numbers were 2 and 3.

The test section is 38mm high, 64mm wide and 500mm long. Test-section static pressures were in the range of 2 to 3psia. The test section was surrounded by plexiglas windows, mounted on the side walls as well as on the top and bottom walls. The top and bottom walls can be deflected to enable adjustment of the streamwise pressure gradient.

The downstream end of the apparatus is connected to a large (750ft³) vacuum vessel, evacuated by a high-capacity vacuum pump (Stokes, Model 412H). Experiments were typically done in short runs of 2 sec. An AT-386 computer with A/D board and D/A boards is used for control and data acquisition.

A subsystem to the main gas delivery system controls the gas and flow rate supplied to the small transverse jet (Figure 2.3). The flow is controlled by fine-metering valves to obtain accurate pressure regulation. The system allows instantaneous gas selection from either of the three supply systems. Helium and argon were used for the jet gas in this study.

Replaceable modules, mounted flush with the test-section wall, incorporate small supersonic nozzles for the transverse jet, each module for a different Mach number. The nozzles have smooth converging-diverging shapes formed by inserting an appropriately-machined male mold in wet epoxy and retracting it after the epoxy dried. By precision drilling of the sonic throat, it was ensured that the nozzles had the correct area ratio for the desired Mach numbers. The nozzle diameter at the exit is $d = 3\text{mm}$. Modules were built for Mach numbers 1, 2.15, 2.81, 3.15, and 4.27, corresponding to $\gamma = 5/3$.

The schlieren system has a focal length of 150mm and beam diameter of 150mm. The light source is a 20-nanosecond spark gap (Xenon, Model 787-B). A horizontal knife edge was used for intercepting the light beam. Two devices were used for imaging: a conventional 35-mm camera, and a CCD Imaging System with 576 x 384 pixel resolution (Photometrics Star I). The CCD system contains a camera controller with video monitor which digitizes, stores, and displays the image. Instant image acquisition proved to be very valuable, allowing us to immediately examine the flow field and notice the changes taking place the flow parameters were varied.

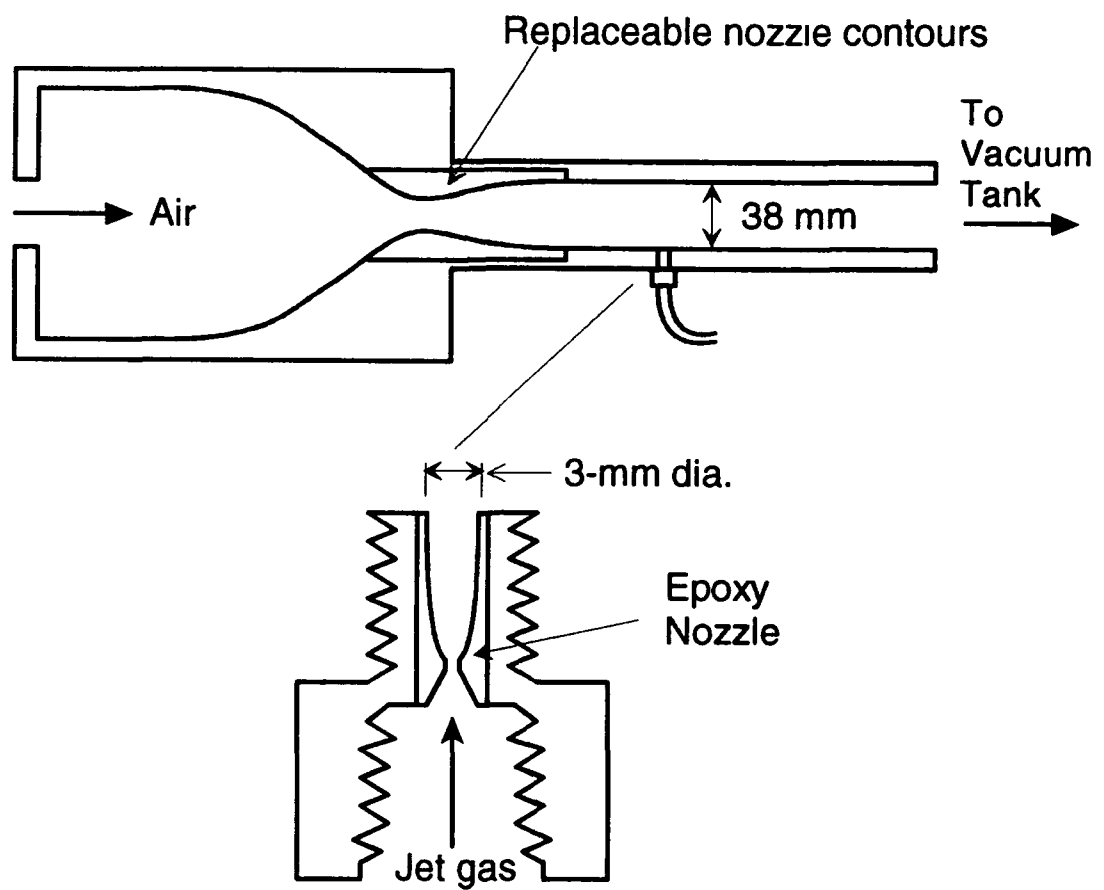


Figure 2.3: Schematic of supersonic tunnel and jet module.

The static pressure distribution along the test section was recorded by means of 16 individual pressure transducers (Omega Engineering, Model PX-136) connected to pressure ports along the upper and lower test-section walls. Pressure ports in the high-pressure part of the facility are also connected to pressure transducers (Setra, Model 280E).

2.5 EXPERIMENTAL CONDITIONS

The table below lists the experimental cases together with the relevant parameters. Cases are tabulated in order of increasing momentum ratio J . Cases with the same numbers have exactly or approximately the same value of J . The cross-flow gas is air for all cases.

Table 2.1 Transverse Jet Parameters

Case	J	M_1	M_j	p_i/p_2	ρ_i/ρ_2	Jet Gas
1a	1.67	2.0	2.15	0.3	0.10	He
1b	1.70	3.0	2.15	0.3	0.10	He
2	2.40	2.0	2.81	0.3	0.14	He
3a	3.09	2.0	2.15	0.5	0.18	He
3b	3.16	3.0	2.15	0.5	0.44	He
4	4.21	2.0	3.53	0.3	0.20	He
5a	5.28	2.0	1.00	5	0.93	He
5b	5.28	2.0	2.81	0.5	0.25	He
5c	5.39	3.0	2.81	0.5	0.24	He
6	6.59	3.0	4.27	0.3	0.27	He
7a	8.35	2.0	2.15	1.6	0.55	He
7b	8.35	2.0	2.81	0.8	0.40	He
7c	8.35	2.0	3.53	0.5	0.36	He
7d	8.35	2.0	3.53	0.5	3.60	Ar

Typical unit Reynolds numbers were in the neighborhood of 10^5 mm^{-1} associated with test-section pressures in the range of 3 psia.

2.6 RESULTS AND DISCUSSION

2.6.1 Flow Visualization

Representative schlieren pictures of the supersonic transverse-jet flow field are shown in Fig. 2.4. Exposure time was 20ns and the knife edge horizontal, accentuating gradients in the transverse direction.

All four cases depicted in Fig. 2.4 have the same momentum ratio, $J = 8.35$, however the jet gas and jet Mach number are variable. Cases 7a-7c employ helium in the jet gas and the jet Mach number increases from 2.15 (Case 7a) to 2.81 (Case 7b) to 3.53 (Case 7c). As shown in Fig. 2.4(a), there is no noticeable change in the jet trajectory as M_j increases, which suggests that penetration is insensitive to variations in the jet Mach number. In terms of pressure ratio, the corresponding trend is from highly under-expanded to nearly pressure matched. Case 7d has exactly the same momentum ratio and Mach numbers as Case 7c, only the helium is now substituted by argon in the jet gas. This was done to examine the effect of a ten-fold increase of density ratio on penetration. As can be seen from Fig. 2.4(b), the argon jet penetrates approximately the same distance as the helium jet, hence density ratio does not appear to influence penetration.

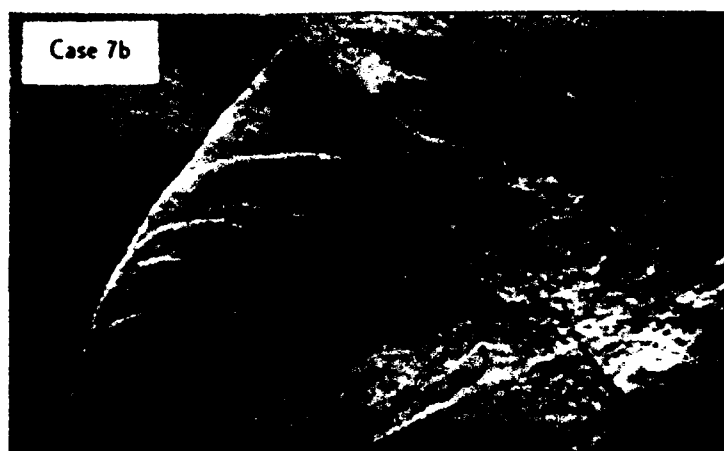


Figure 2.4(a): Schlieren photographs of gaseous jets at $J = 8.35$ into air cross flow at $M_1 = 2.0$ (case 7a, helium jet at $M_j = 2.15$; case 7b, helium jet at $M_j = 2.81$, case 7c, helium jet at $M_j = 3.53$).



Figure 2.4(b): Schlieren photographs of gaseous jets at $J = 8.35$ into air cross flow of $M_1 = 2.0$ (case 7c, helium jet at $M_j = 3.53$; case 7d, argon jet at $M_j = 3.53$).

As expected, the bow shock wave in front of the jet dominates the flow field. A separation region forms in front of the bow shock and creates a secondary, oblique shock near the wall. The boundary layer ahead of the shock is turbulent, with an estimated thickness of 3mm. For the argon jets (Case 7d in Figure 2.4b) the bow-shock shape is smooth, resembling the classic picture of a shock in front of a blunt body. For the helium jets (Cases 7a-7c in Figure 2.4a) the bow shock shape is wrinkled due to interaction with pressure waves emanating from the jet exit, probably caused by the turbulent eddies of the jet moving at supersonic speeds (around 1500m/s) with respect to the surrounding air. For the argon jets, these eddies are subsonic with respect to the surrounding air, so they do not generate large pressure disturbances.

By comparing shapes for several, time-uncorrelated pictures of the same flow field, we noticed that the shock structure is considerably unsteady. For example, the point of reflection of the shock with the upper wall moved as much as 10mm (1/4 of test-section height) from one picture to the other. Unsteadiness appears to be a major aspect of this flow field, something that turbulence models need to take into consideration.

We were able to observe the turbulent structure of the jet for up to $x/d = 20$. The structure appears to have regular, repeating features, much like that of the subsonic transverse jet. Interaction of the reflected bow shock with the jet caused apparent enhancement of the turbulence.

2.6.2 Jet Penetration

The penetration height h is defined here as the maximum height of the jet trajectory, based on schlieren visualization of the upper edge of the jet. The trajectory is seen to level off at $x/d \approx 8$, which is where penetration measurements are referenced. Each value of h/d reflects an average of typically 10 individual trajectory heights measured from separate runs at the same condition. Trajectory heights downstream of the jet's interaction with the reflected bow shock ($x/d > 10$) were not used for inferring penetration height as the enhanced turbulence from that interaction prevents clear visual identification of the edge of the jet. Because the flow is unsteady, and because of the subjective nature of identifying the top edge of the jet, the error in each measurement of h is estimated to be within 10%.

Below we outline the results of the parametric study of h versus J , M_1 , M_j , p_j/p_2 and ρ_j/ρ_2 along the lines of Equations 2.1 and 2.2. The reader is referred to Table 2.1 where these parameters are tabulated for each test case.

Effect of ρ_j/ρ_2 : Comparisons are made between cases 7c and 7d, which have identical p_j/p_2 ; but ρ_j/ρ_2 varies by a factor of 10. This is achieved by simply substituting argon for helium in the jet, keeping everything else constant. The jet trajectories are shown in Figure 2.5 where they appear practically identical. Hence, density ratio has no noticeable effect on h . This agrees with the earlier result of Crans and Collins [9] that molecular weight does not influence penetration.

Effect of M_j : Comparisons are made between cases 5a-5b, and 7a-7b-7c. The values of J and M_1 are constant for each comparison. The density ratio ρ_j/ρ_2 changes, but that was shown to have no effect from the previous set of comparisons. The pressure ratio p_j/p_2 also changes, which is unavoidable as shown by Equation 2.2. As previously stated, it is our assumption that underexpanded jets behave in a similar manner regardless of the actual value of p_j/p_2 . Experimental observations discussed later lead us to define underexpanded jets as those with $p_j/p_2 \geq 0.5$. As can be seen from Table 2.1, the cases compared here involve only underexpanded jets.

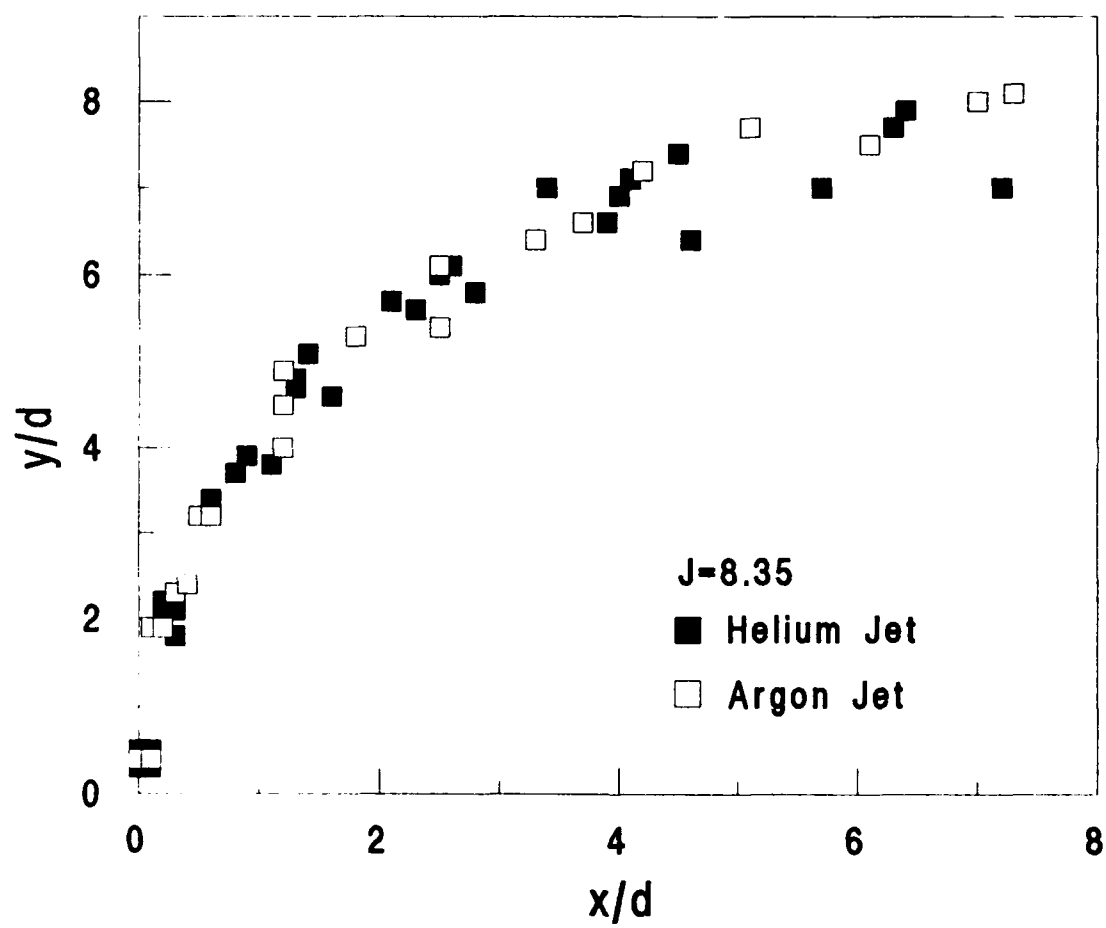


Figure 2.5: Effect of density ratio on jet trajectory.

Trajectories of jets with variable M_j corresponding to the above cases are shown in Figure 2.6 for $J = 5.28$ and Figure 2.7 for $J = 8.35$. The scatter in the trajectory plots reflects the turbulent structure of the jet but also the unsteadiness of the entire bow shock-jet system. For given J and M_1 , there is no perceptible difference between the trajectories, which suggests that M_j alone has little or no effect on penetration. Again, this is subject to our assumption that for $p_j/p_2 \geq 0.5$, the actual value of p_j/p_2 has no substantial effect on penetration.

Effect of M_1 : Comparisons are made between cases 1a-1b, 3a-3b, and 5b-5c. The weak dependence of J on M_1 allows us to vary M_1 , keeping M_j and p_j/p_2 fixed, and produce very little change in J . Penetration height h/d versus J for different M_1 's is shown in Figure 2.8. It is noted that increasing M_1 from 2 to 3 has a beneficial, albeit modest, effect on h , which increases on the order of one jet diameter. This plot also serves to show the expected strong dependence of h on J .

Effect of p_j/p_2 : Visual observation of the transverse jet near field indicated that the shock/expansion waves near the jet exit appeared weakest when the jet total pressure was set such that $p_j/p_2 \approx 0.3$. This led us to re-evaluate the criterion $p_j/p_2 = 0.5$ for "pressure matching" by examining jet penetration at $p_j/p_2 = 0.3$ versus at $p_j/p_2 = 0.5$. Our investigation was aided by the previous result that M_j seems to have little or no effect, on penetration. Comparisons are made between cases 1a-2-4 ($p_j/p_2 = 0.3$) and 3a-5b-7c ($p_j/p_2 = 0.5$). The Plot of h/d versus J for $p_j/p_2 = 0.3$ and $p_j/p_2 = 0.5$ is shown in Figure 2.9. It is noted that for the lower pressure ratio, the jet penetrates further by about 0.5 to 1 jet diameters. Similar correlations for cases with $p_j/p_2 > 0.5$ would fall roughly on the $p_j/p_2 = 0.5$ curve, adding validity to our assumption that p_j/p_2 does not affect penetration once it exceeds about 0.5. If indeed the hypothesis that "pressure-matched" transverse jets exhibit maximum penetration is correct, then the criterion of $p_j/p_2 = 0.3$ for "pressure matching" appears better than that of $p_j/p_2 = 0.5$.

Effect of J : All the previous comparisons have established the momentum ratio J as being the dominant quantity in this flow field. Figures 2.8 and 2.9 show how penetration height h scales with J . Although an exact power law dependence of h on J cannot be inferred from our data, we attempt here a rough comparison of the $h - J$ scaling found here to that established for subsonic flows:

$$\frac{y}{d} = C_i J^{1/3} \left(\frac{x}{c} \right)^{1/3}$$

by Broadwell and Breidenthal [7]. The incompressible constant C_i has the value of about 2.2, as inferred by data of Pratte and Baines [8]. Here we compute a compressible parameter C such that:

$$\frac{h}{d} = C J^{1/3} \left(\frac{x_h}{d} \right)^{1/3}$$

where x_h is the axial location of our penetration measurements (around $x/d = 8$). The parameter C is plotted versus J in Figure 2.10, where it is seen that it does not depart very much from the subsonic value. Considering that this is a rough comparison, it helps only to illustrate that the penetration scaling of the supersonic transverse jet is not dramatically different from that of the subsonic jet.

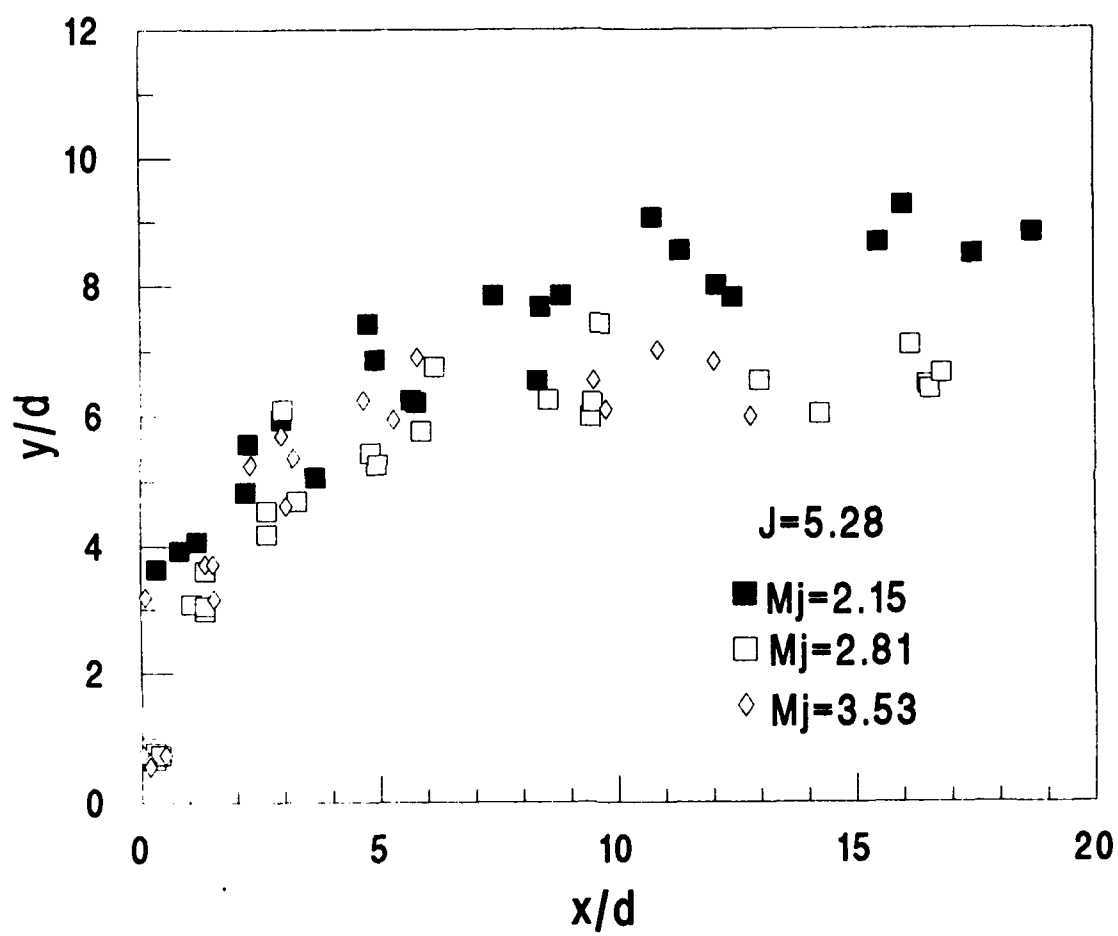


Figure 2.6: Effect of M_j on jet trajectory for $J = 5.28$.

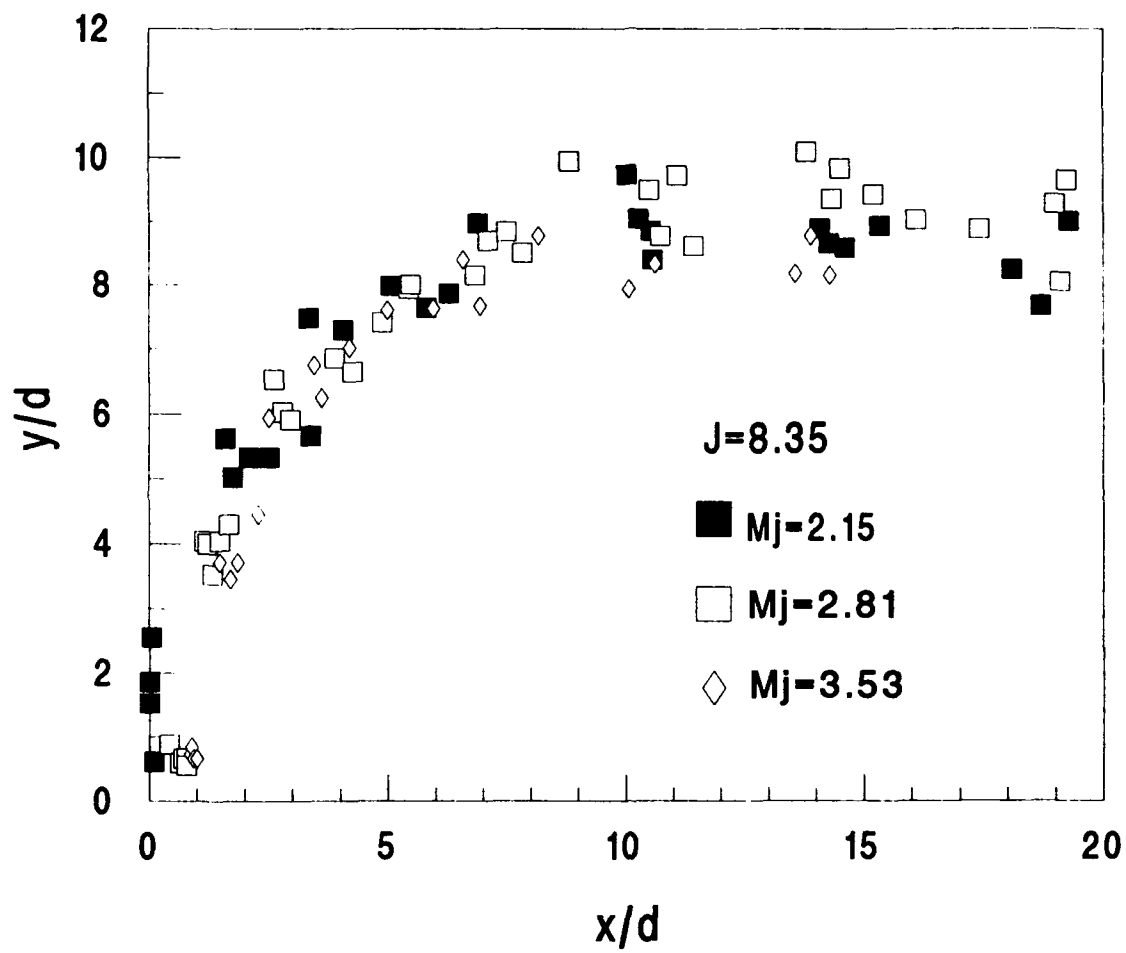


Figure 2.7. Effect of M_j on jet trajectory for $J = 8.35$.

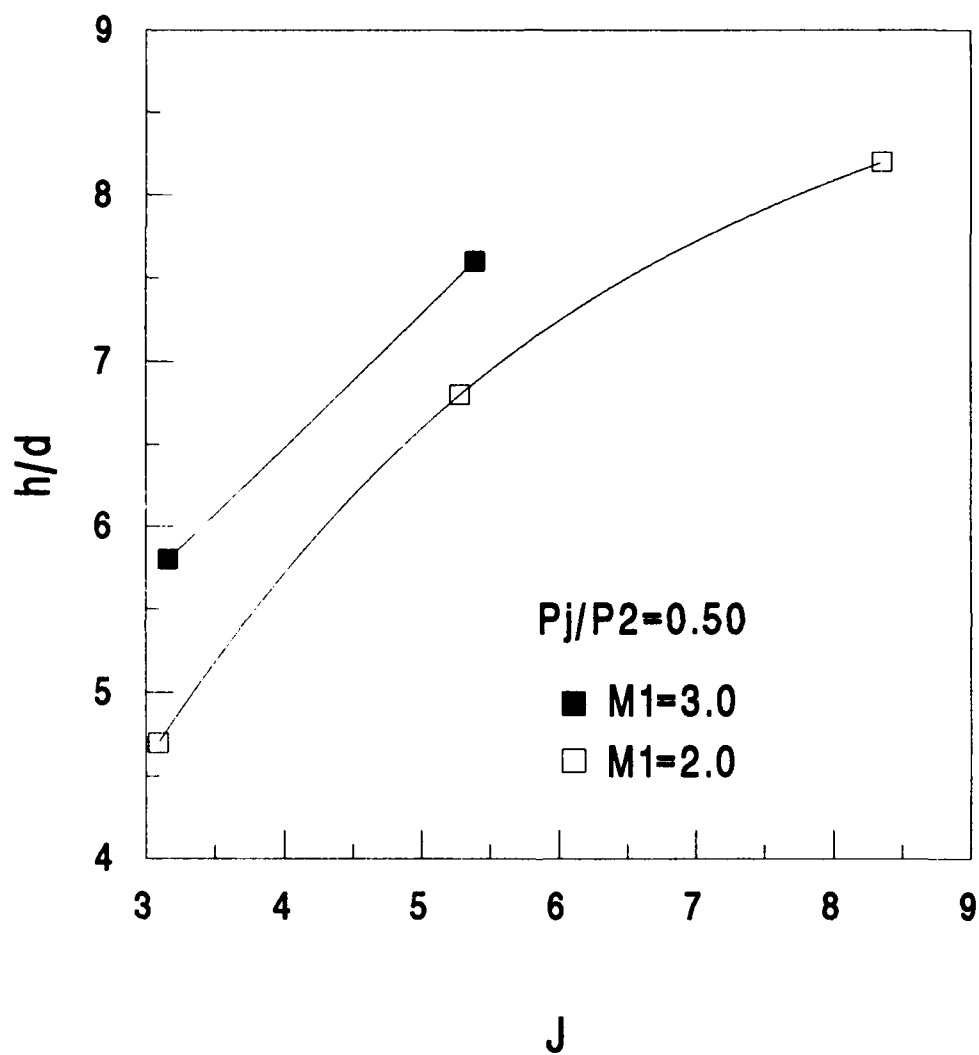


Figure 2.8: Penetration distance h/d versus momentum ratio J for variables M_1 .

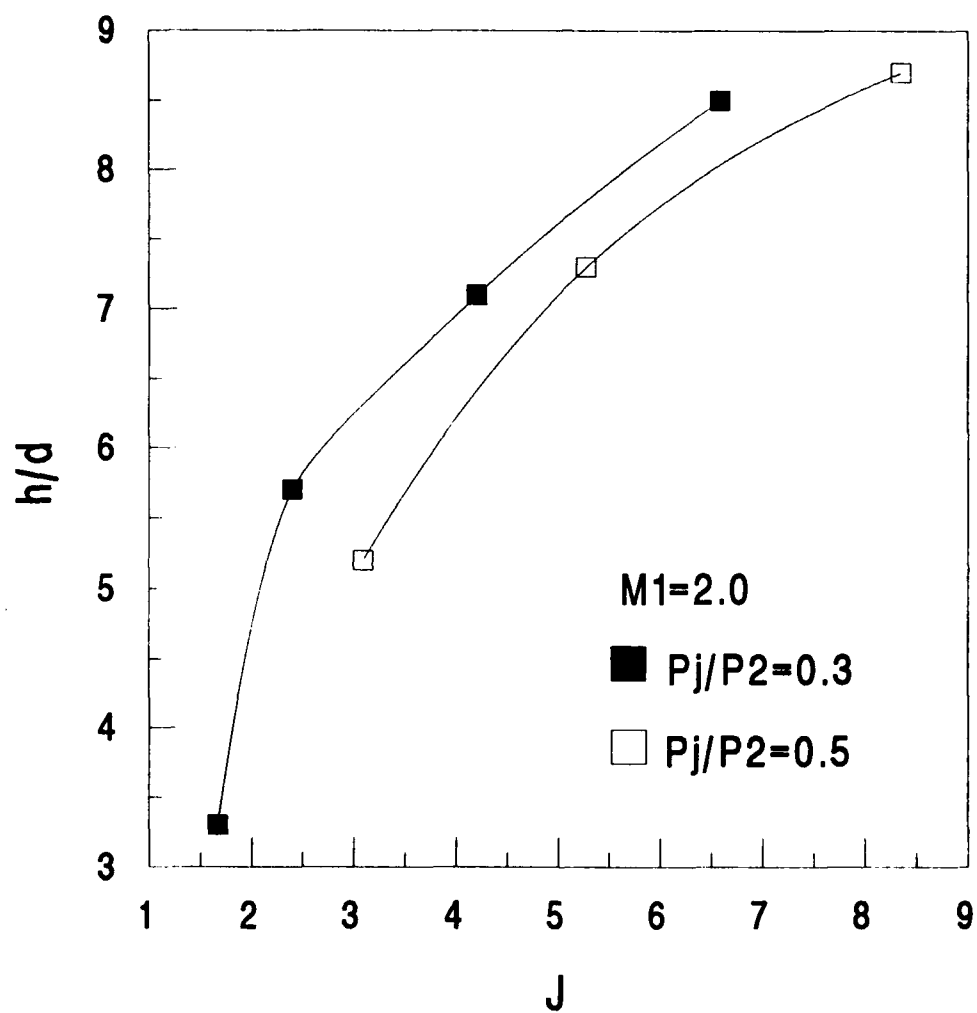


Figure 2.9: Penetration distance h/d versus momentum ratio J for variables pressure ratio.

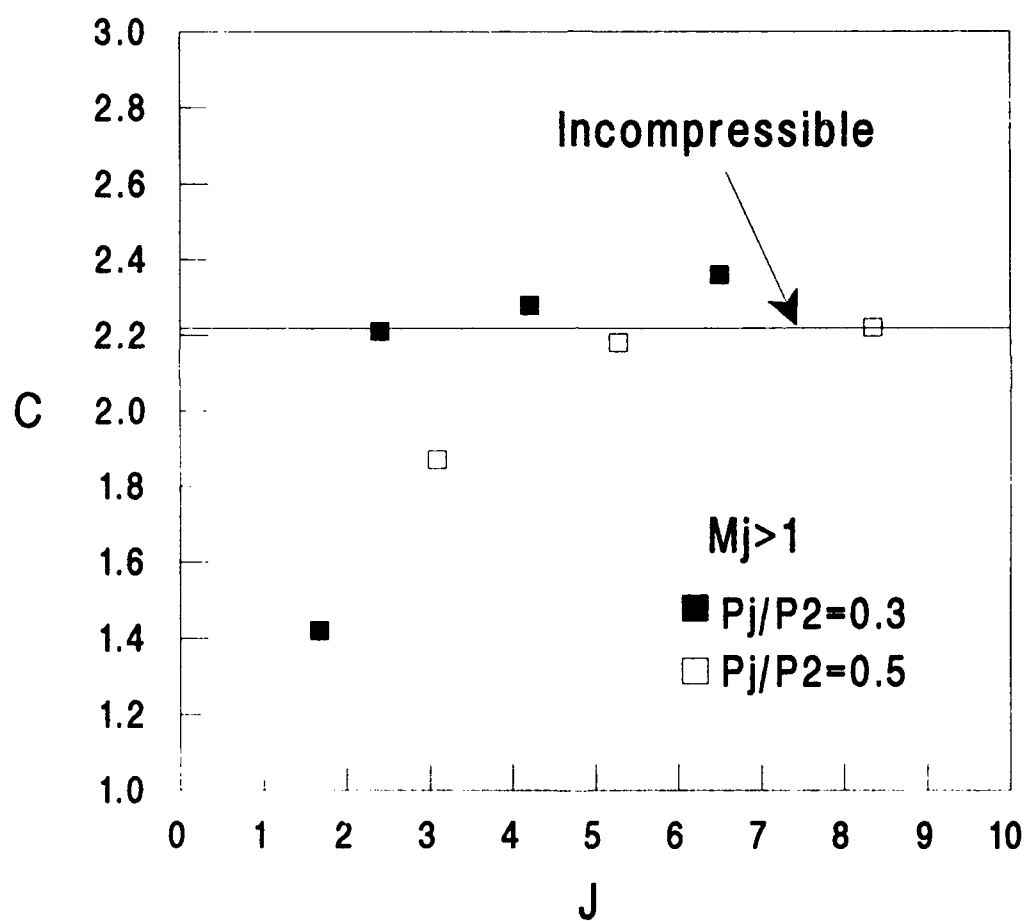


Figure 2.10: Parameter C for incompressible and present compressible transverse jets.

The above comment should not be construed as establishing a similarity between subsonic and supersonic transverse jet in other aspects of the flow field. A distinct feature of the supersonic case is the severe kinetic energy loss due to jet impingement, represented by the large extent of the bow shock seen in the pictures. Growth rate and mixing, quantities not measured here, may be very different in the subsonic and supersonic cases.

Our finding that increasing M_1 slightly increases h is rather surprising and disagrees with theoretical predictions of Heister and Karagozian [6], which show a small decrease of h with M_1 . However, if one approximates the near field of the jet as an inviscid circular cylinder, then the result starts making sense: it is well known that the drag coefficient of the cylinder decreases with increasing supersonic Mach number³. Hence, the drag of the jet near the exit, normalized by the cross-flow momentum, is expected to decrease as M_1 increases from 2 to 3. This will produce a higher penetration, at least in the near field.

2.7 CONCLUSIONS

An experimental parametric study of supersonic transverse-jet penetration versus relevant flow parameters has established the momentum ratio J as the dominant variable. Penetration height increases with J in a fashion fairly similar to that found in subsonic flows. Increasing free-stream Mach number M_1 modestly improves penetration, while the jet Mach number M_j appears to have no effect. Density ratio ρ_j/ρ_2 also has no noticeable effect. There appears to be a value of pressure ratio $p_j/p_2 \approx 0.3$ near which penetration is optimized, which may be associated with "pressure matching" of the jet. Nonetheless, the difference in penetration between underexpanded and "pressure-matched" jets, at the same value of J , is rather small. The flow is found to be highly unsteady, a feature that may significantly affect mixing and combustion.

2.8 RECOMMENDATIONS FOR FOLLOW-ON WORK

The work performed here has helped in establishing the overall trends of supersonic transverse-jet penetration versus flow parameters. However, there are many other aspects of the jet flow that, in our opinion, merit further study. A close study of the turbulent structure of the jet will shed light on its role in entrainment and mixing mechanisms; characterization of the flow unsteadiness is very important for predicting mixing, combustion, and fatigue loads on the combustion chamber; total-pressure loss must be correlated to the main jet parameters, namely momentum ratio and cross-flow Mach number. Finally, the dependence of the above phenomena on jet inclinations other than 90° is crucial in order to identify efficient mixing configurations.

A summary for each of the above areas is presented below, together with suggestions for advanced diagnostic techniques.

2.8.1 Turbulent Structure

The turbulent structure of the transverse supersonic jet has received very little experimental study. Photographs published in the literature represent time-averaged views, with all the turbulent features consequently lost. The pictures obtained in this work show detailed features of the turbulent structure which appears to have a certain degree of organization. The secondary shock waves in the helium-air cases, which are thought to emanate from the turbulent eddies of the jet, are strong evidence that the turbulent structure plays a significant role in the jet development. Yet, we do not precisely know how the structure entrains fluid and how active it is in the mixing process in the near field and far field of the jet.

The design of the UCI Supersonic Turbulence Facility allows the flow to be "cut" with a laser sheet across any desired plane. Planar imaging techniques, discussed below, will reveal the cross-sectional geometry of the structure and the entrainment of cross-flow fluid into the jet fluid. Of interest, for example, is to examine the structure in a plane perpendicular to the jet axis, which may reveal the counter-rotating vortices which theoretical works (Heister and Karagozian [6]) speculate that they dominate the jet far field.

The diagnostic technique that appears most useful for the above investigation is Planar Laser Induced Fluorescence (PLIF). The fluorescing molecule will be biacetyl ($\text{CH}_3\text{COCOCH}_3$), a nontoxic substance that fluoresces in the visible range, with fluorescence lifetimes on the order of 10 ns. Illumination will be provided by frequency-tripled Nd:Yag lasers with pulse energies of about 300mJ at $\lambda = 355\text{nm}$. Two such lasers will be available at UCI for supersonic work. PLIF will not only provide cross-sectional views of the turbulent structure, but will also reveal the entrainment of cross-flow fluid into the jet. Biacetyl can be seeded either in the jet fluid or in the cross-flow fluid. This will allow us to "tag" either fluid and follow its development in the mixing region.

A similar imaging method which does not require seeding is Planar Rayleigh Scattering (PRS). The setup for PRS will be the same as that for PLIF, described above, with the only difference that the Nd:Yag laser will be frequency-quadrupled, producing beams at a wavelength of 266 nm and energy per pulse of 200 mJ. Because most of the supersonic-jet configurations have large gradients of refractive index, PRS is a suitable visualization method for the near-field of the jet.

2.8.2 Shock Structure and Unsteadiness

Using the same diagnostic techniques as in the previous section, the shock structure surrounding the jet will be visualized. Two views will be obtained, the side view depicted in Figure 2.1 and the cross-sectional view depicted in Figure 2.2. For the latter view, only PRS can be used. The side view will reveal the bow shock, whose geometry is directly related to the flow inclination and Mach number just ahead of the jet. The cross-sectional view will provide a real-life comparison with the sketch of Figure 2.2 and thus will be helpful in determining the pressure distribution around the jet perimeter.

An important aspect of the flow is its unsteadiness, which manifests itself through an oscillating bow shock. Unsteadiness may play a significant role on mixing and penetration, likely acting as mixing enhancer. It may also present structural problems due to high transient pressures. By means of sequential instantaneous visualizations of the same test case, making sure that upstream conditions do not vary, shock oscillations will be detected. Rapid-response pressure transducers on the wall will measure the pressure fluctuations. Although the data will not be quantitative enough for a full description of the flow field behind the shock, they will nevertheless indicate the degree of the unsteadiness and to what extent models, all of which so far have assumed steady flow, need to be concerned about it.

2.8.3 Total-Pressure Loss

Any mixing process entails an increase in entropy. In supersonic flow, where mixing is often accompanied by shocks, entropy increase can be dramatic. The jet under study is a notable example of such flow. From a practical standpoint, it is important to find flow configurations where mixing is maximized and energy losses kept to a minimum. The total-pressure loss, which is directly related to the entropy rise, will be measured here by means of pitot-pressure surveys. These surveys will be particularly

useful in the cases with variable injection angle, where optimum configurations will be sought.

2.8.4 Inclination Angle

The advantage of an inclined jet is that part of its momentum directed in the main-flow direction, thus reducing total-pressure loss or even adding thrust to the main flow. The disadvantage is that the momentum normal to the flow is reduced by the factor $\sin^2 \theta_0$, thus degrading penetration. That reduction is severe (more than 50%) if θ_0 exceeds 45 degrees, so it is unlikely that much benefit will occur for angles smaller than that. Obviously, a trade-off study is necessary to see which value of θ_0 provides optimum performance. The study will focus on injection angles of 90, 60, and 45 degrees at several gas-Mach number combinations.

3.0 TASK 2: THEORETICAL STUDY

3.1 SUMMARY

The theoretical and computational research of the transverse liquid injection under the sponsorship of AFWAL is described in this final report. It summarizes the theoretical efforts and numerical results obtained in the past 3 years (with emphasis on more recent developments and results). To understand fully the transverse injection phenomena in a combustion chamber, a three-dimensional analysis is necessary to study the gas-liquid interactions. While theoretical developments are needed for the scope of the problem and to guide our research efforts, the bulk of this project involves numerical simulations; the fluid dynamic interactions between the two immiscible phases are too complex to be treated analytically.

3.2 INTRODUCTION

The fluid dynamic forces on the transverse liquid jet results in a turning of the liquid jet toward the direction of the cross-flow. The turning of the jet and its subsequent mixing with the gas stream are of both practical and academic interest in that many combustion devices are principally of this type and yet little is known about the interactions of the two phases. The transverse injection problem can be reasonably divided into four portions in relation to the position of injection. In the first portion immediately following injection, the liquid jet turns because of the momentum impact and the unbalanced pressure force exerted by the cross-flowing gas. In the second portion, viscous stresses and effects due to the density difference, the relative gas/liquid motion, and the surface tension cause deformation of the jet cross section and give rise to an unstable gas/liquid interface. In the third portion, the dynamic disturbances to the interface lead to breakup of the jet into ligaments. The final portion involves further breakup of the ligaments into droplets and, in the case of heat transfer, the evaporation of the droplets.

Bergeles et al. [11] utilized a three-dimensional finite-difference method to simulate the cooling effectiveness of air injected through a double-row of discrete holes into an air stream over a flat plate. Karagozian [12,13] used a two-dimensional vortex model to simulate a turbulent jet injected into a uniform cross-flow. The vortex model was comprised of a pair of counterrotating vortices. Fearn and Weston [14] also employed a vortex pair model to simulate numerically a turbulent jet into a cross-stream. Their techniques required velocity measurements to complete the model and were, therefore, semi-empirical. Krothapalli et al. [15] experimentally studied the separation phenomena of a uniform air stream ahead of a rectangular jet. A horseshoe-type vortex system rising from the near wake region was observed for a jet-to-air velocity ratio less than 5. Beyond this value, the flow structure behind the jet exit exhibited periodic shedding of asymmetrical vortices from the ends of the rectangular jet slot. All of the above publications dealt only with gaseous injections and, hence, no sharp interfaces were present in their problems.

Heister et al. [16] expanded on the early model of Karagozian and applied it to the problem of a liquid jet transversely injected into a supersonic gas flow. They postulated that the shape of the jet cross section was an ellipse and that the ratio of the semimajor axis to semi-minor axis remained constant when liquid shedding and vaporization were considered. Moreover, it was only a one-way model since the presence of the jet did not influence the gas-phase solution (flow through a bow shock), thus de-coupling the interference between the two phases. Adelberg [17], based on early gravity waves models, suggested an analytical criterion by which one could separate acceleration waves caused by unbalanced pressure forces from capillary waves by gravity. A semi-empirical model was developed in this research to predict the penetration of a liquid jet into a supersonic gaseous

stream. Broadwell and Breidenthal [18] derived two simple formulae to predict the locus of the center of a liquid jet and the separation distance between two counterrotating vortices in the jet far away from the point of injection. However, there were still two constants to be determined experimentally in their model. Kamotani and Greber [19] also observed that a turbulent jet in a cross-flow deformed into a horseshoe or kidney type of twin vortex structure. Less et al. [20] indicated via experiments that the jet-to-cross-flow dynamic pressure ratio is important in predicting the structure and behavior of the liquid jet.

Semi-empirical models suffer a lack of universality. This predicament manifests itself most seriously when considering parametric studies. Simplified theoretical models suffer the same disadvantage and can only provide some global features of the flow, but they are not accurate quantitatively. The barrier to make a complete two-way model (i.e., the liquid jet and the cross-flowing gas stream responding dynamically to each other's presence) is mainly due to the complex interactions between the two immiscible phases. The fact that computations of this nature demand considerable resources, both in memory and CPU time, also contributes to the difficulty in making a successful model. The availability of supercomputers would alleviate concerns for computational resources. Advancement in increasing the capability of real time interaction between computations and graphical representations can enhance the research progress even further. As for the two-phase problem itself, technically speaking, the issues of maintaining the phase discontinuity and conserving mass remain as the two most important subjects. The two subjects are particularly menacing in the transverse injection study, as compared to a two-dimensional co-flowing case, because the transverse injection problem doesn't have an exact initial state and, in spite of liquid high density, the total liquid mass concerned only constitutes a minor fraction of the entire system mass.

In the rest of this report, the transverse injection research is subdivided into a number of phases, corresponding to activities in various periods during the past three years. Phases in the first year are only summarized here with results presented in the Appendices. Previous annual/progress reports contain more in-depth information for the period. The focus of this report is on the activities of the final 2 years when most of the two-phase model was developed and numerical simulations having direct bearing on the transverse injection problem were conducted.

3.3 THEORY AND COMPUTATIONS

3.3.1 Phase I

A computer code for three-dimensional laminar elliptic flows was adopted in the initial stage of the research and several test runs were conducted with this code. These test runs were designed to debug the computer program because the code was keyed in manually. The main body of work in this phase included debugging in both compilation and run time, and accuracy check by test results. The test cases involved simple channel flows, having known exact solutions, with varied axial flow directions. These tests were necessary to ensure the program had no typographical errors in all three orthogonal directions and to help a user to become familiar with the coding.

The flow considered was that inside a three-dimensional rectangular channel. The flow with a uniform axial velocity component entered the semi-infinite channel and its subsequent development was calculated. The flow was laminar and governed by the continuity and Navier-Stokes equations, subject to proper boundary conditions. Even though one of the dimensions of the channel was infinite, the momentum conservation equation for that direction was kept in the simulation to achieve the objectives stated in the previous paragraph. Three tests were conducted, each having a

flow developing along one of the Cartesian directions, but only results of one test are attached in Appendix B. The results have shown that the code was able to predict the flow development correctly and give a zero solution of the velocity component in the direction which extended to infinity.

3.3.2 Phase II

Having completed debugging the adopted 3-D code, the rectangular channel would serve as a basic configuration for ensuing numerical tests. The tests designed in this phase were flows of gaseous jets transversely injected into a cross-flowing gas stream inside the rectangular channel. The injection geometry was chosen such that the flow field was symmetrical with respect to two parallel Cartesian planes in order to save computational costs. For simplicity, imaginary gases were used to attain laminar flows while the gas densities and injection and inlet velocities could be varied. The heavier the injectant was, the closer the simulation result would be to the actual liquid/gas configuration. Therefore, the tests provided us with preliminary estimates about jet bending and penetration. Gaseous injectants might be relevant, too, in practical situations where, for example, hydrogen fuel is used as the injectant.

The geometry considered was a rectangular channel with a circular orifice where gases with a higher momentum flux were injected into the channel. The diameter of the injection orifice was 0.002 m and the center of the injection orifice was situated 5 diameters downstream from the channel inlet. The computational domain was 30 diameters in the axial (z) dimension, 20 diameters in the transverse direction (y) and 10 diameters in the third dimension (x). The cross-flow entered the channel with a uniform velocity of 1 m/s. A schematic of the geometry is shown in Figure 3.1, where the sharp boundary between the gas jet and the cross-flow is exaggerated. The flow field was governed by the continuity and Navier-Stokes equations, subject to proper boundary conditions. To ensure mass conservation for individual species, a species conservation equation was also required.

Three test cases were investigated in this phase. The injection speed was 2 m/s for the first two cases and 1 m/s for the third case. The injectant density to cross-flow density ratio was also varied between 5 to 100. A ratio of the order of 100 is closer to a liquid/gas configuration. The above specified conditions rendered the momentum flux ratio to vary between 4.5 and 10, which is a typical range for subsonic flows. The flow circulation inside the concentrated portion of the jet could also simulate the actual internal circulation in a liquid jet. A few typical results from the test, which had a momentum flux ratio of 10, are presented in Appendix C. Detailed discussions about all results can be found in the report entitled "Computational Research on Liquid and Heavy Gas Jets Injected into a Crossflow," which was previously submitted to the AFWAL.

3.3.3 Phase III

With the knowledge of the gas-to-gas injection problem, the research was carried forward to the liquid-to-gas problem. Unlike the gas-to-gas cases, the cross-flowing gas now cannot diffuse into the liquid phase and a sharp phase discontinuity should be present in the flow. Conventional numerical techniques cannot preserve the discontinuity to satisfaction and a numerical technique suitable for this problem was needed. Before venturing further into the two-phase simulation, some basic physical laws that govern the state of the flow and the numerical techniques and algorithm will be introduced briefly in the following paragraphs.

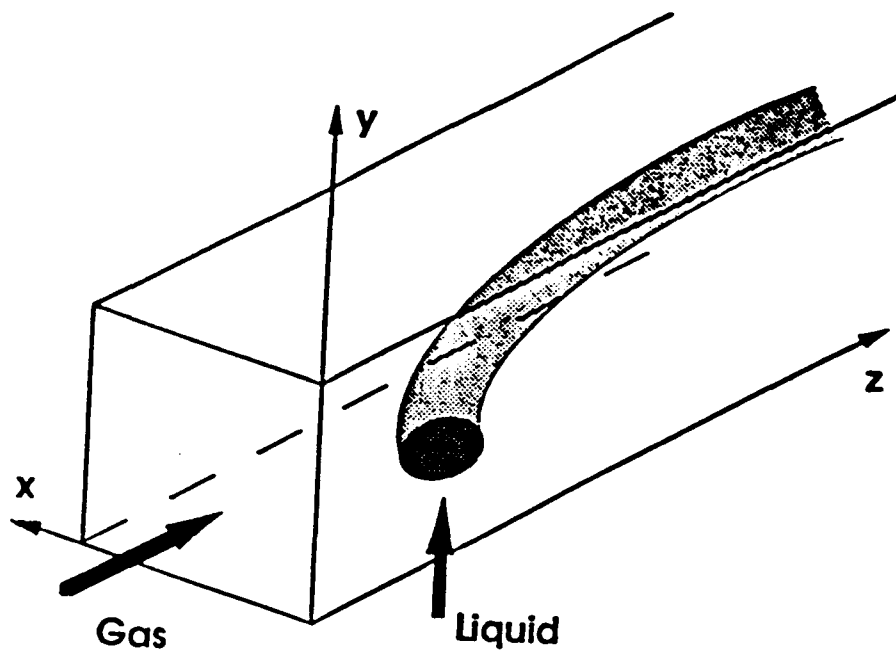


Figure 3.1: Geometry concerned and the coordinate system used.

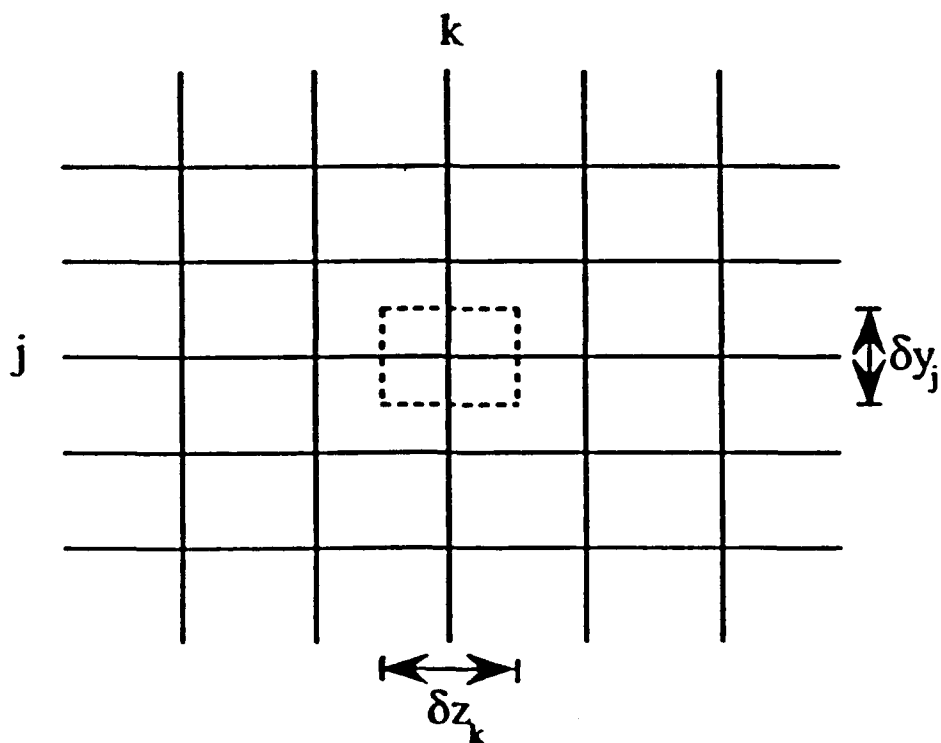


Figure 3.2: A representative 2-D computational cell.

The two basic principles that a flow must follow are the conservation of mass and the conservation of momentum (Newton's second law of motion). In a multiphase system, not only must the total system mass be conserved but the mass of each individual phase, after accounting for phase transitions and/or chemical reactions, has to be conserved too. The above three principles can be translated into the following three differential equations which govern the state of a flow when there is no phase transition or chemical reaction:

$$\frac{D\rho}{Dt} = -\rho(\nabla \cdot \vec{V}) \quad (1)$$

$$\rho \frac{D\vec{V}}{Dt} = -\nabla p - [\nabla \cdot \vec{\tau}] \quad (2)$$

$$\frac{DF}{Dt} = 0 \quad (3)$$

where the following definitions are made:

$\frac{D}{Dt}$	substantive derivative
F	volume fraction of the liquid phase
p	pressure
t	time
\vec{V}	velocity vector
ρ	density
$\vec{\tau}$	stress tensor

In relation to the transverse injection problem at hand, the incompressibility and constant temperature conditions are also assumed in formulating the above equations.

The complexity of the transverse injection problem, which has no two-dimensional simplification, renders itself only suitable for numerical solution. In a

numerical simulation, the derivatives in the governing equations are replaced by approximate formulae. For instance, one can use Taylor series expansions to estimate those derivatives. For a complex problem, more elaborate approximations are needed in order to eliminate the possibility of divergence and attain more accurate results. For the transverse injection problem, a control volume approach was chosen and the derivatives at the control volume faces were estimated by the hybrid scheme [21]. A control volume is an imaginary volume surrounding a numerical grid in a discretized solution domain. A numerical simulation seeks solutions of the dependent variables at each grid.

Upon substituting approximate formulae for the derivative terms in the governing equations and rearranging, an algebraic equation per dependent variable is obtained for each numerical grid in terms of its neighbors. The algebraic equations can be expressed generally by the following expression:

$$(A_P - S_P \Delta v) \phi_P = A_E \phi_E + A_W \phi_W + A_N \phi_N + A_S \phi_S + A_T \phi_T + A_B \phi_B + (S_C \Delta v + A_P^0 \phi_P^0) \quad (4)$$

and:

$$A_P = A_E + A_W + A_N + A_S + A_T + A_B + A_P^0$$

where ϕ can be any dependent variable, Δv is the control volume, and A_i are expressions, containing physical properties, velocity components and dimensions of a control volume, resulting from the hybrid scheme. The subscripts P, E, W, N, S, T and B refer to the grid concerned, the eastern face, the western face, the northern face, the southern face, the top face, and the bottom face of a rectangular control volume, respectively. They also represent neighboring computational grids when they are associated with a dependent variable. The superscript 0 denotes quantities from a previous time step. $(s_P \phi_P + S_C)$ is a linearized source term. It represents various stress derivatives in the momentum equations. The total number of algebraic equations like Equation (4) equals the number of grid points in the solution domain times the number of dependent variables. These algebraic equations are solved simultaneously and iteratively until convergence, subject to the boundary conditions and initial conditions of the transverse injection problem.

The solution procedures adopted in this research are based on the SIMPLE [21] algorithm. It includes the following iterative steps:

1. Guess a pressure field;
2. Solve the momentum equations;
3. Solve a pressure-correction equation (continuity equation);
4. Correct the pressure and the velocity field with results from step 3;
5. Solve for the mass (volume) fraction of the liquid phase;
6. Reconstruct the phase discontinuity based on the solution from step 5;
7. Treat the corrected pressure field as a new guess and return to step 2; repeat the process until converged solutions are obtained for all dependent variables.

The grid system employed in the computer code is rectangular and staggered. A staggered grid system is one in which the velocity control volumes are offset by one-half grid spacing in each of the Cartesian directions with respect to the scalar control volume, which surrounds a numerical grid.

Much effort was devoted to preserving the phase discontinuity across the gas/liquid interface. In this preliminary two-phase simulation, the cell density and viscosity were evaluated by the following formulae [22]:

$$\rho = \alpha\rho_l + (1.0 - \alpha)\rho_g \quad (5)$$

$$\mu = \alpha\mu_l + (1.0 - \alpha)\mu_g \quad (6)$$

where α is the volume fraction and μ is the viscosity. A donor-acceptor prescription was employed by which the density at the cell boundary was calculated according to the following equation:

$$\rho_{cb} = \rho_D \quad \text{if } \alpha_D = 0. \text{ or } \alpha_D = 1.0 \text{ or } |\alpha_D - \alpha_A| < 0.001 \quad (7)$$

$$\rho_{cb} = (1.0 - \alpha_A)\rho_{Dg} + \alpha_A\rho_{Dl} \text{ otherwise}$$

where subscripts D and A denote donor and acceptor cells, respectively. The donor or acceptor status of a cell with respect to its neighbors was established by the velocity vector at the cell faces. The phase discontinuity was not explicitly defined in this scheme. Rather, it could only be deduced indirectly from the distribution of the physical properties (e.g., density).

Excerpts of the results obtained using the above scheme (without explicitly defining the phase discontinuity or satisfying interface boundary conditions) are presented in Appendix D. Overall, the above scheme could not avoid artificial diffusion (numerical smearing) except near the orifice of injection and, therefore, it cannot be used to study jet penetration and distortion. Because of the ambiguity of the position of the phase discontinuity, the investigation of surface instabilities along the interface will be impossible. This leads to the development of a better scheme in Phase IV.

3.3.4 Phase IV

A new way of tracking the interface must be devised to minimize numerical smearing effects. This can be achieved by explicitly defining the sharp phase discontinuity from the solution of Equation (3). Once the interface is constructed according to the marker solution, the cells inside the region bounded by the interface will take on the liquid density value while cells outside the region assume the gas density value. This is different from the method in Phase III where the density of a cell was calculated according to Equations (5) and (7) without regard to the location of the interface. The following paragraphs describe this surface-constructing method in greater detail.

An essential requirement in simulating a two-phase flow is to preserve the integrity of each phase. Most existing numerical techniques for immiscible two-phase flows fail when applied to a three-dimensional problem. For instance, the method of using a height function to describe the phase discontinuity cannot overcome the difficulty of the multiplicity nature of the interface. Another example would be to use the Lagrangian frame of reference to follow the interface, but this method becomes extremely cumbersome and time-consuming for a three-dimensional problem. In addition, it cannot handle a problem which does not have an exact initial state. A brief literature survey revealed that there was only one research group at Los Alamos that has continually undertaken, through a span of about two decades, this phase of gas-liquid interface preservation in numerical simulations. An Eulerian method, Volume of Fluid (VOF) [23], developed by the Los Alamos group, has undergone substantial testing and given satisfactory results in all two-dimensional tests. This method, therefore, is adopted as the interface-tracking method for the transverse injection problem.

The principal procedures of the VOF method involve solving for the volume fraction of the liquid phase and then constructing the phase discontinuity according to the distribution of the volume fraction. Once the interface is established, the physical properties within a computational cell and mass and momentum fluxes crossing cell boundaries can be evaluated precisely without introducing artificial smearing. A two-dimensional example is given here to describe how the interface is constructed. A typical two-dimensional computational control volume of a scalar is depicted in Figure 3.2. Similar cells like this spread across the entire calculation domain. The center of each cell is associated with a particular liquid volume fraction that comes from the species conservation principle. A line segment in a 2-D computational cell can be approximated by either:

$$Z(y_{k,j}) = F(k-1,j)\delta z_{k-1} + F(k,j)\delta z_k + F(k+1,j)\delta z_{k+1}$$

or:

$$Y(z_{k,j}) = F(k,j-1)\delta y_{j-1} + F(k,j)\delta y_j + F(k,j+1)\delta y_{j+1}$$

where Z and Y are relative locations of the interface in the cell. If one assumes that the grid spacing is constant and that z is equal to y , the slope of the line segment can be approximated by:

$$\left(\frac{dY}{dz}\right)_{k,j} = 2[Y(z_{k+1,j}) - Y(z_{k-1,j})] / (\delta z_{k+1} + 2\delta z_k + \delta z_{k-1})$$

$$\left(\frac{dZ}{dy}\right)_{k,j} = 2[Z(k,y_{j+1}) - Z(k,y_{j-1})] / (\delta y_{j+1} + 2\delta y_j + \delta y_{j-1})$$

depending on which representation of the line segment is chosen. However, experience [23] has shown that the derivative with the smallest magnitude best approximates the slope of the interface because the corresponding Z or Y expression is more accurate.

The next step is to decide on which side the liquid resides. Suppose dZ/dy is the smallest in magnitude (so that the surface is more vertical than horizontal) and chosen

as the slope of the interface in the cell. If dY/dz is negative, liquid is on the left side of the interface. Otherwise, the liquid resides on the right side of the cell. On the other hand, if dY/dz is chosen as the slope of the interface in the cell, a negative dZ/dy indicates that liquid resides below the phase discontinuity. Once the slope of the surface and the side occupied by the liquid are determined, a line can be drawn with the correct amount of volume for the liquid in the cell. The phase discontinuity is then obtained by joining the line segments within computational cells together. In extending this scheme to the three-dimensional situation, the line is interpreted as a surface segment. In other words, it is assumed that there is no variation of the volume fraction in the third direction within one cell. The three-dimensionality of the problem is not lost with this assumption because it is essentially a problem of grid resolution and is common in all numerical simulations.

The VOF method was incorporated into the solver used in Phase III and a liquid transverse injection problem was tested. The governing equations for this problem are the same as those listed in Phase III. F can be interpreted as the liquid volume fraction, but it can also be treated simply as a numerical marker that gives both the position and quantity of the liquid. Its magnitude varies between 0 and 1. It is zero when a cell is empty of liquid and unity when a cell is full of liquid. A cell is partially-filled if the F value is between zero and unity. The density is still kept in the equations because it varies in cells through which the liquid/gas interface passes, even though the compressibility is neglected in both phases. The density of a cell is related to the volume fraction by:

$$\rho = \rho_l F + (1 - F)\rho_g \quad (8)$$

To avoid excessive numerical smearing, a special advection method, called the donor-acceptor fluxing scheme [23], was employed to update F at step 5 of the solution procedures stated in Phase III. This advection method uses the fact that a change of F in a Cartesian control volume (cell) is equal to the summation of the fluxes through the six cell faces, and it also takes into account the orientation of the interface within a cell in calculating those fluxes. The amount of F fluxed across one cell face according to this method is estimated by the following formula:

$$\Delta F = \text{MIN}\{F_{AD}(|v|\delta t)(\text{AREA})_l + \delta F, F_D \Delta v\} / \Delta v$$

where

$$\delta F = \text{MAX}\{(1 - F_{AD})(|v|\delta t)(\text{AREA})_g - (1 - F_D)\Delta v, 0\}$$

The subscripts D and A denote the donor cell and the acceptor cell. The double subscript AD refers to either A or D depending upon the orientation of the interface relative to the direction of flow. $AD=A$ when the liquid/gas interface is convected mostly normal to itself; otherwise $AD=D$. (AREA) is the projected area of the interface on the cell face and $(\text{AREA})_g$ is the complement of it; v is the velocity component normal to the cell face and Δv is the volume of the donor cell. MAX and MIN are functions which return the maximum and minimum values of functions arguments.

Now, we refer to Figure 3.1 for the schematic of the test problem. The flow is three-dimensional and subsonic. In fact, a two-dimensional simplification of this problem (transverse injection) does not exist because the region behind and beneath the jet would have been an undefined region (a void) in that case. To minimize the computational efforts, the actual computational domain consisted of two planes of symmetry. First, the

top of the channel was taken as a symmetry plane. The second plane of symmetry sliced the liquid jet in halves in the z direction. Therefore, only half of the jet shown in Figure 3.1 was included in the actual calculation. The diameter of the injector was 0.003 m and its center was 5 injector diameters downstream from the channel inlet. The y dimension (height) of the computational domain was 20 diameters, the length (z) 30 diameters and the width 10 diameters. The flow under consideration corresponded to the following specified conditions:

$$\begin{aligned} v_j &= 1 \text{ m/s} \\ \rho_g &= 1 \text{ Kg/m}^3 & \rho_j &= 5 \text{ Kg/m}^3 \\ \text{Re}_g &= 40 & \text{Re}_j &= 100 \end{aligned}$$

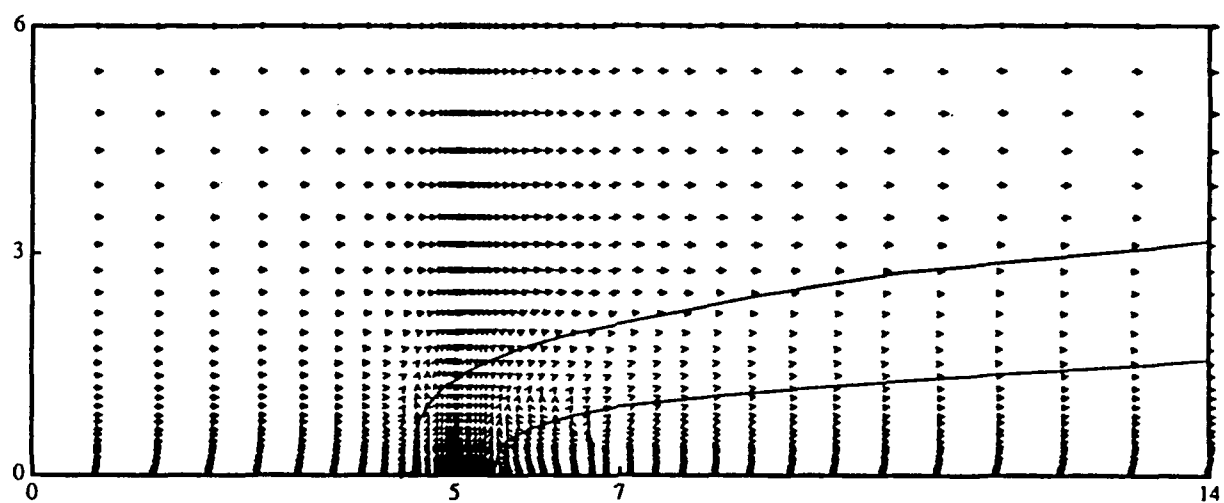
The subscript j refers to the liquid jet. The Reynolds numbers listed above were based on the injector diameter. The jet-to-gas momentum flux ratio of this flow can be defined as follows:

$$M = \sqrt{\frac{(\rho v^2)_j}{(\rho w^2)_g}}$$

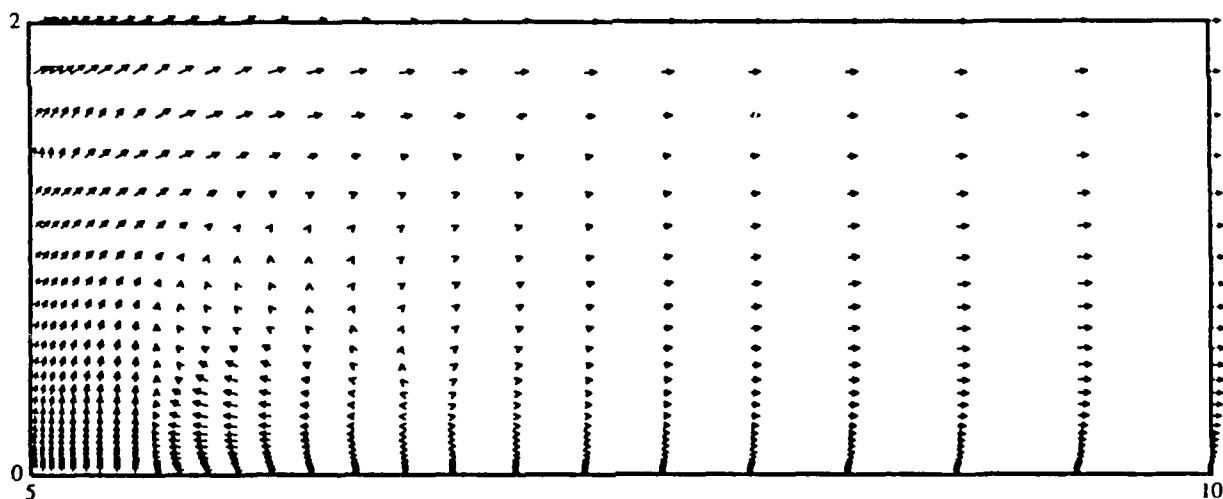
and equals 3 for this test case. Note that the definition above equals the square root of that of Less and Schetz [20]. The surface tension effects were not included in the calculation and the pressure was assumed to be uniform in a partially-filled control volume.

Two-dimensional projections of the velocity fields and the jet cross sections are shown here. Referring to Figure 3.1, the x direction is now denoted as the spanwise direction, the y direction as the transverse direction, and the z direction as the axial direction of the domain of interest. Figure 3.3a shows the jet cross section and the velocity field at 0.15 injector diameter away from the center of the jet in the spanwise direction. The gas flow is deflected both in the transverse and spanwise directions. A recirculating region behind the jet column can be better visualized in Figure 3.3b, which is an enlargement of the region. Figure 3.4a shows another z-y cross-sectional plot of the jet and the velocity vector at 0.32 injector diameter in the spanwise direction. The cross section of the jet has tapered and the maximum speed of the gas has decreased because of reduced axial acceleration (the spanwise velocity acceleration is increasing). A recirculation underneath the jet, enlarged in Figure 3.4b, can also be observed and is larger than the one shown in the previous figures. Notice that the mean radius of curvature of the jet near the injector is of comparable magnitude to the injector diameter.

In order to interpret the vector plotting routine, certain facts should be understood. The velocity magnitude is proportional to the length of the tail of the arrow; the overall length including the length of the arrowhead is not of consequence. The location of the numerical node where the velocity is calculated is at the base of the tail. Consequently the details are not always represented well in plots like Figure 3.3a or 3.4a. Certainly, no mass crosses the jet boundary when resolution is made on a scale smaller than the arrow itself.

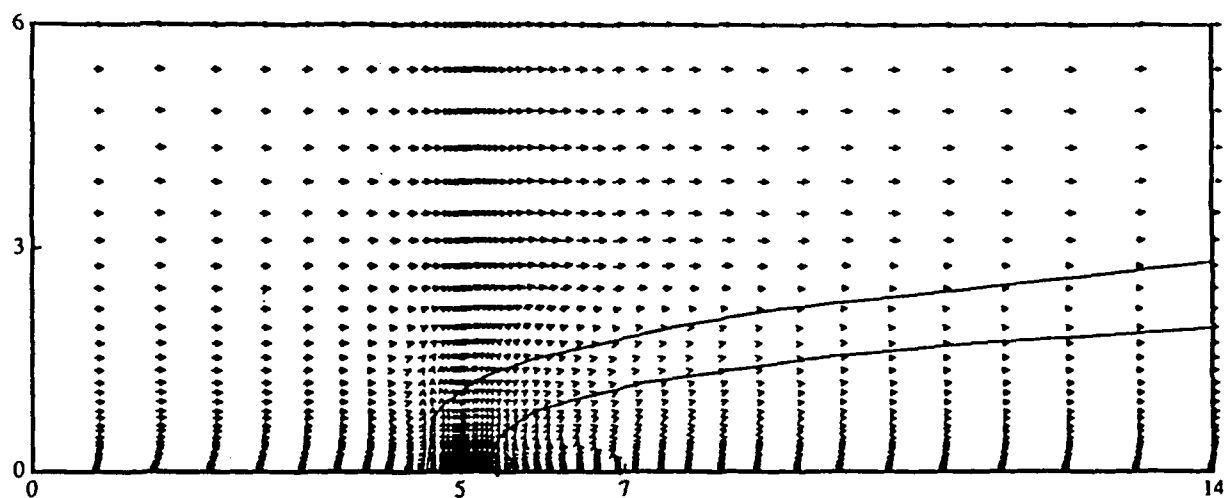


(a)

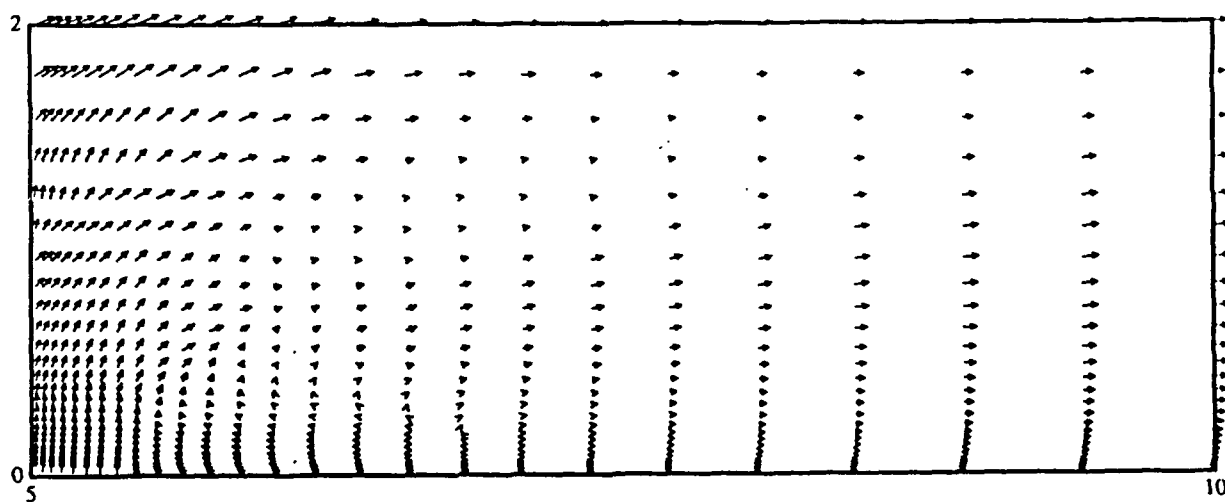


(b)

Figure 3.3: (a) Velocity vector and jet cross section at $x=0.15 d$;
Max. vector=1.71 m/s.
(b) Enlargement of the recirculation region;
Max. Vector=1.15 m/s.



(a)



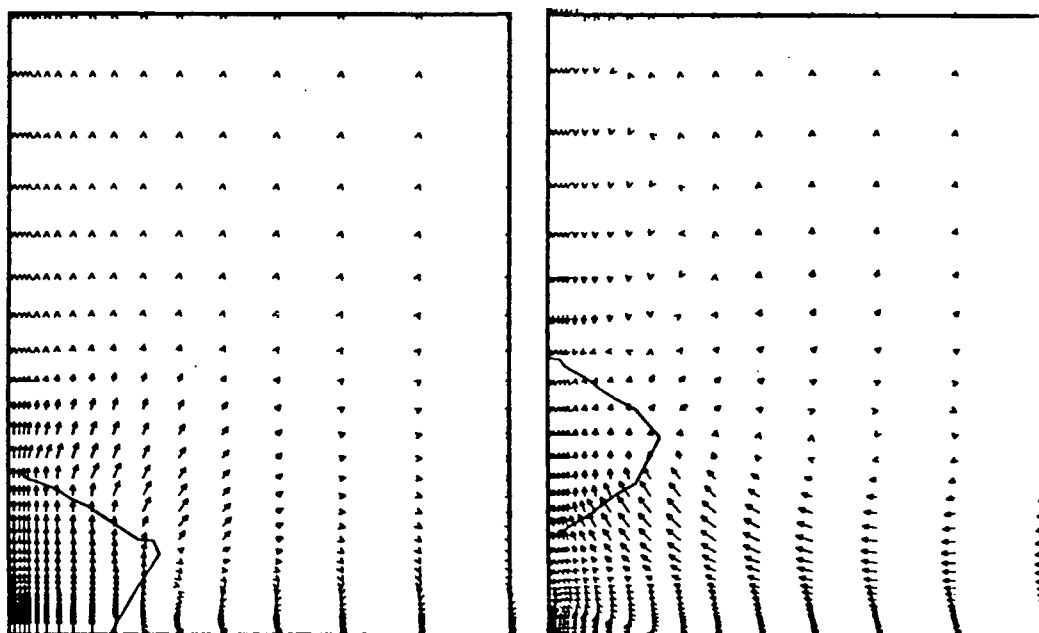
(b)

Figure 3.4: (a) Velocity vector and jet cross section at $x=0.32 d$;
Max. vector=1.35 m/s.
(b) Enlargement of the recirculation region;
Max. vector=1.17 m/s.

Figure 3.5a shows the jet cross section and the velocity field in a x - y plane at a distance of 0.78 injector diameter from the leading edge of the injector in the axial direction. The liquid jet is injected upward from the lower left-hand corner of the plot and the cross-flowing gas is in the direction perpendicular to the page (outward). The deflection of the gas mass by the injection of the liquid is vividly shown in this figure. The gas is deflected both upward and sideward and the jet at this axial location expands slightly in the spanwise direction. Part of the sideward-deflected gas flows downward and a clockwise-circulating vortex is in its early stage of formation near the bottom of the chamber. Figure 3.5b shows the flow pattern and the jet cross section at an axial location 4.5 injector diameters downstream from the leading edge of the injector. The clockwise-circulating vortex has lifted off the channel bottom and is partially responsible for the rise of the jet column. There is an additional circulating vortex just above the liquid mass in this cross section. This counterclockwise vortex is formed by the gas deflected upward early on and its strength is smaller than that of its clockwise counterpart. Figure 3.5c shows the flow and the jet at 19.25 diameters downstream from the leading edge of the injector. The jet has risen even higher and the clockwise-rotating vortex has moved almost completely out of the domain represented by this figure. The jet cross section has elongated in its transverse dimension and shrunk in the spanwise dimension. The velocity vectors shown in the plot are minuscule compared to those in the previous two figures, indicating a subsiding interaction between the cross-flow and the injection, although the basic flow structure resulting from the interaction still persists. In reality, the liquid jet may not survive this far downstream without fragmentation.

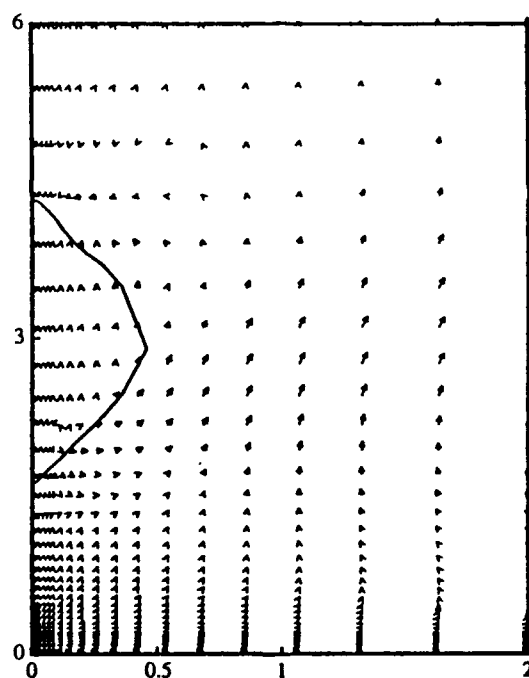
Figure 3.6a shows the velocity field in a horizontal (z - x) plane that is 0.1 injector diameter above the channel bottom. The cross-flow is from left to right and the liquid jet column extends perpendicularly out of the plane of the page. Behind the injector, the cross-flowing gas forms a wake region that is similar to the classical wake of a flow passing a two-dimensional circular cylinder, except there are severe wall influence and injection in the current flow. The wake can be seen more clearly in Figure 3.6b that magnifies the region. In fact, the wake at this transverse location also interchanges momentum and mass with the two recirculating vortices in the z - y and x - y planes, as shown in Figure 3-5, not merely with wakes at other transverse locations (as it is in the classical case). The flow resumes in the axial direction after about two injector diameters from the center of the injection.

There are at least three major circulating vortex systems present in the flow. They all initiate around the injection region. Two of them (one in z - x horizontal cross sections, Figure 3.6, and one in z - y vertical cross sections, Figure 3-4) exist within about 2 injector diameters after the injection and interact with each other and with the third system in the x - y cross sections (Figure 3.5) vigorously. The high shear created by this complicated interaction may play a major role in fragmenting the jet within a few diameters of axial distance in practical applications. This raises a serious doubt of the applicability of a locally two-dimensional model, as in other studies [6, 8], to this flow where the mean radius of curvature of the jet near the injector is comparable to the injector diameter. The numerical calculation assumes a constant velocity profile in a surface cell across the interface. This is a crude approximation when the jet-to-gas viscosity and density ratios are high. It can also jeopardize the ability to predict the surface motion in those situations where the phenomena of liquid breakup are to be considered. These concerns will be addressed in the next phase.



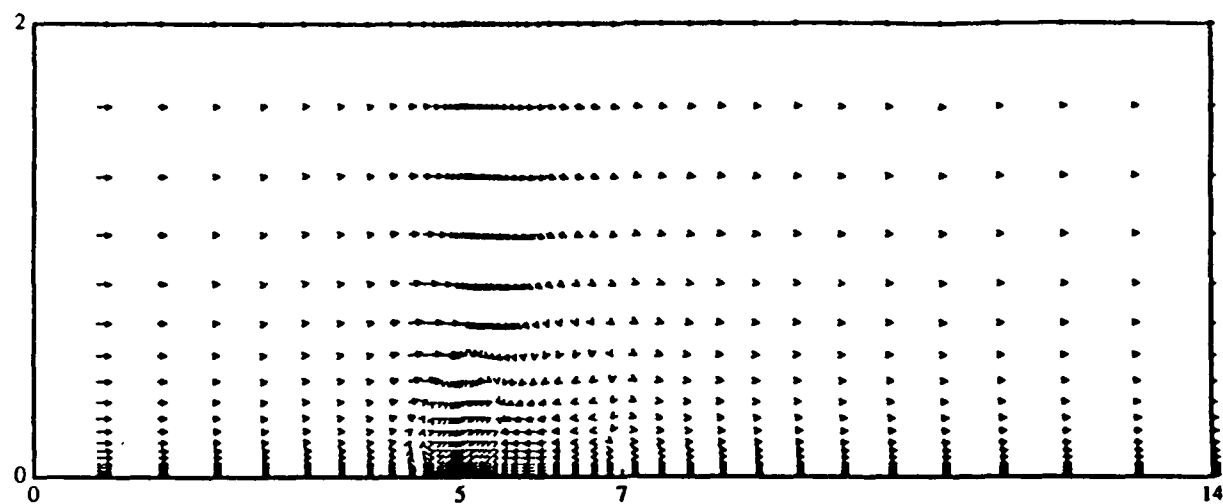
(a)

(b)

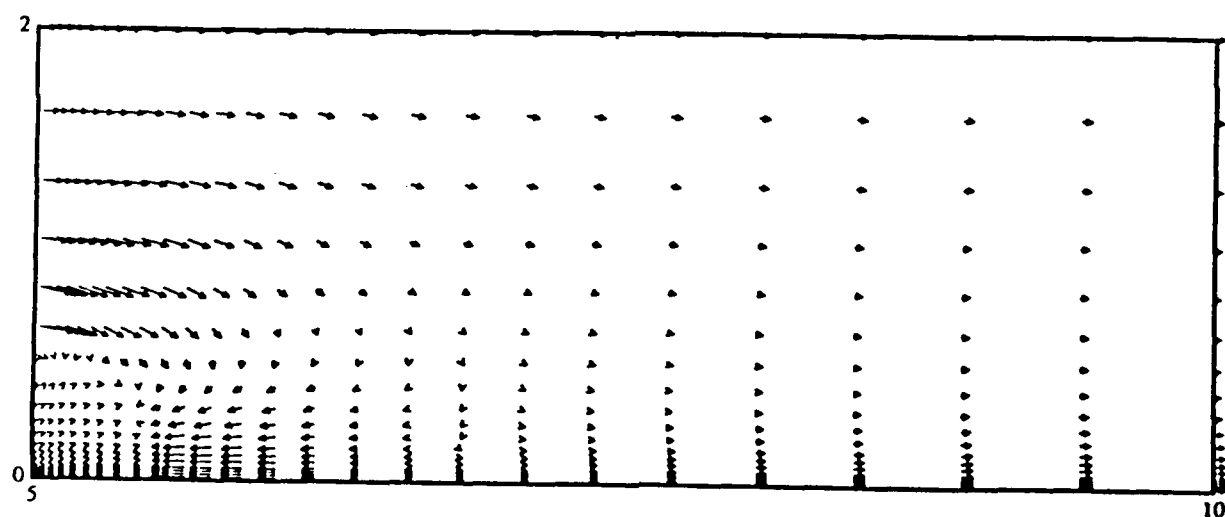


(c)

Figure 3.5: (a) Velocity vector and jet cross section at $z=5.28$ d;
Max. vector=1.61 m/s.
(b) Velocity vector and jet cross section at $z=9.0$ d;
Max. vector=0.23 m/s.
(c) Velocity vector and jet cross section at $z=23.75$ d;
Max. vector=0.03 m/s.



(a)



(b)

Figure 3.6: (a) Velocity vector at $y=0.1$ d; Max. vector=1.02 m/s.
 (b) Enlargement of the wake region; Max. vector=0.78 m/s.

3.3.5 Phase V

The two-phase model in Phase IV used a crude approximation to treat the interfacial stress conditions. The model calculated the intersections of the interface segment with the left and the right cell boundaries and, from knowledge of which side the liquid occupied, mass and momentum fluxes. Stress quantities were calculated by using averaged viscosity coefficients and the velocity solutions. These mass and momentum fluxes and stresses were fed back into the iterative procedures and new values of the velocity components and liquid volume fraction were generated. The method described above satisfied the boundary conditions required at the interface, namely, velocity and stress continuity across the phase interface, but the values of those quantities were only approximate. Moreover, the procedure allowed a surface cell density to directly participate in the liquid/gas interface dynamics. This had an effect of smearing the physical processes at the discontinuity and, generally, stiffening the matrix solver in the solution procedures.

The dynamics at the material interface require that the stress tensor be continuous across the surface. There are three types of forces at work in general. They are the viscous force, the fluid dynamic pressure force, and the surface-tension force. Among them, the viscous force acts both perpendicularly and tangentially to the material interface, but the pressure force and the surface-tension force act only perpendicularly to the surface. The balance between the three forces perpendicular to the interface and the continuity of the tangential viscous force at the surface govern the dynamic behavior of fluids in the vicinity of the material interface. Note that fluid densities do not come into play in the dynamics of interface boundary conditions.

The improvement over the model in Phase IV calls for a complete separation of the two immiscible phases in the calculation. This is achieved by formulating the exact and complete boundary conditions at the liquid/gas interface: first, in a generalized coordinate system and, subsequently, in the Cartesian coordinate system to suit our calculation. This complete formulation includes surface-tension effects. The physical statement in the last paragraph can be written mathematically as the following three equations:

$$\mu_1 \left. \frac{\partial V'}{\partial n} \right|_1 = \mu_g \left. \frac{\partial V'}{\partial n} \right|_g + \frac{1}{2} (P_1 - P_g + S) \quad (9)$$

$$\mu_1 \left(\frac{\partial U'}{\partial n} + \frac{\partial V'}{\partial \eta} \right)_1 = \mu_g \left(\frac{\partial U'}{\partial n} + \frac{\partial V'}{\partial \eta} \right)_g \quad (10)$$

$$\mu_1 \left(\frac{\partial W'}{\partial n} + \frac{\partial V'}{\partial \zeta} \right)_1 = \mu_g \left(\frac{\partial W'}{\partial n} + \frac{\partial V'}{\partial \zeta} \right)_g \quad (11)$$

where n , η and ζ are the local normal, first tangential and second tangential directions in the generalized coordinate system. Furthermore, the unit vector in the n direction is specifically defined to be always pointing outwardly into the gas phase for convenience. V' , W' and U' are velocity components in the n , η and ζ directions; P and S are the fluid dynamic pressure and the surface-tension pressure. The subscripts g and l denote the gas and liquid phases, respectively.

Because the computational domain is Cartesian, the above three relations have to be transformed back to the Cartesian frame. The final working equations thus become

$$\begin{aligned} \mu_g(a_1 U_g + a_2 V_g + a_3 W_g) + \mu_g \Omega_{lg} = \mu_l(a_1 U_l + a_2 V_l + a_3 W_l) \\ + \mu_l \Omega_{ll} + \frac{1}{2}(P_g - P_l + S) \end{aligned} \quad (12)$$

$$\mu_g(b_1 U_g + b_2 V_g + b_3 W_g) + \mu_g \Omega_{2g} = \mu_l(b_1 U_l + b_2 V_l + b_3 W_l) + \mu_l \Omega_{2l} \quad (13)$$

$$u_g(c_1 U_g + c_2 V_g + c_3 W_g) + \mu_g \Omega_{3g} = \mu_l(c_1 U_l + c_2 V_l + c_3 W_l) + \mu_l \Omega_{3l} \quad (14)$$

where U , V and W are velocity components in the x , y and z directions, respectively. Coefficients a , b and c are equal to:

$$a_1 = D_{n1} \frac{\partial D_{n1}}{\partial x} + D_{n2} \frac{\partial D_{n1}}{\partial y} + D_{n3} \frac{\partial D_{n1}}{\partial z}$$

$$a_2 = D_{n1} \frac{\partial D_{n2}}{\partial x} + D_{n2} \frac{\partial D_{n2}}{\partial y} + D_{n3} \frac{\partial D_{n2}}{\partial z}$$

$$a_3 = D_{n1} \frac{\partial D_{n3}}{\partial x} + D_{n2} \frac{\partial D_{n3}}{\partial y} + D_{n3} \frac{\partial D_{n3}}{\partial z}$$

$$b_1 = D_{n1} \frac{\partial D_{\eta 1}}{\partial x} + D_{n2} \frac{\partial D_{\eta 1}}{\partial y} + D_{n3} \frac{\partial D_{\eta 1}}{\partial z}$$

$$+ D_{\eta 1} \frac{\partial D_{n1}}{\partial x} + D_{\eta 2} \frac{\partial D_{n1}}{\partial y} + D_{\eta 3} \frac{\partial D_{n1}}{\partial z}$$

$$b_2 = D_{n1} \frac{\partial D_{\eta 2}}{\partial x} + D_{n2} \frac{\partial D_{\eta 2}}{\partial y} + D_{n3} \frac{\partial D_{\eta 2}}{\partial z} \\ + D_{\eta 1} \frac{\partial D_{n2}}{\partial x} + D_{\eta 2} \frac{\partial D_{n2}}{\partial y} + D_{\eta 3} \frac{\partial D_{n2}}{\partial z}$$

$$b_3 = D_{n1} \frac{\partial D_{\eta 3}}{\partial x} + D_{n2} \frac{\partial D_{\eta 3}}{\partial y} + D_{n3} \frac{\partial D_{\eta 3}}{\partial z} \\ + D_{\eta 1} \frac{\partial D_{n3}}{\partial x} + D_{\eta 2} \frac{\partial D_{n3}}{\partial y} + D_{\eta 3} \frac{\partial D_{n3}}{\partial z}$$

$$c_1 = D_{n1} \frac{\partial D_{\zeta 1}}{\partial x} + D_{n1} \frac{\partial D_{\zeta 1}}{\partial y} + D_{n3} \frac{\partial D_{\zeta 1}}{\partial z} \\ + D_{\zeta 1} \frac{\partial D_{n1}}{\partial x} + D_{\zeta 2} \frac{\partial D_{n1}}{\partial y} + D_{\zeta 3} \frac{\partial D_{n1}}{\partial z}$$

$$c_2 = D_{n1} \frac{\partial D_{\zeta 2}}{\partial x} + D_{n2} \frac{\partial D_{\zeta 2}}{\partial y} + D_{n3} \frac{\partial D_{\zeta 2}}{\partial z} \\ + D_{\zeta 1} \frac{\partial D_{n2}}{\partial x} + D_{\zeta 2} \frac{\partial D_{n2}}{\partial y} + D_{\zeta 3} \frac{\partial D_{n2}}{\partial z}$$

$$c_3 = D_{n1} \frac{\partial D_{\zeta 3}}{\partial x} + D_{n2} \frac{\partial D_{\zeta 3}}{\partial x} + D_{n3} \frac{\partial D_{\zeta 3}}{\partial x} \\ + D_{\zeta 1} \frac{\partial D_{n3}}{\partial x} + D_{\zeta 2} \frac{\partial D_{n3}}{\partial x} + D_{\zeta 3} \frac{\partial D_{n3}}{\partial x}$$

The s are defined as, respectively,

$$\Omega_1 = [D_{n1} D_{n2} D_{n3}] \begin{bmatrix} \frac{\partial U}{\partial x} & \frac{\partial U}{\partial y} & \frac{\partial U}{\partial z} \\ \frac{\partial V}{\partial x} & \frac{\partial V}{\partial y} & \frac{\partial V}{\partial z} \\ \frac{\partial W}{\partial x} & \frac{\partial W}{\partial y} & \frac{\partial W}{\partial z} \end{bmatrix} \begin{bmatrix} D_{n1} \\ D_{n2} \\ D_{n3} \end{bmatrix}$$

$$\Omega_2 = [D_{n1}D_{n2}D_{n3}] \begin{bmatrix} \frac{\partial U}{\partial x} & \frac{\partial U}{\partial y} & \frac{\partial U}{\partial z} \\ \frac{\partial V}{\partial x} & \frac{\partial V}{\partial y} & \frac{\partial V}{\partial z} \\ \frac{\partial W}{\partial x} & \frac{\partial W}{\partial y} & \frac{\partial W}{\partial z} \end{bmatrix} \begin{bmatrix} D_{\eta 1} \\ D_{\eta 2} \\ D_{\eta 3} \end{bmatrix} +$$

$$[D_{\eta 1}D_{\eta 2}D_{\eta 3}] \begin{bmatrix} \frac{\partial U}{\partial x} & \frac{\partial U}{\partial y} & \frac{\partial U}{\partial z} \\ \frac{\partial V}{\partial x} & \frac{\partial V}{\partial y} & \frac{\partial V}{\partial z} \\ \frac{\partial W}{\partial x} & \frac{\partial W}{\partial y} & \frac{\partial W}{\partial z} \end{bmatrix} \begin{bmatrix} D_{n1} \\ D_{n2} \\ D_{n3} \end{bmatrix}$$

$$\Omega_3 = [D_{n1}D_{n2}D_{n3}] \begin{bmatrix} \frac{\partial U}{\partial x} & \frac{\partial U}{\partial y} & \frac{\partial U}{\partial z} \\ \frac{\partial V}{\partial x} & \frac{\partial V}{\partial y} & \frac{\partial V}{\partial z} \\ \frac{\partial W}{\partial x} & \frac{\partial W}{\partial y} & \frac{\partial W}{\partial z} \end{bmatrix} \begin{bmatrix} D_{\zeta 1} \\ D_{\zeta 2} \\ D_{\zeta 3} \end{bmatrix} +$$

$$[D_{\zeta 1}D_{\zeta 2}D_{\zeta 3}] \begin{bmatrix} \frac{\partial U}{\partial x} & \frac{\partial U}{\partial y} & \frac{\partial U}{\partial z} \\ \frac{\partial V}{\partial x} & \frac{\partial V}{\partial y} & \frac{\partial V}{\partial z} \\ \frac{\partial W}{\partial x} & \frac{\partial W}{\partial y} & \frac{\partial W}{\partial z} \end{bmatrix} \begin{bmatrix} D_{n1} \\ D_{n2} \\ D_{n3} \end{bmatrix}$$

The D s are directional cosine/sine or combinations of both between the generalized and Cartesian coordinate systems and equal to:

$$D_{n1} = -\frac{\cos\theta_1 \sin\theta_2}{\alpha}$$

$$D_{n2} = -\frac{\cos\theta_1 \cos\theta_2}{\alpha}$$

$$D_{n3} = -\frac{\sin\theta_1 \cos\theta_2}{\alpha}$$

$$D_{\zeta 1} = -\frac{\cos\theta_2 \sin\theta_2 \sin\theta_1}{\alpha}$$

$$D_{\zeta 2} = \frac{\sin \theta_1 \cos^2 \theta_2}{\alpha}$$

$$D_{\zeta 3} = \frac{\cos \theta_1}{\alpha}$$

$$D_{\eta 1} = \cos \theta_2$$

$$D_{\eta 2} = \sin \theta_2$$

$$D_{\eta 3} = \theta$$

where $\alpha = \sqrt{\cos^2 \theta_1 + \sin^2 \theta_1 + \cos^2 \theta_2}$. θ_1 is the angle measured counterclockwise between the y and z axes and θ_2 is the angle between the y and x axes, also measured counterclockwise. Figure 3.7 pictorially describes the two coordinate systems.

Inspecting Equations (9-14), one can observe the following:

1. They are symmetric except for the surface-tension pressure term in the normal stress relation, Equation (9);
2. They all contain first-order derivatives of the dependent variables, which result from coordinate transformation, and zero-order terms which are present due to the interface curvatures with respect to the Cartesian axes;
3. While there is only one form of σ in each of the Equations (12-14), the value of σ in the liquid side is different from that in the gas side.

The second improvement is the inclusion of surface-tension effects. The surface-tension pressure can be incorporated directly into the momentum equations as extra source terms or included in the interface stress continuity conditions, as was done in Equations (10)-(11). The surface tension pressure S is given by:

$$S = -\sigma K \tag{15}$$

where σ is the surface-tension coefficient and K the surface curvature. To be consistent with the VOF scheme, the surface curvature in a surface cell is given by:

$$K = \frac{d}{dx} \left[\frac{\frac{dY}{dx}}{\sqrt{1 + \left(\frac{dY}{dx}\right)^2}} \right]$$

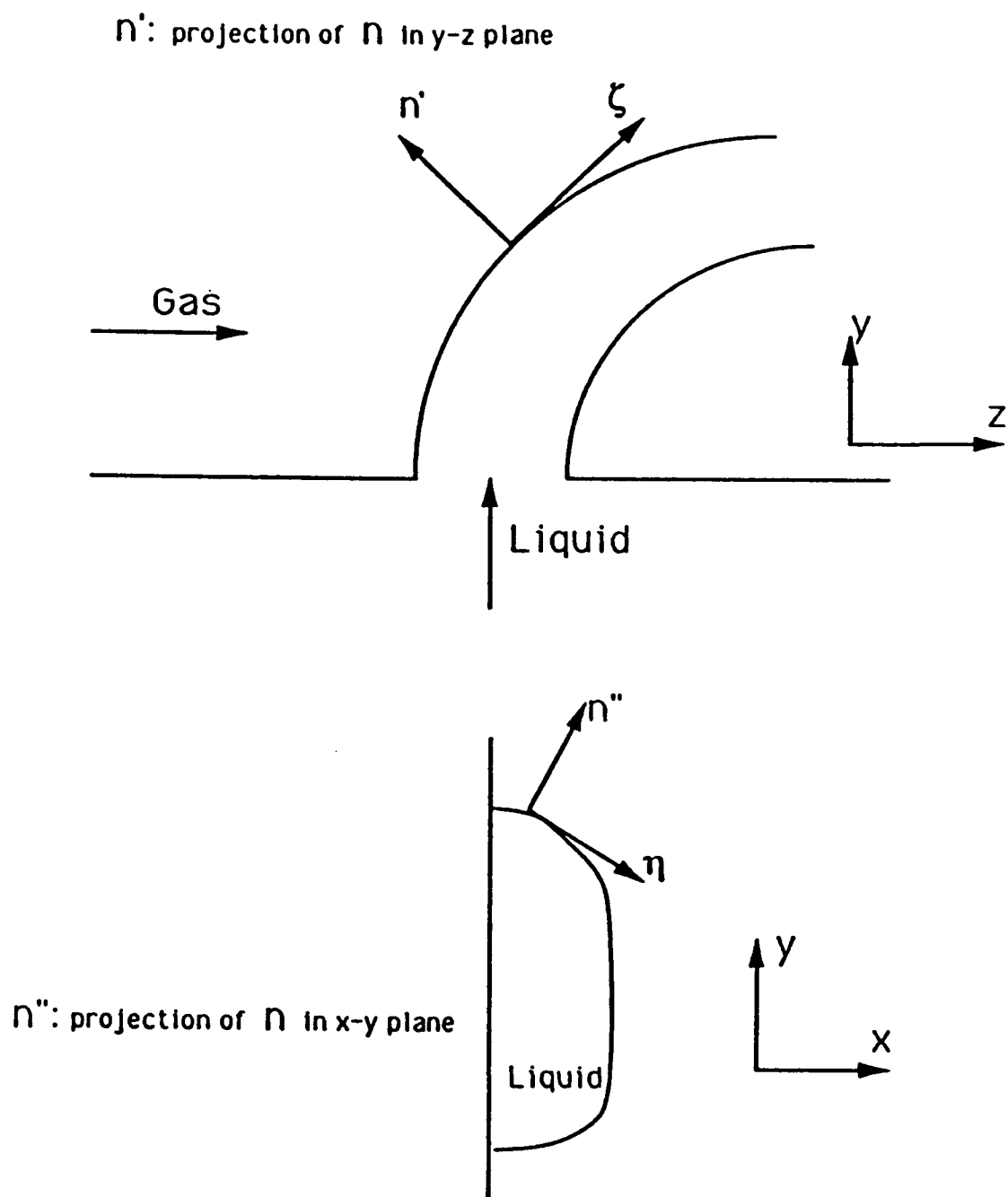


Figure 3.7: The coordinate systems.

when the interface is more horizontal than vertical. Otherwise, the curvature is given by:

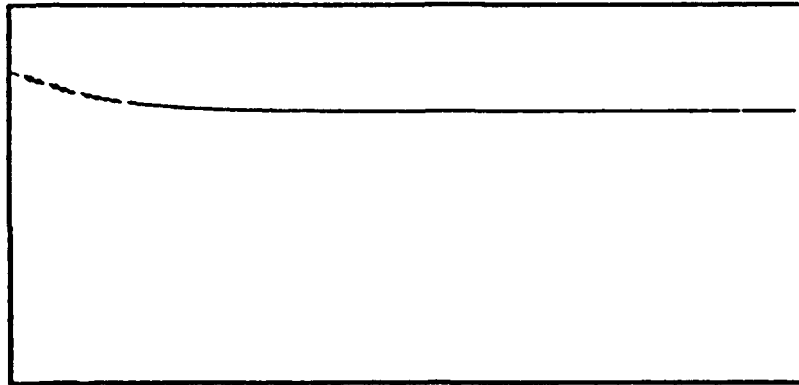
$$K = \frac{d}{dy} \left[\frac{\frac{dX}{dy}}{\sqrt{1 + \left(\frac{dX}{dy}\right)^2}} \right]$$

A second curvature can also be calculated similarly for a three-dimensional flow.

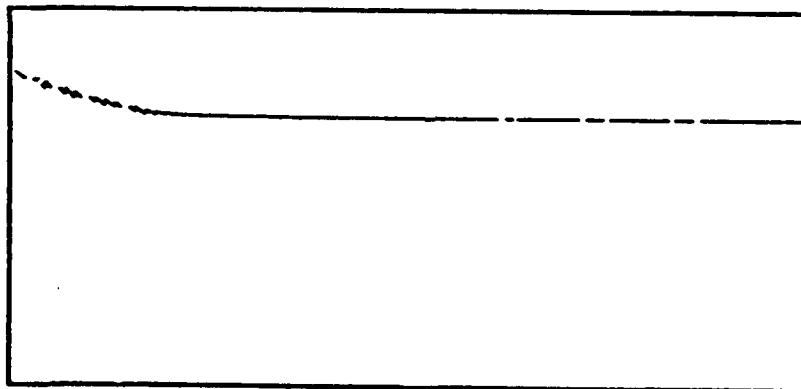
The above interface model is incorporated into the fluid dynamic solver and a two-dimensional free-surface flow is tested to validate the model. The free-surface flow is of a column of liquid with uniform height running into a solid wall. The simulation is to determine the height of the jump and the advancing speed of the bore front as a result. The column of liquid originally moves toward the solid wall at a speed of 0.1 m/s. For simplicity, the flow is kept laminar by choosing a proper combination of fluid density and viscosity; the surface-tension effects are also neglected for the time being. The density of the fluid is immaterial as far as the interface conditions are concerned. In order to discern the effects of viscosity, two parallel numerical simulations are tested, one including viscous effects at the interface and one without. In the figures shown below, the left computational boundary coincides with the solid wall.

Figure 3.8 compares the bore shapes from the two simulations at 0.0015 second after the impact. The height at the solid wall rises, against gravity, to conserve the system mass. The free surface is smoother for the case where viscous effects are included. Figure 3.9 shows the bore shapes at 0.0066 second after the impact. The region influenced by the bore, which is running away from the wall, is clearly broadened. The bore shape is almost completely formed in the case neglecting viscous effects at the free surface. Figure 3.10 shows the two cases at 0.008 second after the impact. The bore shape for the case with viscous effects can now be seen in the plot. Because the formation of the bore front happens later for the viscous case, the elevation in the bore region is mostly higher for the nonviscous case. Figure 3.11 compares the bore shapes at 0.011 second after the impact. The bore is now completely formed for the viscous case. Notice that the elevation of the horizontal bore regions in the two cases is the same. However, the bore front is steeper for the case with no viscous effects at the free surface. Moreover, an undular motion of the bore is also observed, but viscous effects seem to damp out this phenomenon in the other case. Note also that the region influenced by the returning bore is larger for the case including viscous effects.

If the point of half elevation at the bore front is chosen as the reference point, the advancing speed of the viscous bore is 0.4352 m/s while the speed is 0.4754 m/s for the inviscid case. The theoretical speed is 0.4254 m/s [24]. This entails a 2.3% error for the viscous bore, but a 11.8% error for the nonviscous bore. In conjunction with the observation made about the bore elevation in the last paragraph, this suggests that the bore height is primarily an inviscid phenomenon, but that the bore shape and its advancing speed are surely viscous ones.



(a)

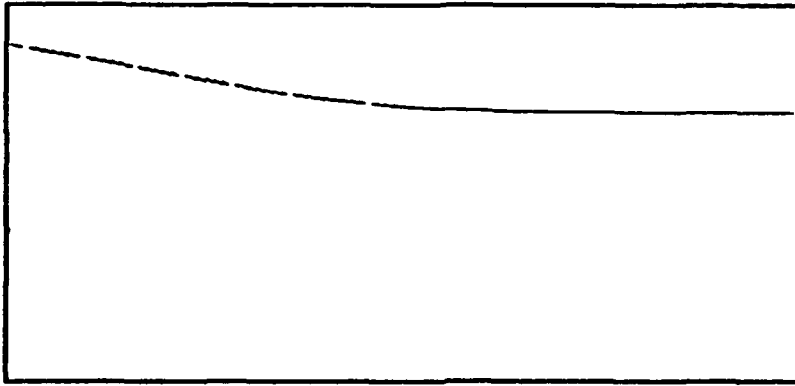


(b)

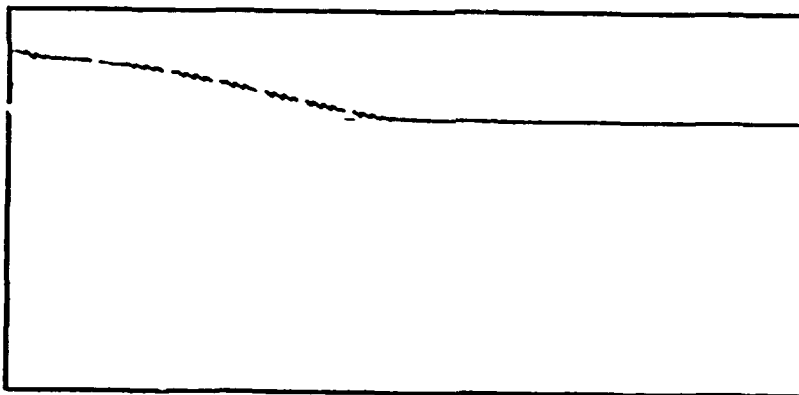
Figure 3.8: Bore Shape

(a): Full interface conditions.

(b): Approximate interface conditions at 0.0015 second.



(a)

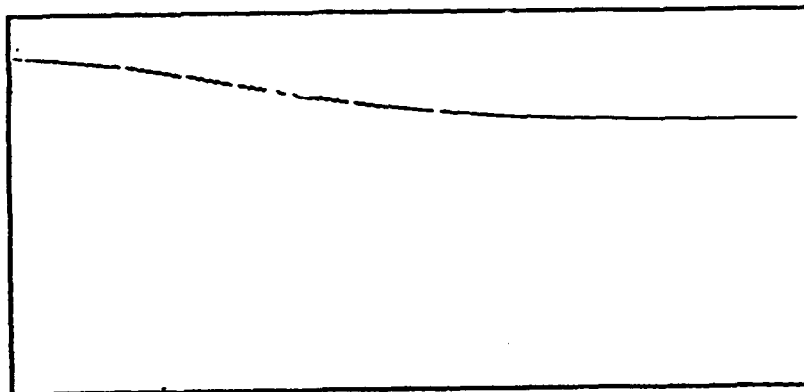


(b)

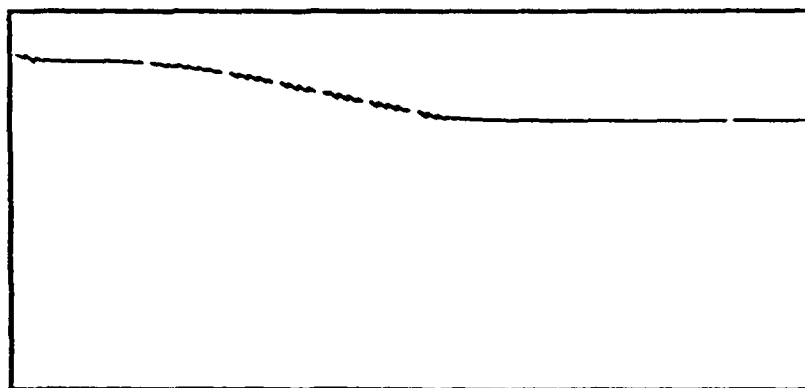
Figure 3.9: Bore Shape

(a): Full interface conditions

(b): Approximate interface conditions at 0.0066 second.



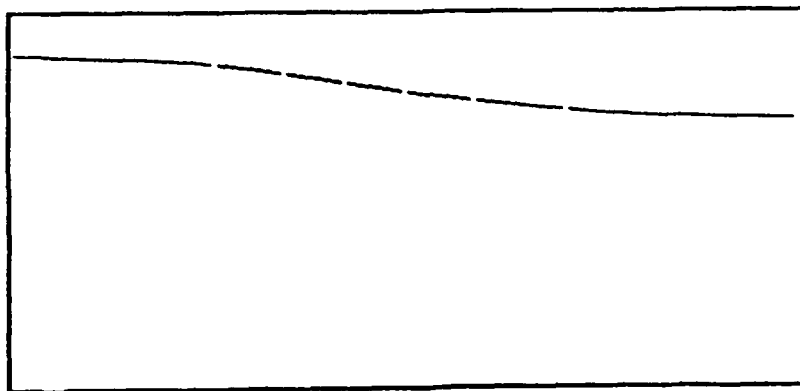
(a)



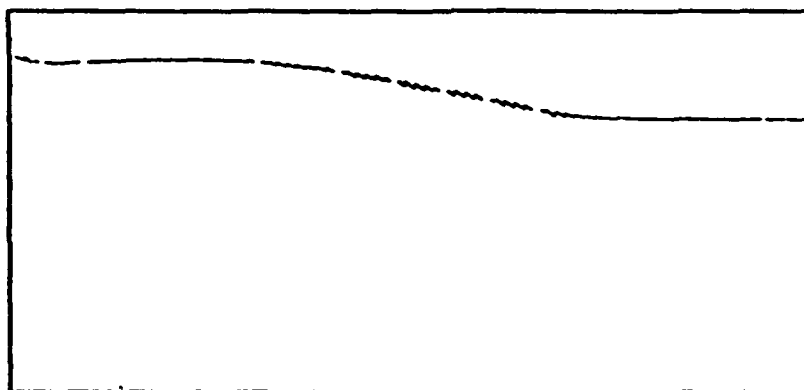
(b)

Figure 3.10: Bore Shape

(a): Full interface conditions.
 (b): Approximate interface conditions at 0.008 second.



(a)



(b)

Figure 3.11: Bore Shape

- (a): Full interface conditions.
- (b): Approximate interface conditions at 0.011 second.

4.0 REFERENCES

- [1] Zukoski, E.E. and Spaid, F.W. "Secondary Injection of Gases into a Supersonic Cross Flow," AIAA Journal, 1964, Vol. 12, p. 1689.
- [2] Schetz, J.A., Weinraub, R.A., and Mahaffey, R.E. "Supersonic Transverse Injection into a Supersonic Stream," AIAA Journal, 1968, Vol. 6, p. 933.
- [3] Schetz, J.A. and Billig, F.S. "Penetration of Gaseous Jets Injected into a Supersonic Stream," Journal of Spacecraft, 1966, Vol. 3, p. 1658.
- [4] Billig, F.S., Orth, R.C., and Lasky, M. "A Unified Analysis of Gaseous Jet Penetration," AIAA Journal, 1971, Vol. 9, p. 1043.
- [5] McDaniel, J.C. and Graves, J. "Laser-Induced Fluorescence Visualization of Transverse Gaseous Injection in a Nonreacting Supersonic Combustor," Journal of Propulsion and Power, 1988, Vol. 4, p. 591.
- [6] Heister, S.D. and Karagozian, A.R. "Gaseous Jet in Supersonic Crossflow," AJAA Journal, 1990, Vol. 28, p. 819.
- [7] Broadwell J.E. and Breidenthal, R.E. "Structure and Mixing of a Transverse Jet in Incompressible Flow," Journal of Fluid Mechanics, 1984, Vol. 148, p. 405.
- [8] Pratte, B.D. and Baines, W.D. "Profiles of Round Turbulent Jet in a Cross Flow," Journal Hydronaut. Div. ASCE, 1967, Vol. 92, p.53.
- [9] Crans, L.J. and Collins, D.J. "Stagnation Temperature and Molecular Weight Effects in Jet Penetrations," AIAA Journal, 1970, Vol. 8, p. 287.
- [10] Shapiro, A.H. "The Dynamics and Thermodynamics of Compressible Fluid Flow," Vol. II, Krieger, 1954, p. 883.
- [11] Bergeles, G., Gosman, A.D. and Launder, B.E. "Double-Row Discrete-Hole Cooling: An Experimental and Numerical Study," AIAA Journal, 1977, Vol. 15, p. 499.
- [12] Karagozian, A.R. "The Flame Structure and Vorticity Generated by a Chemically Reacting Transverse Jet," AIAA Journal, Vol. 24, No. 9, pp. 1502, 1986.
- [13] Karagozian, A. R. "An Analytical Model for the Vorticity Associated with a Transverse Jet," AIAA Journal, Vol. 24, No. 3, pp. 429, 1986.
- [14] Fearn, R. and Weston, R. P. "Vorticity Associated with a Jet in a Cross Flow," AIAA Journal, Vol. 12, No. 12, pp. 1666, 1974.
- [15] Krothapalli, A., Lourenco, L., and Buchlin, J.M. "On the Separated Flow Upstream of a Jet in a Cross Flow," AIAA 27th Aerospace Sciences Meeting, Reno, Nevada, 1989.
- [16] Heister, S.D., Nguyen, T.T., and Karagozian, A.R. "Modeling of Liquid Jets Injected Transversely into a Supersonic Crossflow," AIAA 26th Aerospace Sciences Meeting, Reno, Nevada, January 11-14, 1988 .

- [17] Adelberg, M. "Breakup Rate and Penetration of a Liquid Jet in a Gas Stream," AIAA Journal, Vol. 5, No. 8, p. 1408, 1967.
- [18] Broadwell, J.E. and Breidenthal, P.E. "Structure and Mixing of a Transverse Jet in Incompressible Flow," Journal of Fluid Mechanics, Vol. 148, pp. 405, 1984.
- [19] Kamotani, Y. and Greber, I. "Experiments on a Turbulent Jet in a Cross Flow," AIAA Journal, Vol. 10, p. 1425, 1972.
- [20] Less, D.M. and Schetz, J.A. "Transient Behavior of Liquid Jets Injected Normal to a High-Velocity Gas Stream," AIAA Journal, Vol. 24, No. 12, p. 1979, 1986.
- [21] Patankar, S.V., "Numerical Heat Transfer and Fluid Flow," McGraw-Hill Book Company, 1981.
- [22] Ramshaw, J.D. and Trapp, J.A. "A Numerical Technique for Low-Speed Homogeneous Two-Phase Flow with Sharp Interfaces," Journal of Computational Physics, Vol. 21, p. 438, 1976.
- [23] Hirt, C.W. and Nichols, B.D. "Volume of Fluid (VOF) Method for the Dynamics of Free Boundaries," Journal of Computational Physics, Vol. 39, p. 201, 1981.
- [24] Stoker J.J., "Water Waves," Interscience, New York, 1975.
- [25] Van Dyke, M. "Entry Flow in a Channel," Journal of Fluid Mechanics, Vol. 44, Part 4, p. 813, 1970.

APPENDIX A

Estimation of Average Pressure around Jet

To find the circumferentially-averaged pressure around the jet, the jet is treated as a circular inviscid cylinder in a cross flow. The sketch of Figure 2.2 shows the flow features as we proceed along the cylinder surface from the front to the rear stagnation points: the sonic point is reached at the approximate radial location where a straight line tangent to the cylinder makes an angle δ_{\max} (the maximum shock-turning angle) with respect to the centerline [10]. Flow accelerates through a Prandtl-Meyer expansion until it passes through a shock which is necessary to decelerate it to the rear stagnation point. The circumferentially-averaged pressure is:

$$\bar{p} = \frac{1}{\pi} \int_0^{\pi} p d\phi$$

with ϕ defined in Figure 2.2.

Since the cylinder perimeter represents a streamline, the total pressure after the main shock, p_{t2} , is preserved from the front stagnation point to the rear shock. If the rear-shock position were known, the entire pressure distribution around the cylinder would be readily obtainable by the approximations:

From front stagnation point to sonic point:

$p \approx 1/2(p_{t2} + p_*)$, where p_* is the static pressure at the sonic point.

From sonic point to rear shock:

p given by Prandtl-Meyer relations with p_{t2} , the total pressure.

From rear shock to rear stagnation point:

$p \approx p_{t3}$, with p_{t3} the total pressure after the rear shock.

The difficulty lies in predicting the rear-shock location, which requires a numerical solution of the flow field. To circumvent the problem, the present method uses an empirical input to locate the rear shock. That input is the drag coefficient C_D for the inviscid cylinder in supersonic flow, which can be inferred from experimental data and numerical computations. The values for C_D used here are the average of those suggested by Schetz and Billig [3] ($C_D = 1.06 + 1.14M_1^{-3}$) and by Heister and Karagozian [6] ($C_D = 1.2 + 0.543M_1^{-2}$), which are in good agreement for $M_1 > 2$. In terms of p , the drag coefficient is

$$C_D = \frac{2}{\gamma_1 p_1 M_1^2} \int_0^{\pi} p \sin\phi d\phi$$

The radial location of the rear shock was computed by trial and error so that C_D given by the above formula agreed with the empirical expressions. The resulting average pressure, expressed as \bar{p}/p_2 , ranged from 0.55 for $M_1 = .5$ to 0.42 for $M_1 = 4.0$. Hence, the value $\bar{p} = 0.5p_2$ appears to be a fair approximation for the range of Mach numbers explored here.

APPENDIX B

Phase I. Simple Channel Flow

To facilitate the test, three sides of the channel are taken to be planes of symmetry; i.e., flow fields on the other sides of these three planes are simply mirror images of the flow field in the channel considered. A uniform inlet velocity of 1 m/s is used and the fluid viscosity coefficient and density are chosen such that the Reynolds number based on the half channel height equals 50. Three tests are completed for flows having different axes of development, but results from only one test are presented here. The flow is developing along the positive z direction and bounded by a wall at $y=1$ m. The bottom plane as well as planes at $x=0$ and $x=1$ m are taken as a plane of symmetry in the problem. The channel is 16 meters long (z) and 1 meter wide (x) in the simulation. The boundary conditions are:

$$\bar{\omega} = 0. \quad @ y = 1 \text{ m}$$

$$\frac{\partial \bar{\omega}}{\partial x} = 0. \quad @ z = 16 \text{ m}$$

$$\left\{ \begin{array}{l} U = 0. \\ \frac{\partial V}{\partial x} = 0. \\ \frac{\partial W}{\partial x} = 0. \end{array} \quad @ x = 1 \text{ m} \right\}$$

$$\left\{ \begin{array}{l} V = 0. \\ \frac{\partial U}{\partial y} = 0. \\ \frac{\partial W}{\partial y} = 0. \end{array} \quad @ y = 0 \right\}$$

$$\left\{ \begin{array}{l} U = 0. \\ V = 0. \\ W = 1.0 \text{ m/s} \end{array} \quad @ z = 0 \right\}$$

$$\left\{ \begin{array}{l} U = 0. \\ \frac{\partial V}{\partial x} = 0. \\ \frac{\partial W}{\partial x} = 0 \end{array} \quad @ x = 0 \right\}$$

The iterative solution process is terminated when the overall mass-flux imbalance is less than 0.001% of the inlet mass flux.

A direct numerical comparison of the z-component velocity profile at the exit ($z=16$ m) between the numerical solution and the exact solution below demonstrates favorably the performance of the code.

Y	EXA. SOL.	NUM. SOL.	ERROR (%)
8.0E-02	1.4904E+00	1.4880E+00	1.6432E-01
1.6E-01	1.4616E+00	1.4599E+00	1.1897E-01
2.4E-01	1.4136E+00	1.4129E+00	4.8102E-02
3.2E-01	1.3464E+00	1.3470E+00	4.1516E-02
4.0E-01	1.2600E+00	1.2618E+00	1.4207E-01
4.8E-01	1.1544E+00	1.1572E+00	2.4583E-01
5.4E-01	1.0626E+00	1.0660E+00	3.2100E-01
6.0E-01	9.6000E-01	9.6376E-01	3.9158E-01
6.6E-01	8.4660E-01	8.5046E-01	4.5653E-01
7.2E-01	7.2240E-01	7.2613E-01	5.1564E-01
7.6E-01	6.3360E-01	6.3710E-01	5.5239E-01
8.0E-01	5.4000E-01	5.4317E-01	5.8715E-01
8.4E-01	4.4160E-01	4.4434E-01	6.2139E-01
8.6E-01	3.9060E-01	3.9310E-01	6.3904E-01
8.8E-01	3.3840E-01	3.4062E-01	6.5724E-01
9.0E-01	2.8500E-01	2.8693E-01	6.7695E-01
9.2E-01	2.3040E-01	2.3201E-01	7.0028E-01
9.4E-01	1.7460E-01	1.7588E-01	7.3162E-01
9.5E-01	1.4625E-01	1.4735E-01	7.5347E-01
9.6E-01	1.1760E-01	1.1852E-01	7.8357E-01
9.7E-01	8.8650E-02	8.9386E-02	8.3021E-01
9.8E-01	5.9400E-02	5.9946E-02	9.1915E-01
9.9E-01	2.9850E-02	3.0201E-02	1.1771E+00

Figure B.1 shows the development of the centerline z-component velocity. An interesting feature is that, instead of asymptotically approaching the fully-developed velocity value of 1.5 m/s straightforwardly, an inflection point is present in the profile at the beginning stage of the development. This signifies the time lag for the fluids at the bottom to feel the presence of the wall completely. This is also consistent with the finding by Van Dyke [25].

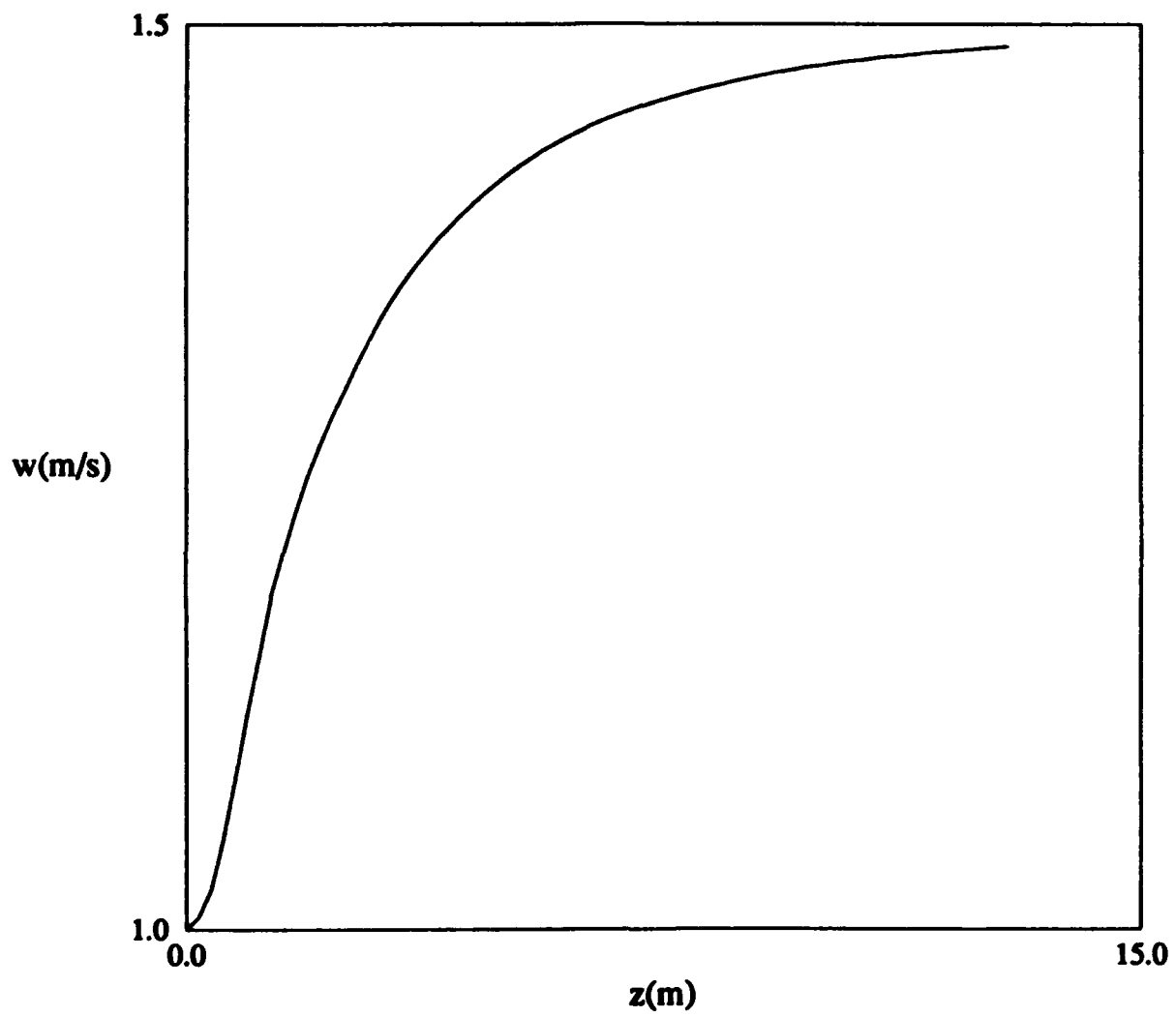


Figure B.1: Centerline velocity development.

APPENDIX C

Phase II. Gaseous Jet Injection

Figure C.1 shows the velocity field in a x-y cross-section at $z=0.00934$ m. The stronger jet in this case creates two different features from those of the previous runs. First, a slender, recirculating region very close to the plane of symmetry at $x=0$ is present. The inner part (near $x=0$) of the jet is able to penetrate much farther into the cross-flow than the outer part is. Strong enough shear is thus generated between fluid elements and the recirculating region is created. Second, the stronger and heavier jet pushes the surrounding gas near the bottom out almost to the core region of the cross-flow. This effect counters the mixing between the injectant and the cross-flow. Figure C.2 presents the mass fraction contours at the same location. The dip at the top portion of the contours reflects the existence of the aforementioned recirculating region. The injectant is able to penetrate far better than those in the previous two cases. Figures C.3 and C.4 are the same pair of plots about 1.3 diameters down stream from the end of the injection. The recirculating mass encompasses a much larger portion of the computational domain compared with those in the previous two runs. The upward current, as is indicated by Figure C.4, at the bottom near $x=0$ seems to be stronger also. It becomes clear later that a rotating vortex in z-y plane contributes to this phenomenon.

Figure C.5 shows the velocity field at a location approximately 20 diameters downstream from the end of injection. The flow field at this location is very complicated, even though the maximum speed is only about half of what it was at the previous locations shown. Careful examination reveals that there are a total of five recirculating regions in this cross section. The center of the dominating rotating vortex moves both upward and toward the center. This latter movement was not seen in the two runs described before. A slender recirculating region is created again at the center (in y dimension) near $x=0$, only this time it possesses the opposite sense from the one described in Figure C.1. Figure C.6 is the companion mass fraction distribution plot of Figure C.5. The injectant in this case reached the top plane of symmetry. This has a very distinctive implication for the geometry we have chosen. The plane of symmetry at the top ($y=0.04$ m) implies that the full channel actually comprises the present computational domain plus its mirror image, which has an injection configuration opposite to the present one. There would be two distinct flames if combustion occurs in the previous two runs; then, Figure C.6 indicates that the two flames might join at a certain downstream location.

Figure C.7 is a vectorial representation of the velocity field in a z-y cross-section at $x=0.00035$ m. The wake region behind the injection is stronger and extends from the bottom to a higher position in y dimension than those in the previous cases. In addition to what has been observed in the lower momentum flux ratio runs before, a clockwise-rotating vortex is present near the bottom of this cross section. This vortex is created by the upward momentum of the jet and the fact that permeability of a dense jet is poorer for the cross-flow in the streamwise direction. Figure C.8 is the mass fraction contours plot at the same spanwise location. Significant mixing does not occur until about half way across the height of the chamber; and there it is almost as if the injectant is forced to make a ninety degree turn towards the direction of the cross-flow. Figures C.9 and C.10 present the velocity and mass fraction fields at $x=0.00362$ m, about 1.3 diameters away from the end of the injection in the spanwise direction. The existence of the recirculating region mentioned previously signifies that the high momentum influx brought by the jet is still felt at this location. Apart from this, the rest of the flow field is similar to those of the lower momentum flux ratio cases. Figure C.12 indicates that the convective mass transport is not as dominant at this location as it was in the previous two cases.

Figures C.11 and C.12 are plots of velocity vectors and mass fraction contours in a z-x cross-section at a height of 0.00029 m. One can find a recirculating wake immediately behind the jet (represented by an almost stagnant region near $x=0$) and a second recirculatory region further away from the jet at the center in the spanwise direction. The second feature was not present in the lower momentum flux ratio cases. Figures C.13 and C.14 are the same pair of plots at $y=0.02066$ m. This is about 10 diameters above the injection orifice. Unlike its counterparts before, the injection is felt by the cross-flow at such a high position that the cross-flow still has to adjust its passage near $x=0$. The bulk of the injectant is still around a region that is a direct projection of the injection orifice onto this cross-section, as is indicated by Figure C.14.

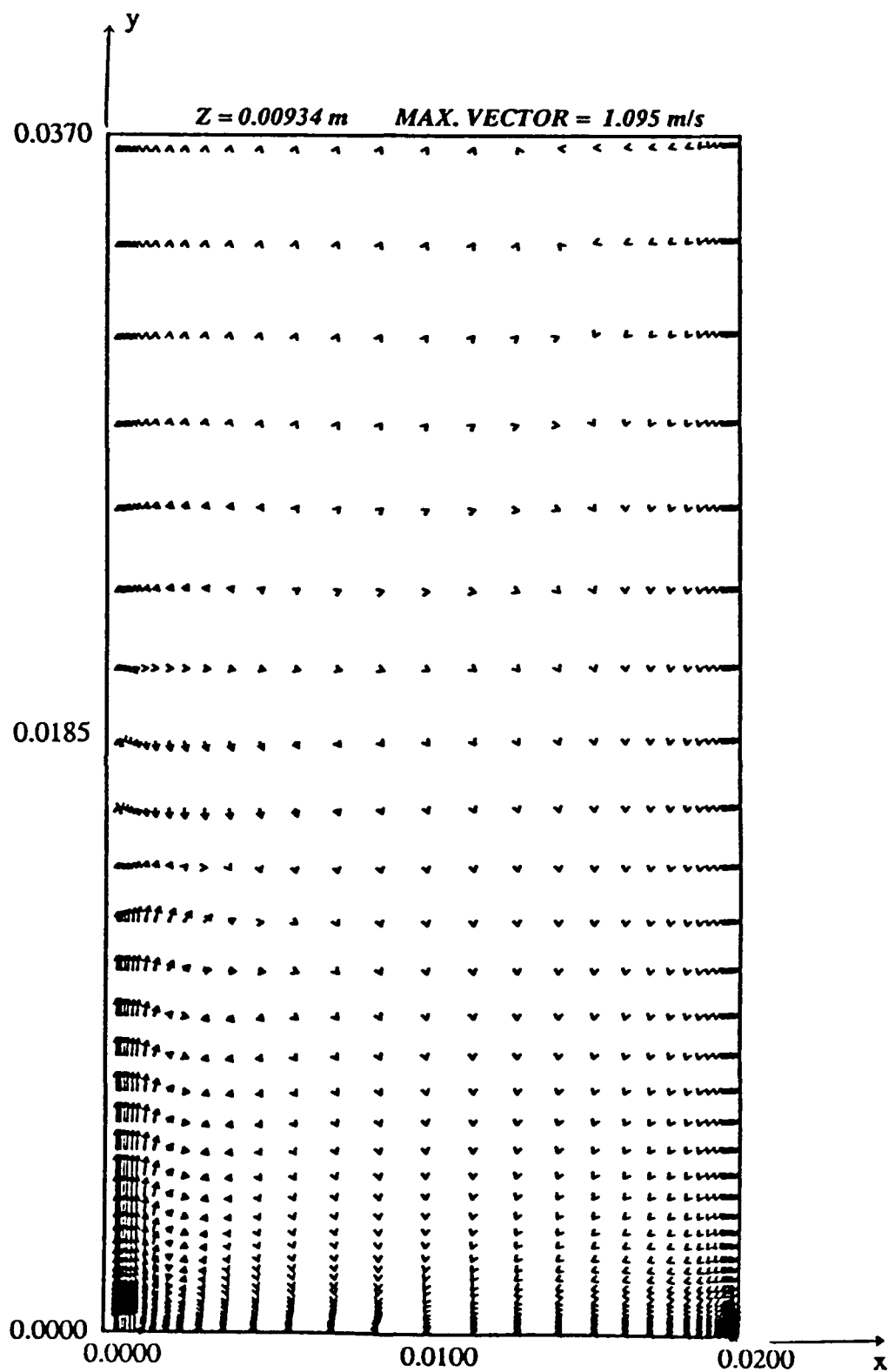


Figure C.1: Velocity vectors (x-y) at $z=0.00934 \text{ m}$.

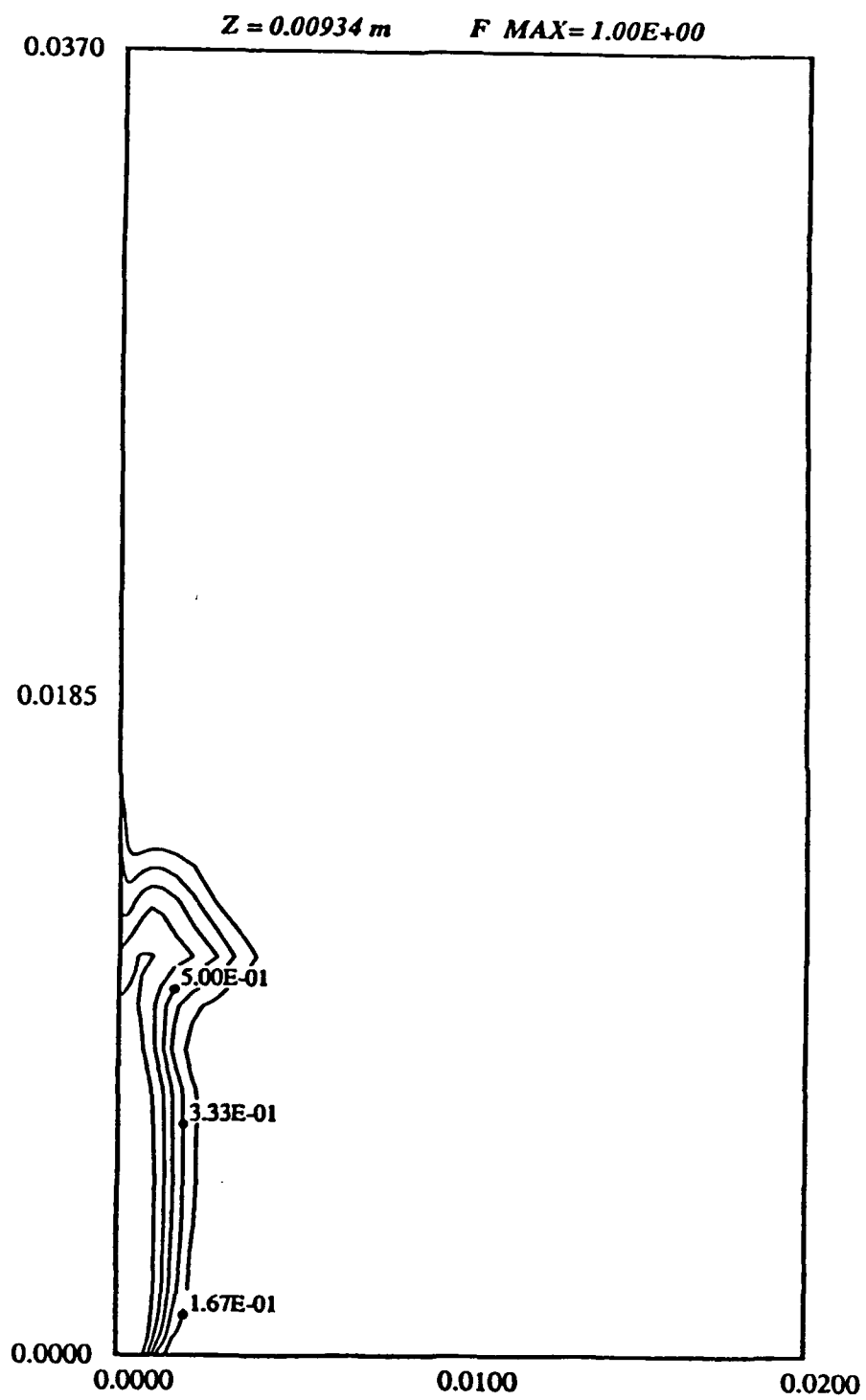


Figure C.2: Mass fraction contours of injectant (x-y) at $z=0.00934 \text{ m}$.

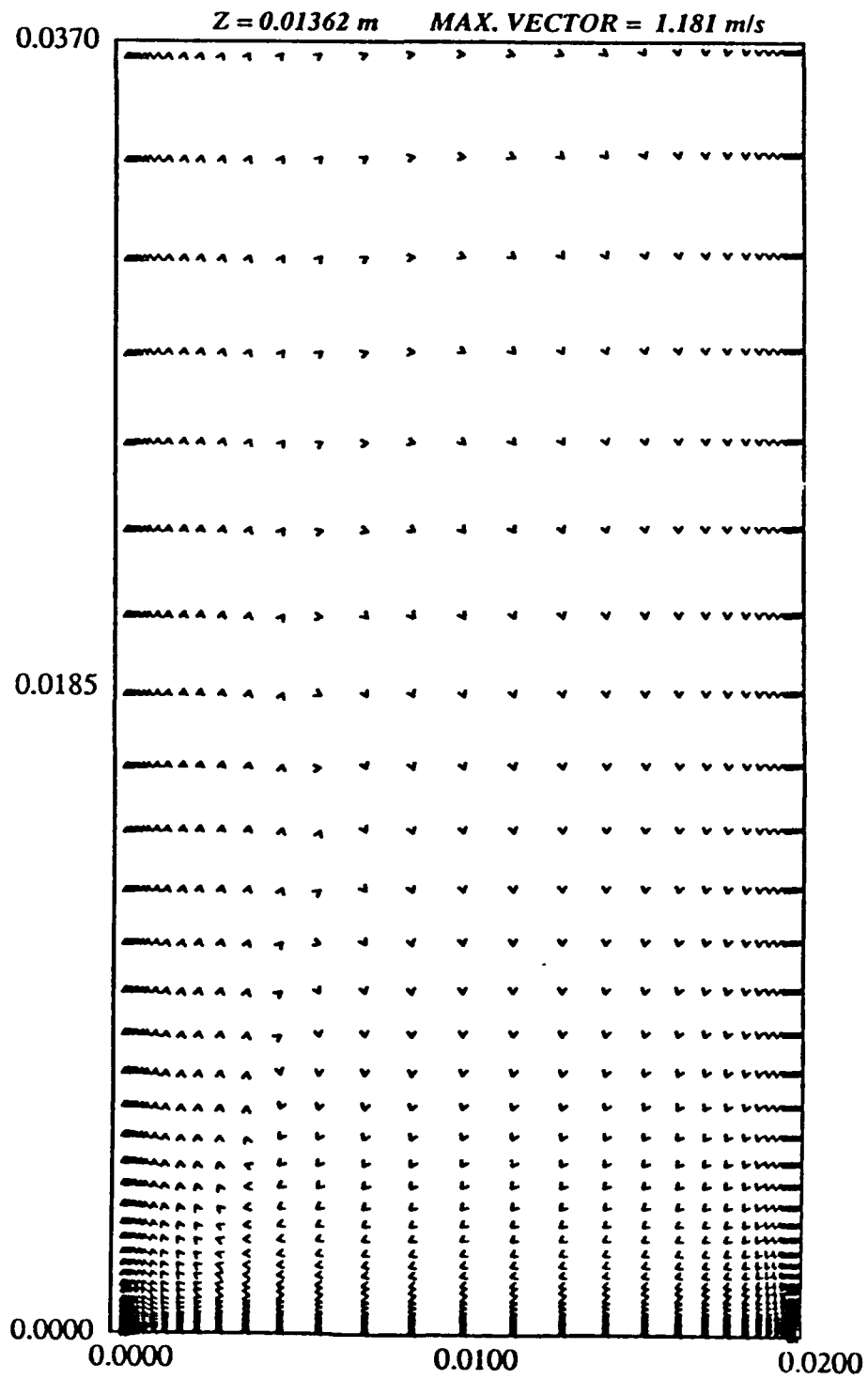


Figure C.3: Velocity vectors (x-y) at $z=0.01362 \text{ m}$.

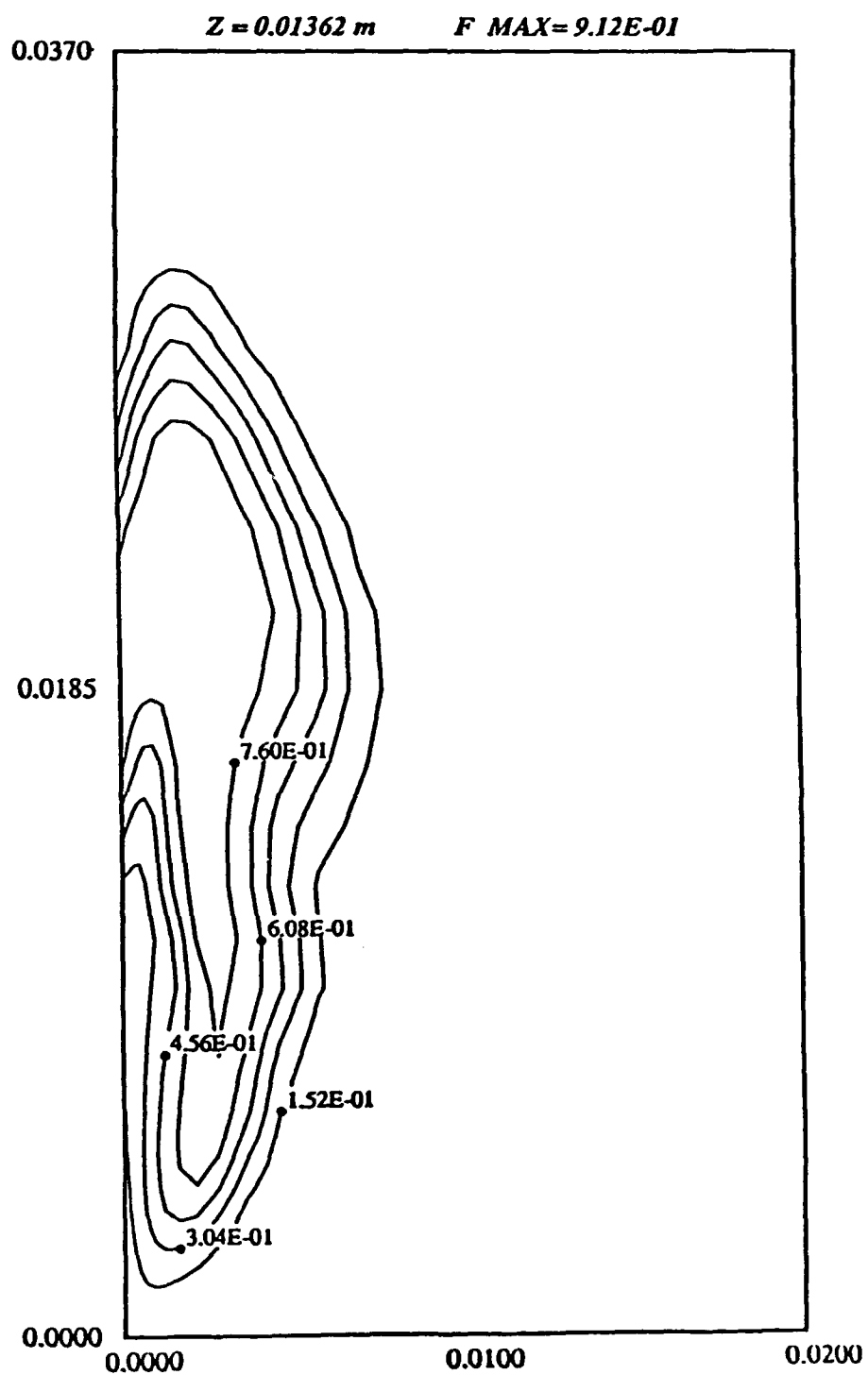


Figure C.4: Mass fraction contours of injectant (x-y) at $z=0.01362 \text{ m}$.

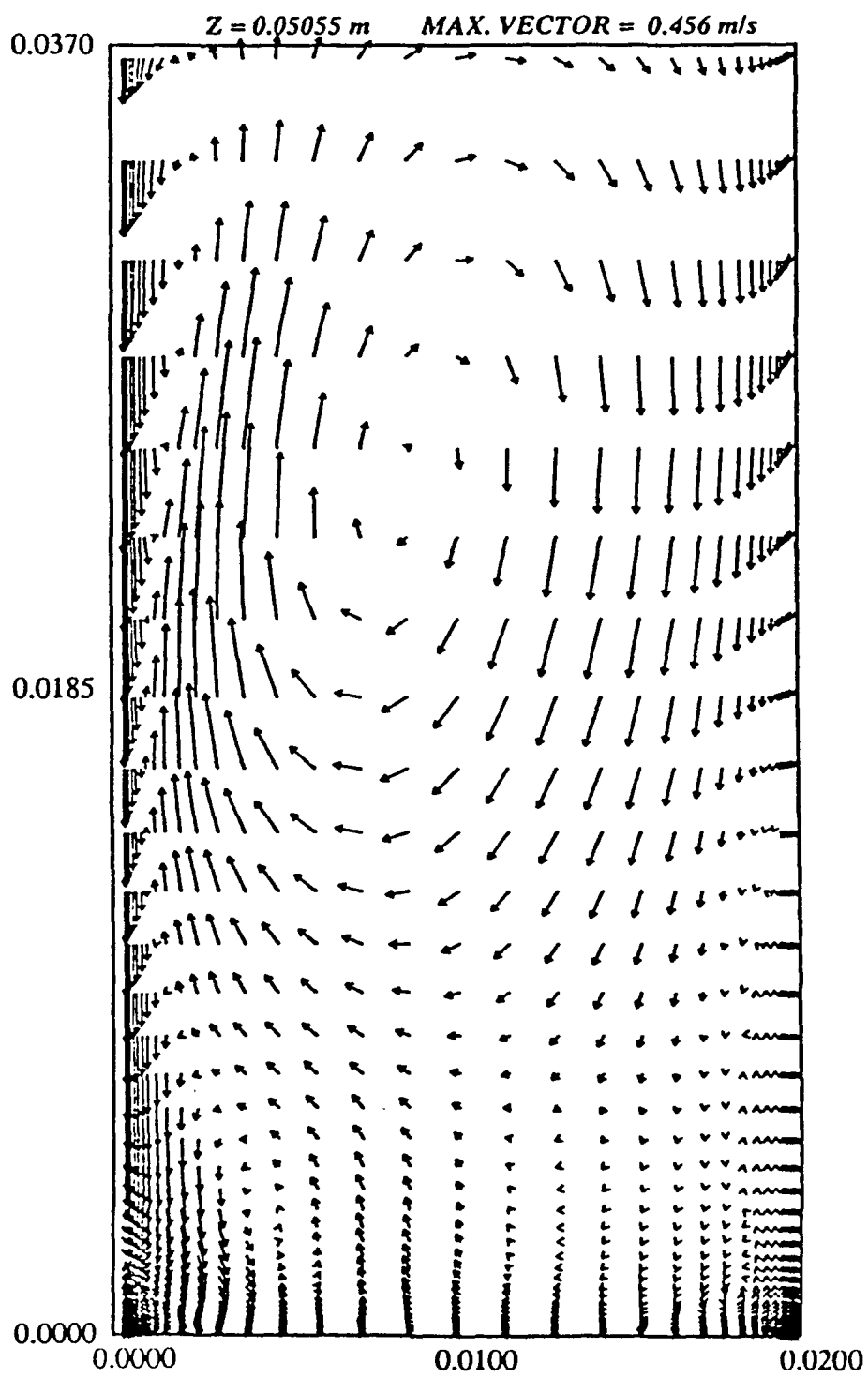


Figure C.5: Velocity vectors (x-y) at $z=0.05055 \text{ m}$.

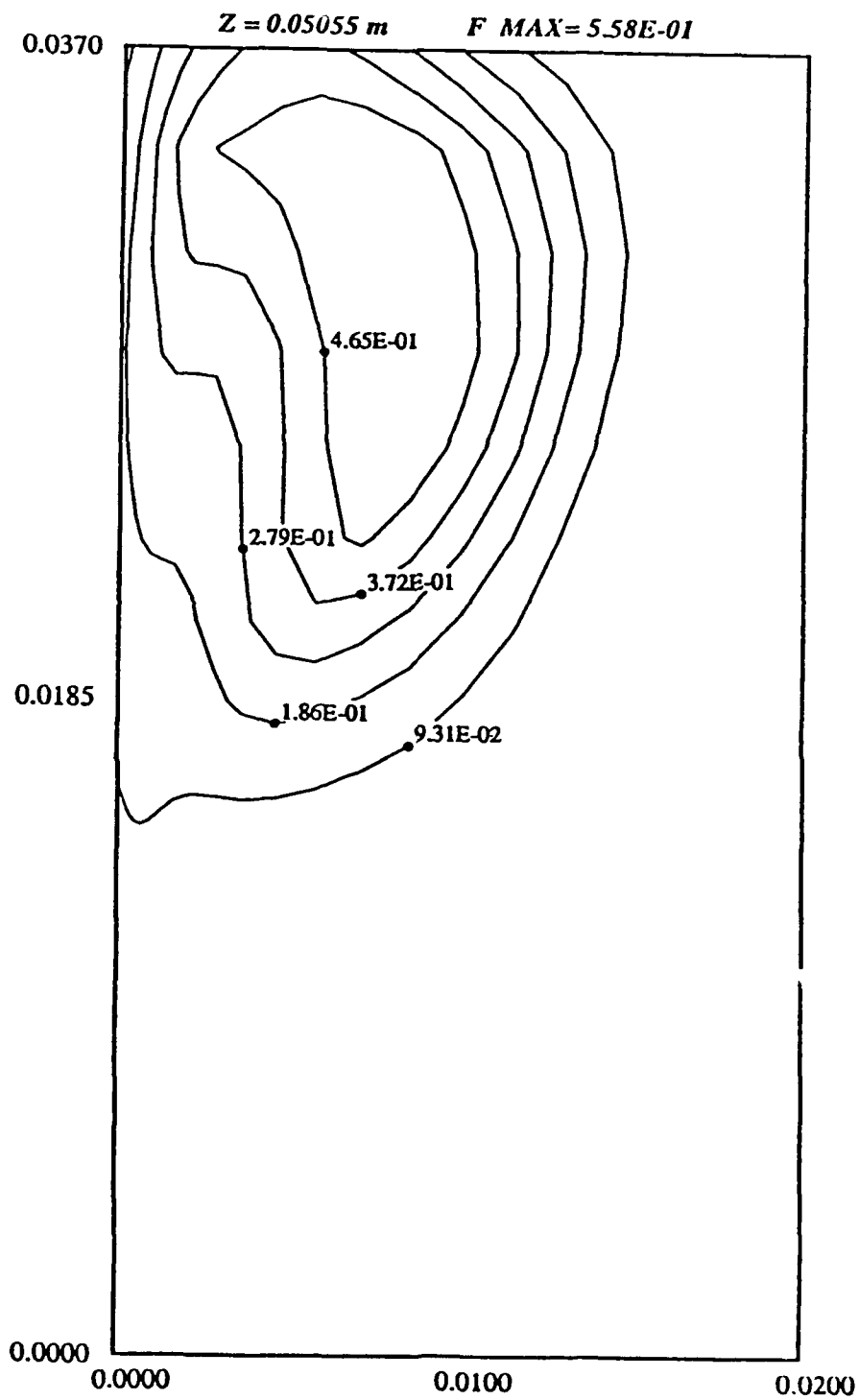


Figure C.6: Mass fraction contours of injectant (x-y) at $z=0.05055 \text{ m}$.

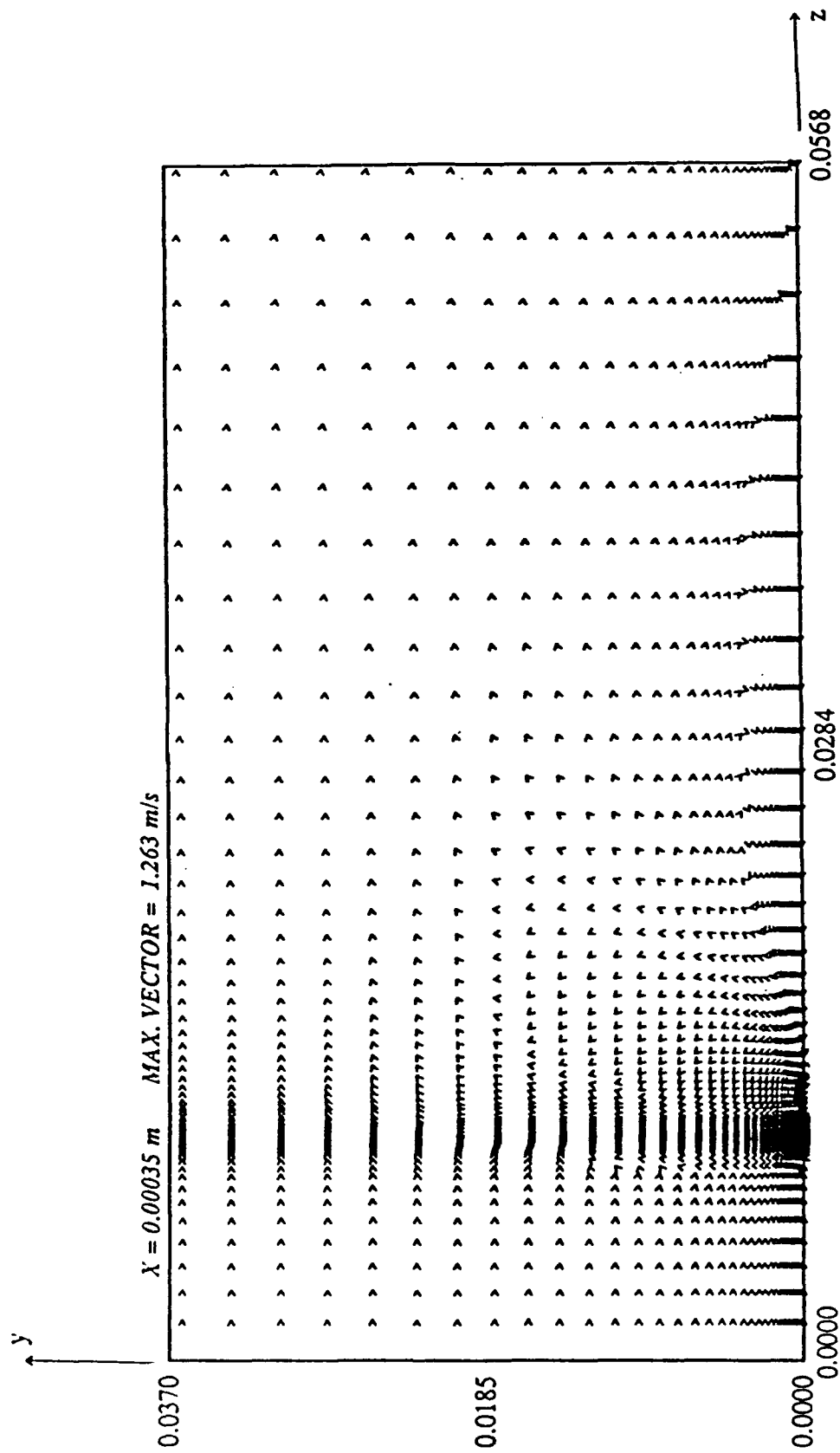


Figure C.7: Velocity vectors (z-y) at $x=0.00035 \text{ m}$.

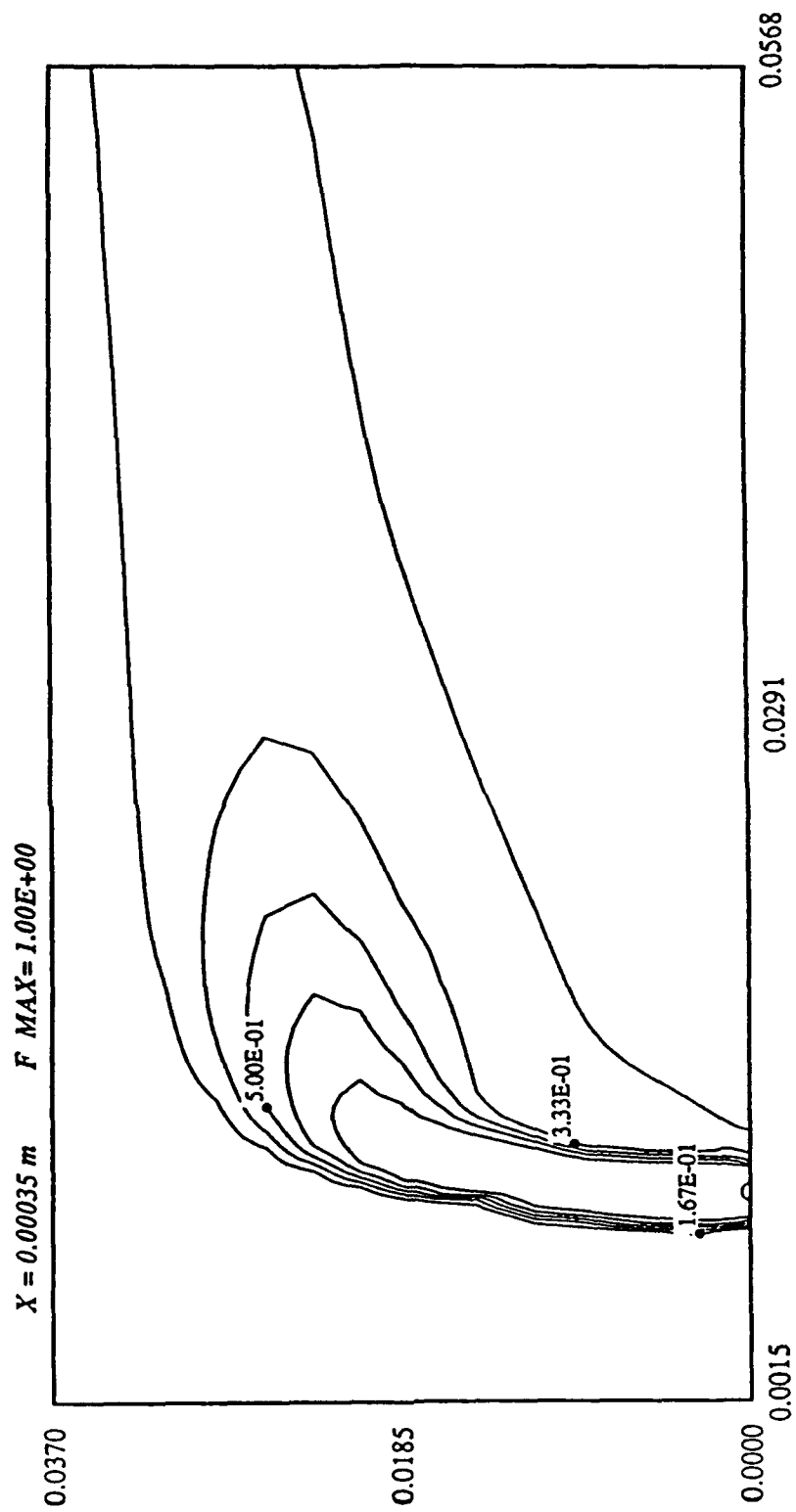


Figure C.8: Mass fraction contours of injectant ($z-y$) at $x=0.00035 \text{ m}$.

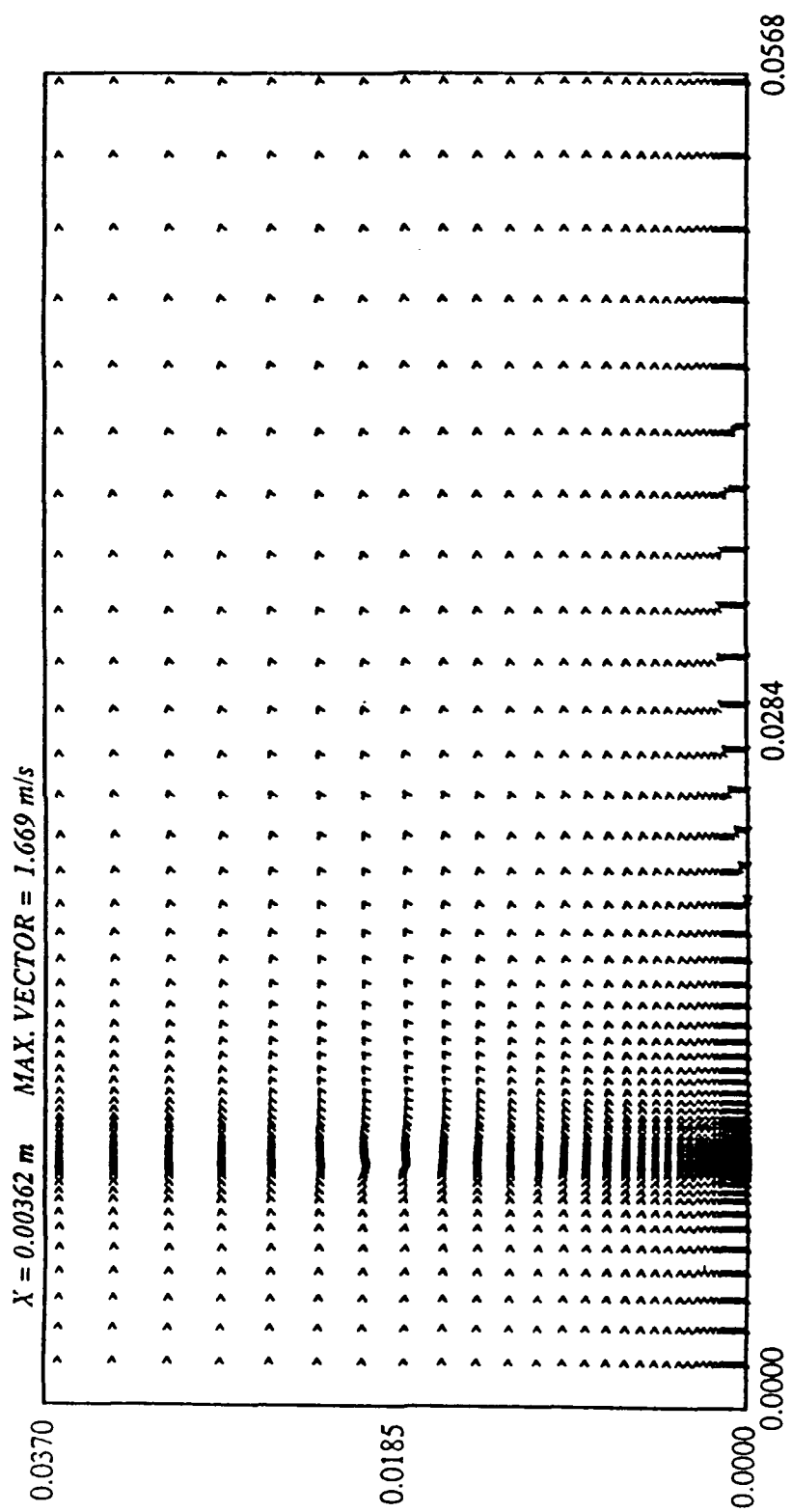


Figure C.9: Velocity vectors (z-y) at $x=0.00362 \text{ m}$.

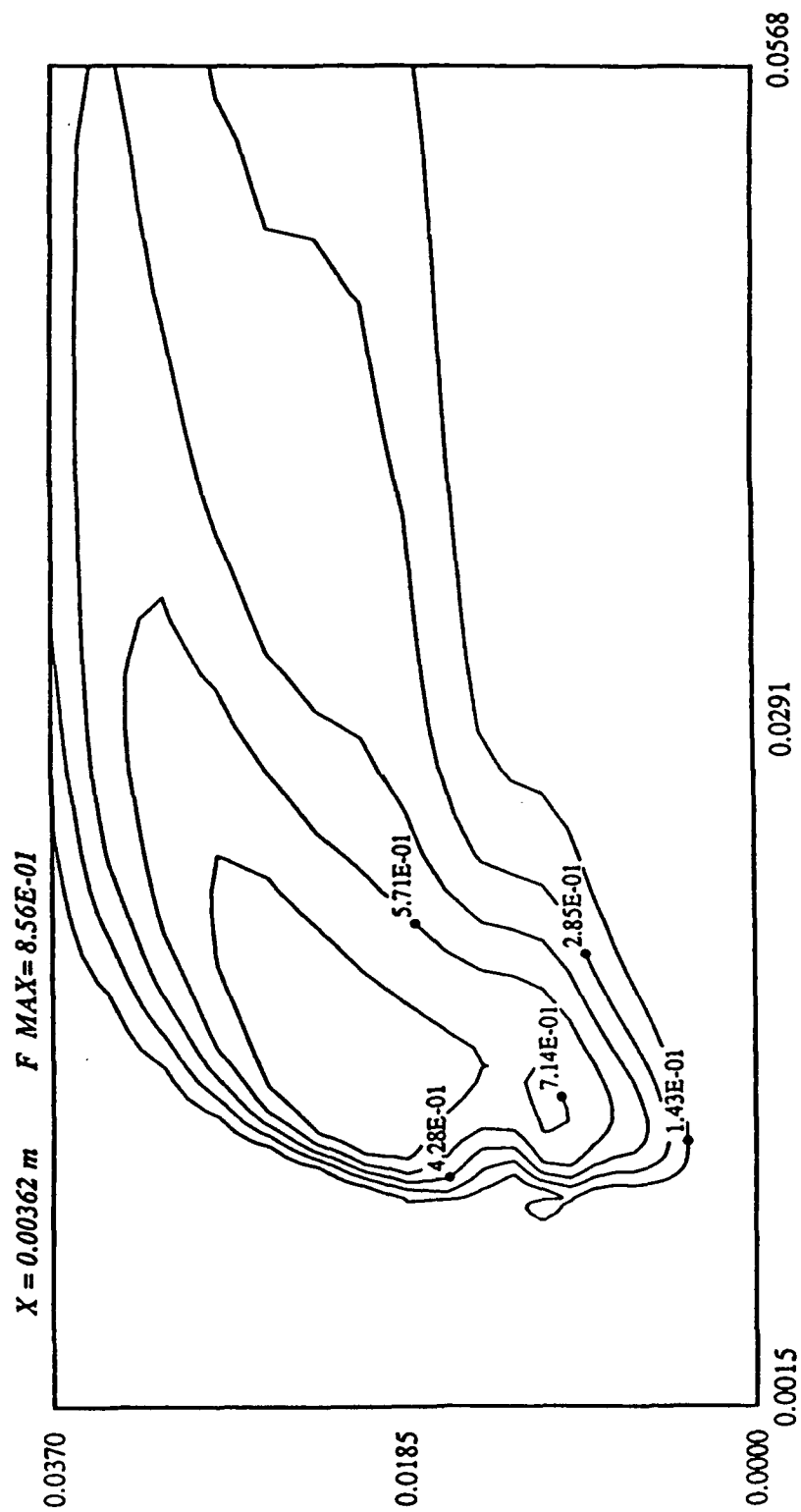


Figure C.10: Mass fraction contours of injectant (z-y) at $x=0.00362 \text{ m}$.

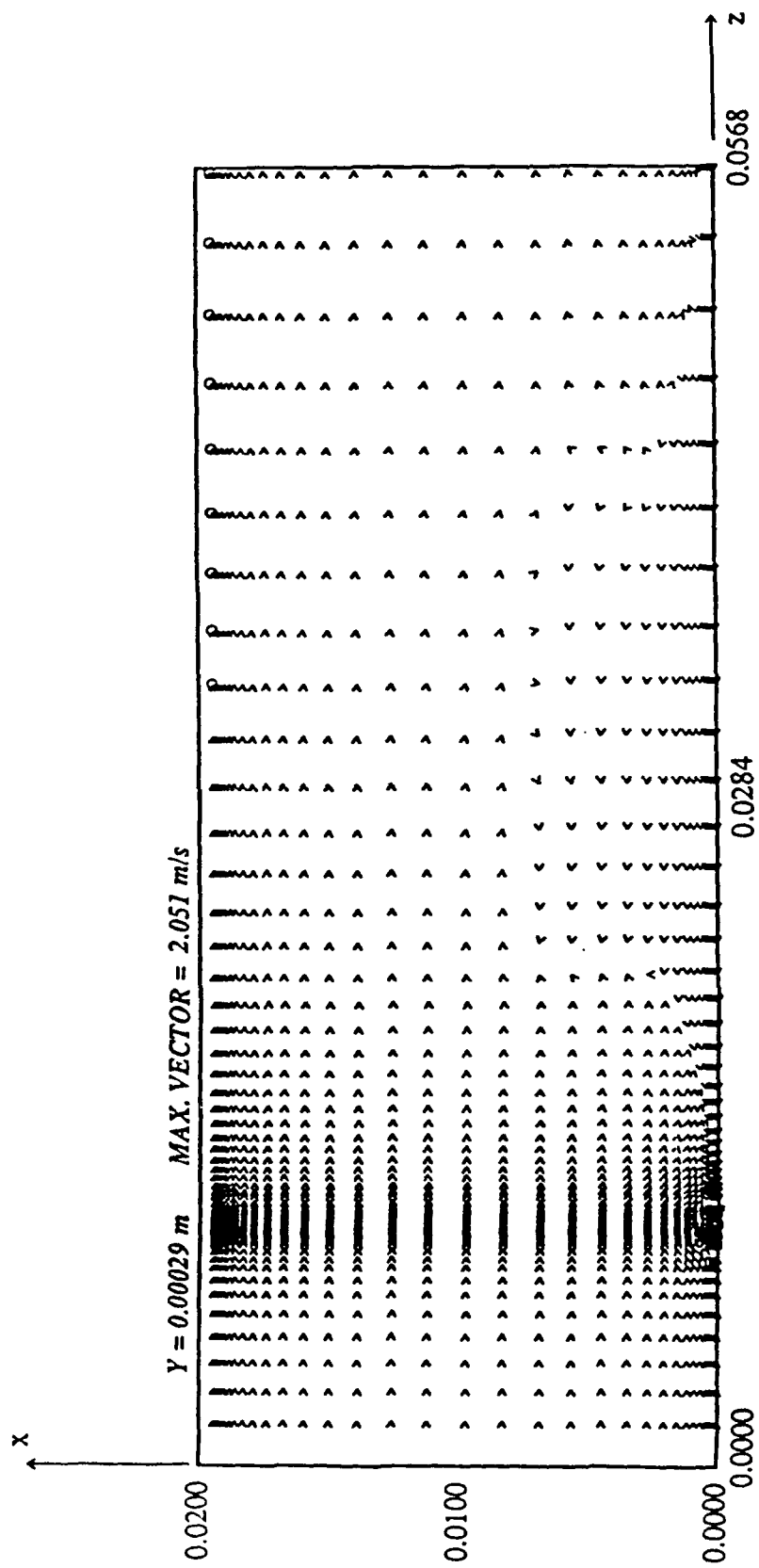


Figure C.11: Velocity vectors (z-x) at $y=0.00029$ m.

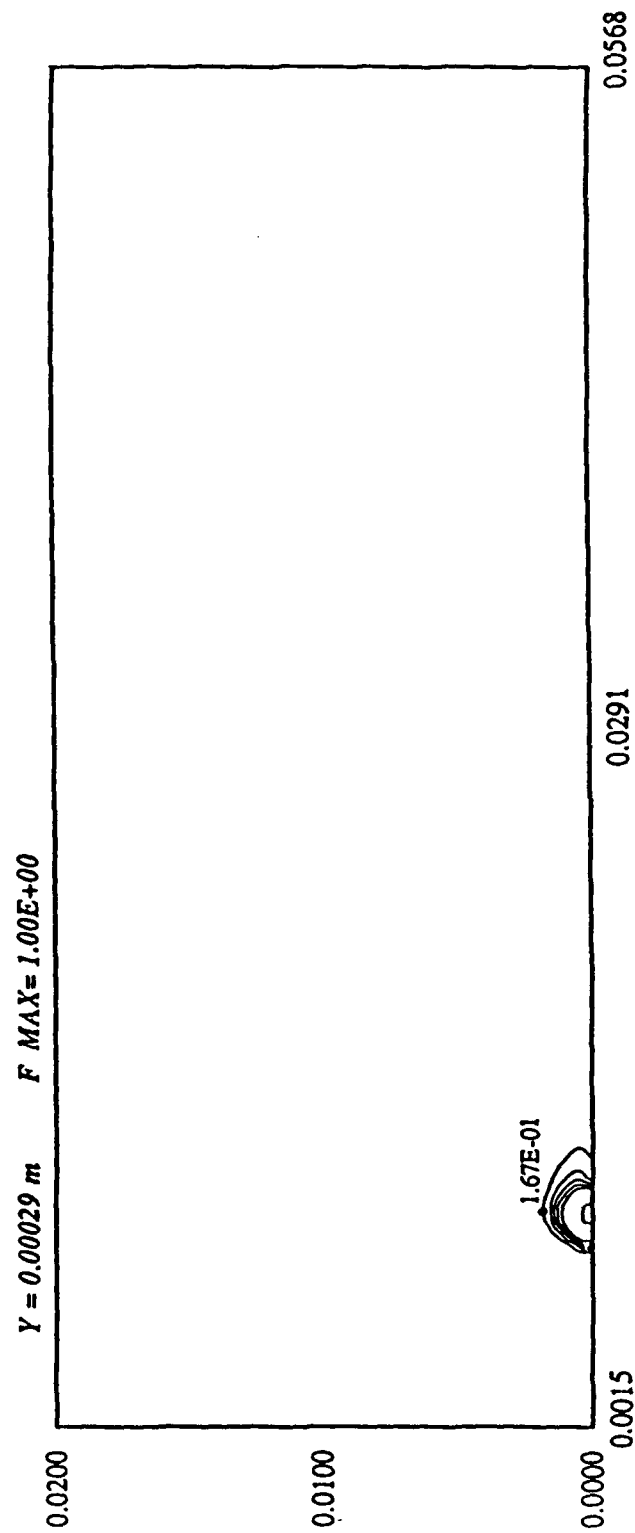


Figure C.12: Mass fraction contours of injectant ($z-x$) at $x=0.00029 \text{ m}$.

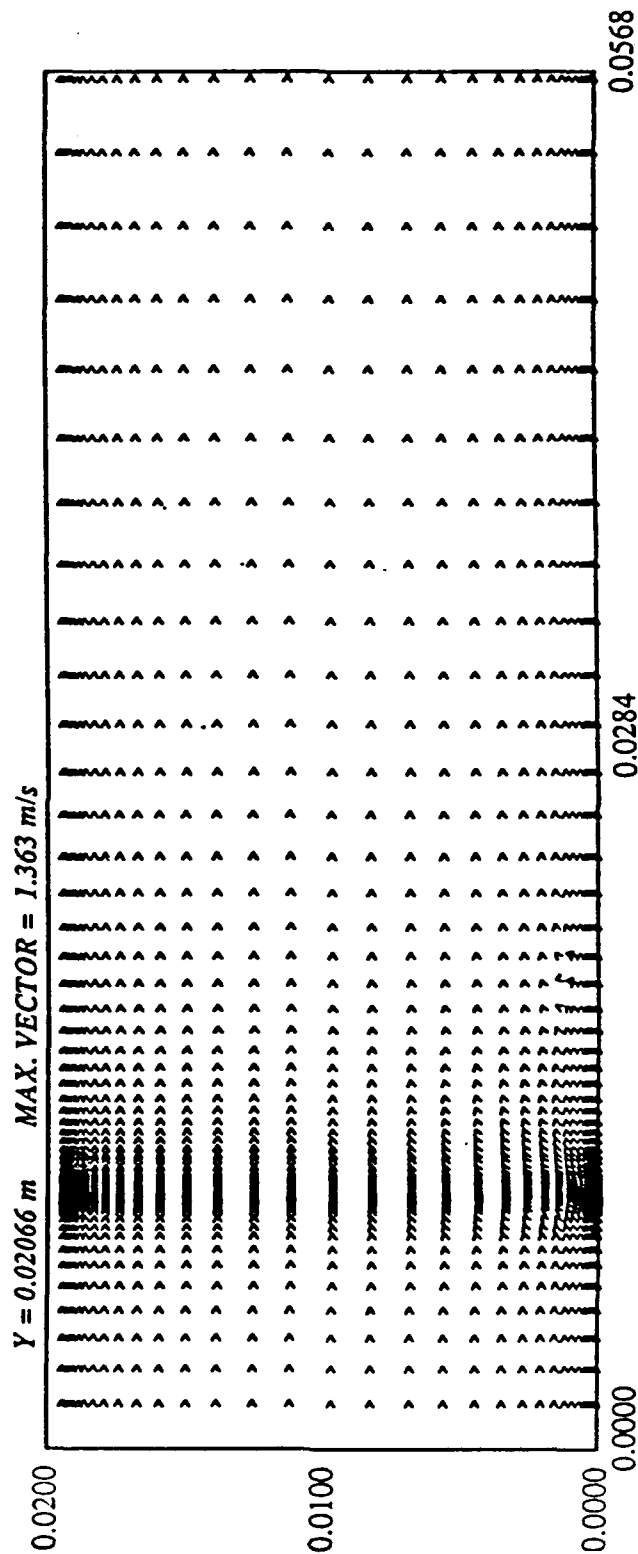


Figure C.13: Velocity vectors (z-x) at $y=0.02066$ m.

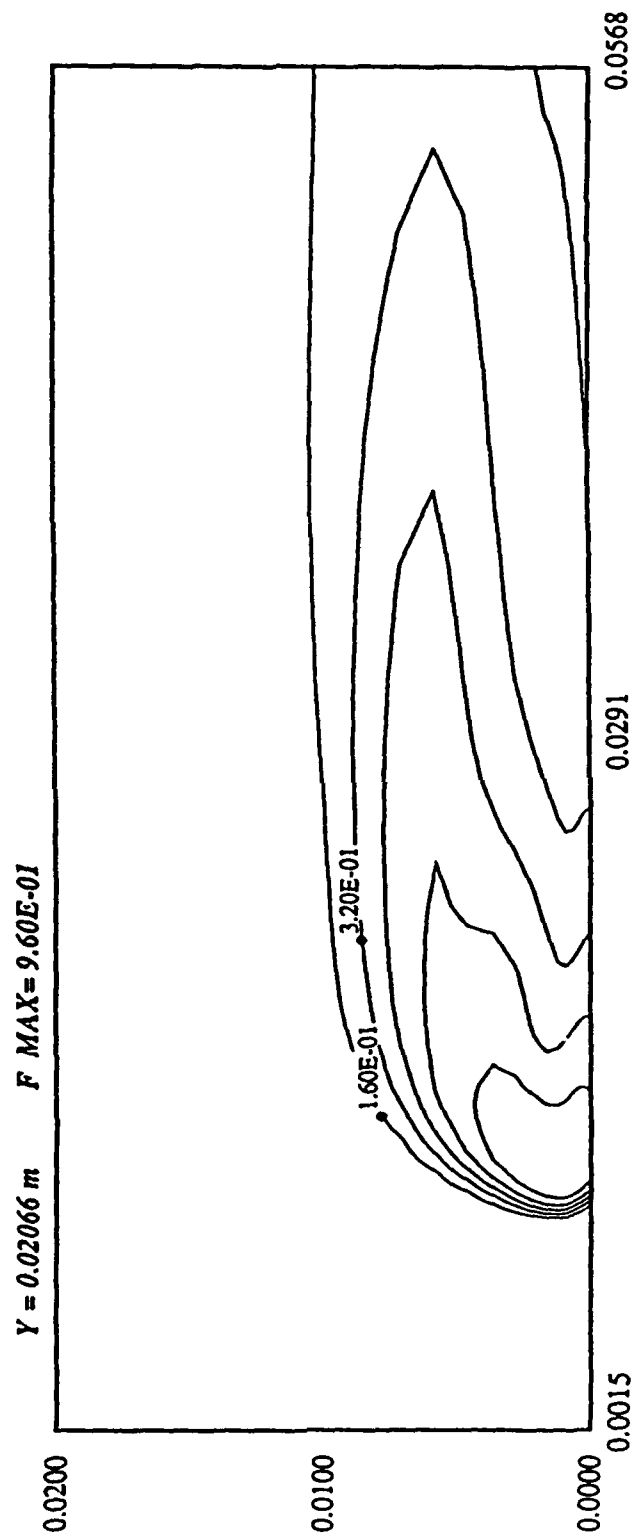


Figure C.14: Mass fraction contours of injectant ($z-x$) at $x=0.02066 \text{ m}$.

APPENDIX D

Phase III. Liquid Jet Injection

Figure D.1 shows a plot of volume fraction contours at $z=0.016$ m. The center of the injection orifice is located at $z=0.012$ m and the diameter of the injection orifice equals 0.004 m. Ideally, there should be only one contour line that separates the gas from the liquid. (In this case, the liquid is coming out of the page from the lower left-hand corner.) Due to numerical diffusion and the smearing resulting from the scheme (Equations (5)-(7)), unrealistic contours, like those corresponding to 0.3, 0.5 and 0.7, exist. Figure D.2 is the corresponding velocity vector plot at the same z location. A clockwise vortex is present, but the center of this vortex doesn't overlap with the one in the volume fraction plot, again showing the effect of numerical smearing.

Figure D.3 shows a volume fraction plot in a y - z cross-section at $x=0.0012$ m. The smearing is apparently more serious in the streamwise direction, according to this plot. At the end of the channel, the smearing completely shadows the supposedly-present liquid jet; i.e., one cannot tell whether the jet is a liquid one or a gaseous one at the end except the two 0.1 contours run in a rather parallel manner, uncharacteristic of gaseous jets. Figure D.4 is the corresponding velocity vector plot at the same x location. The original jet velocity structure is able to preserve itself in a few vertical grids. In view of the volume fraction plot, the liquid jet should be able to penetrate a little bit further into the gas stream if it were not affected by the numerical smearing.

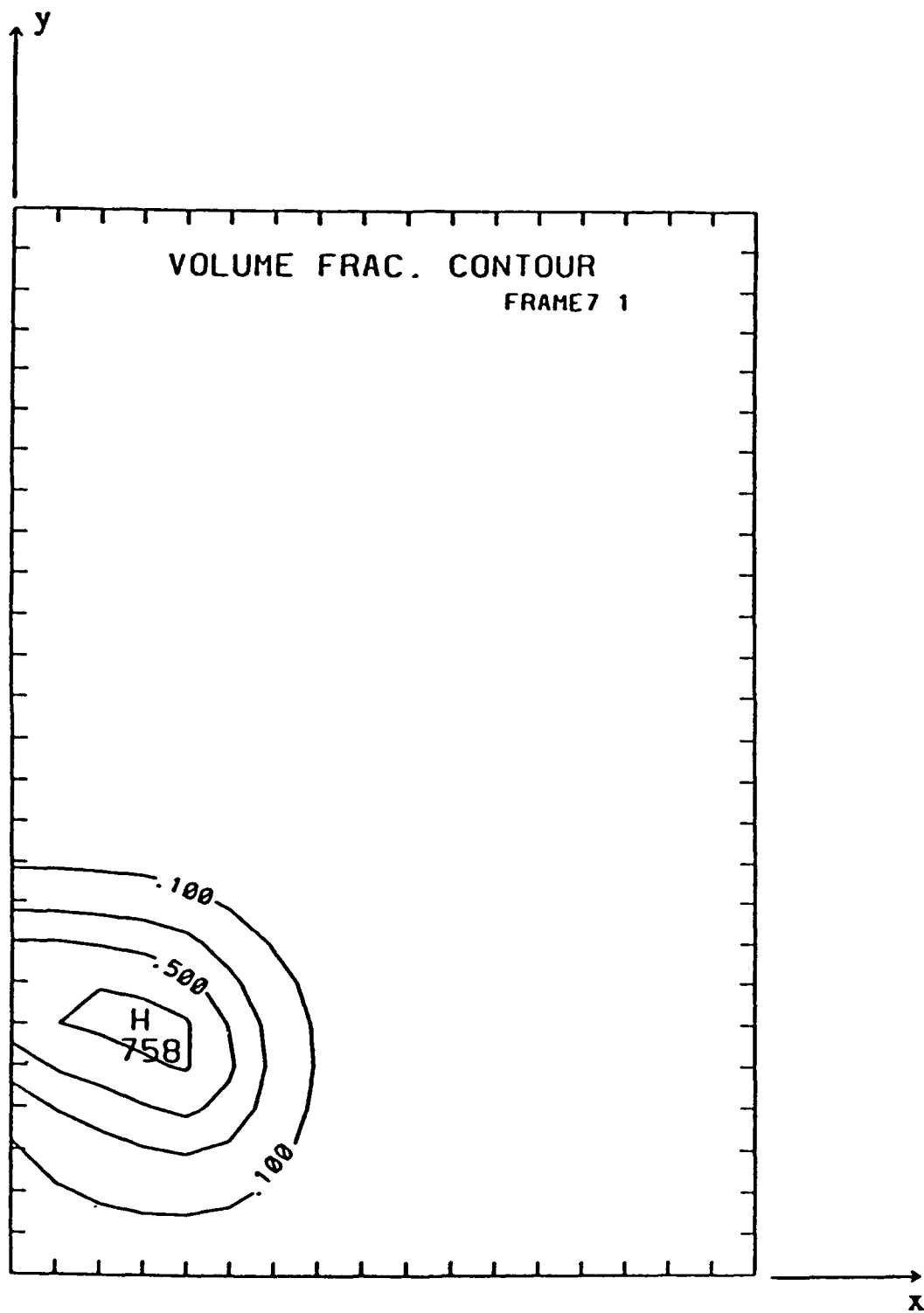


Figure D.1: Volume fraction contours at $z=0.016$ m.

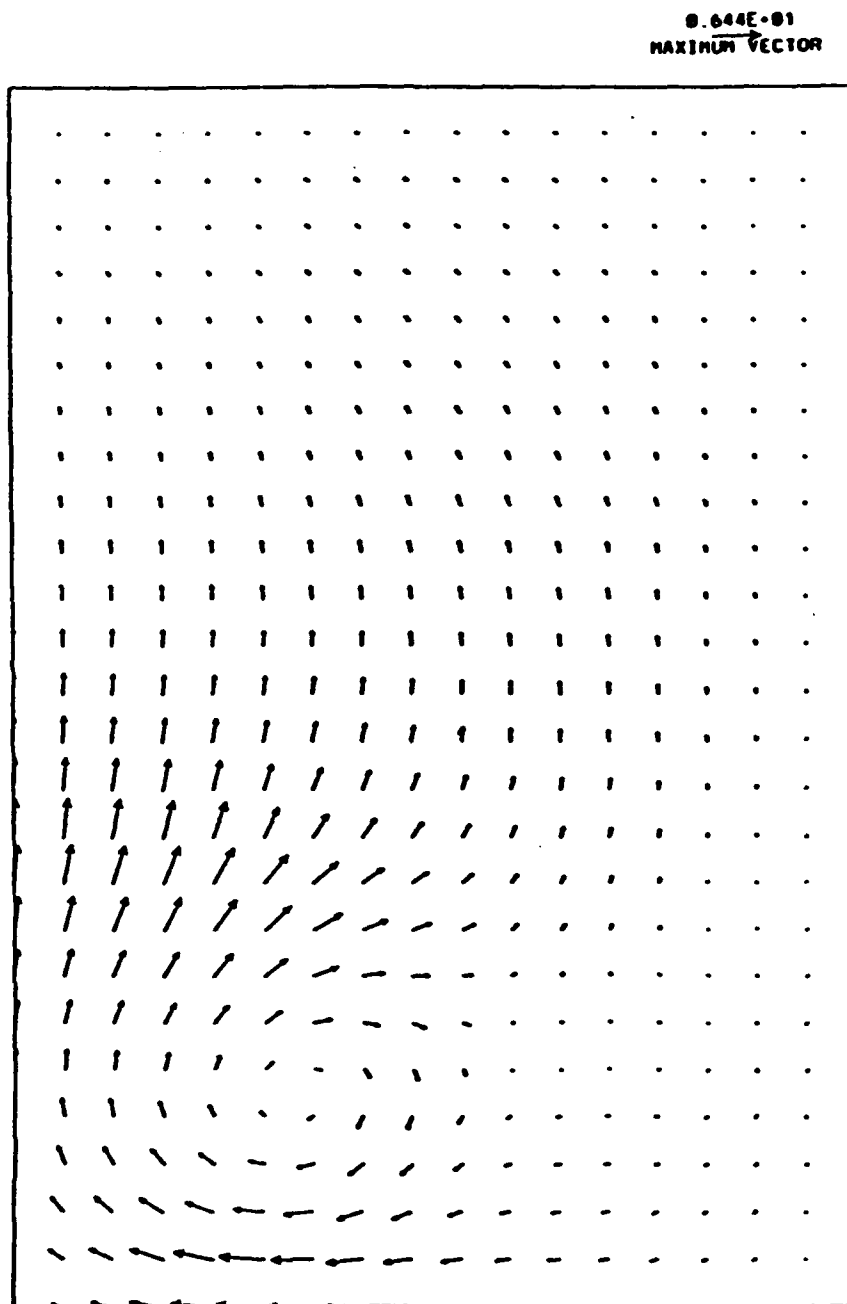


Figure D.2: Velocity Vector Plot at $z=0.016$ m.

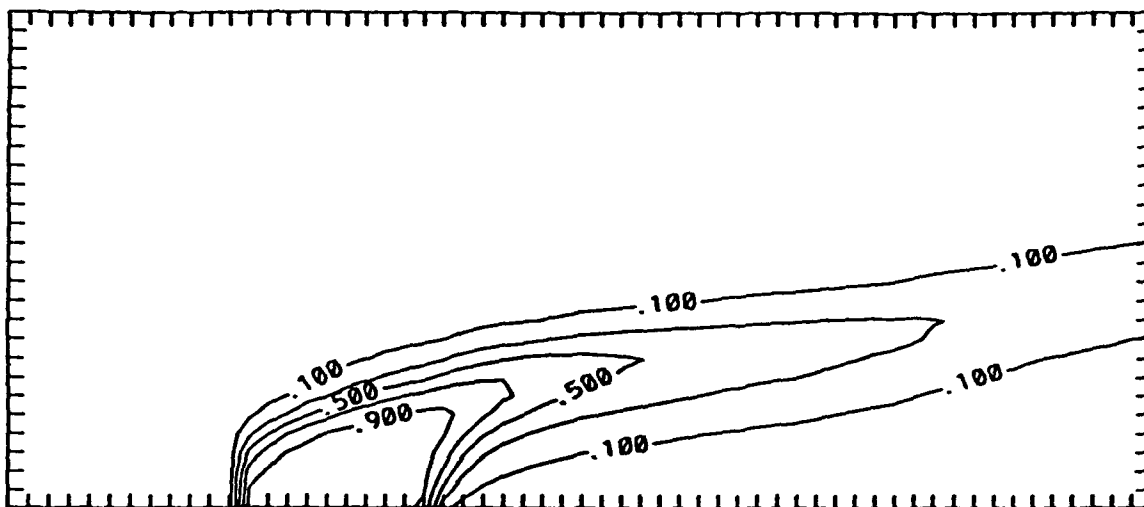


Figure D.3: Volume fraction contours at $x=0.0012$ m.

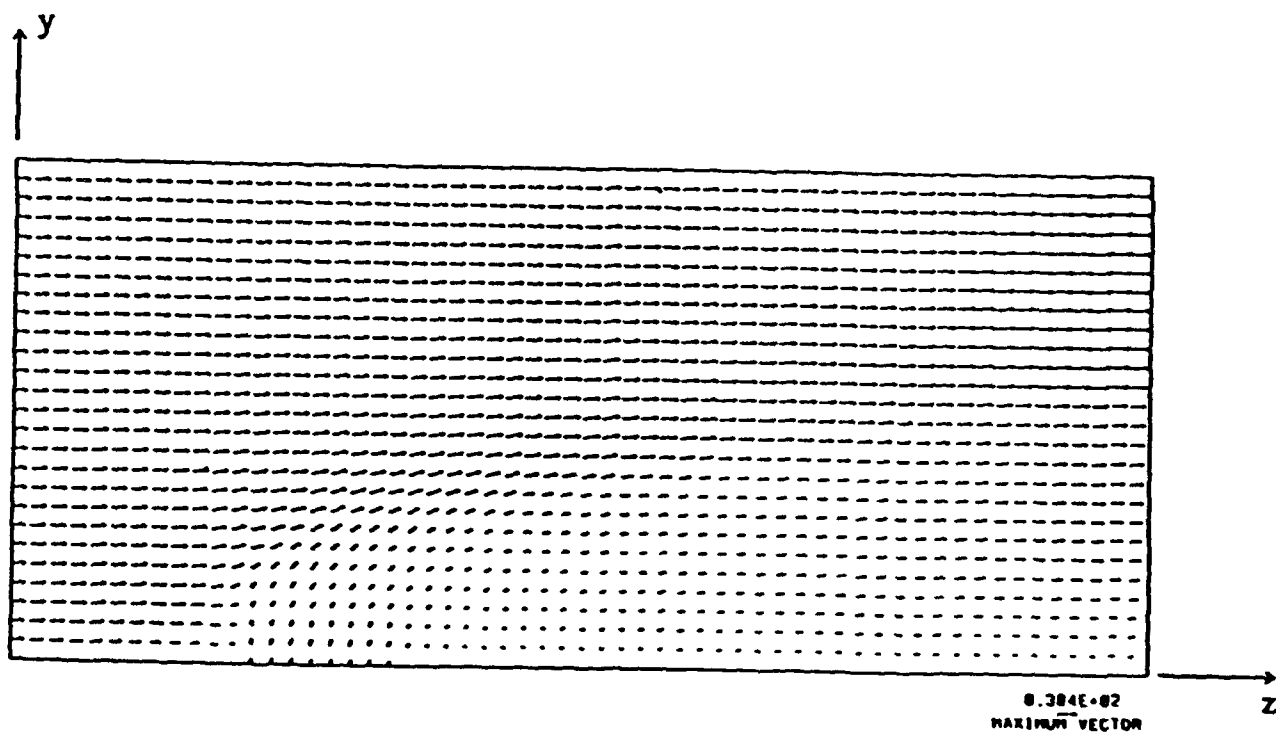


Figure D.4: Velocity vector plot at $x=0.0012$ m.